The Institute of Photonic Sciences

Hybrid diffuse optical neuromonitoring of cerebral haemodynamics: from the smallest premature born infants to adults

Martina Giovannella

Ph.D. dissertation

Advisor: Prof. Dr. Turgut Durduran
Co-advisor: Dr. Udo M. Weigel

Castelldefels (Barcelona), February 2019

Solo dopo aver conosciuto la superficie delle cose, - conclude -
ci si può spingere a cercare quel che c'è sotto.
Ma la superficie delle cose è inesauribile.
Italo Calvino, Palomar, 1983

Io penso che un uomo senza utopia, senza sogno, senza ideali,
vale a dire senza passioni e senza slanci
sarebbe un mostruoso animale fatto
semplicemente di istinto e di raziocinio,
una specie di cinghiale laureato in matematica pura
Fabrizio De André, intervista a Vicenzo Mollica

So... come up to the lab, and see what's on the slab
I see you shiver with antici... pation
Dr. Frank N. Furter, The Rocky Horror Picture Show, 1975.

Abstract

Hybrid diffuse optical devices allows for the non-invasive and continuous monitoring of the cerebral haemodynamics and metabolism. Such devices can be portable and are relatively inexpensive, therefore available at the bed- or cot-side. These advantages make the technology appealing and useful for a variety of applications. For my Ph.D. thesis, I have worked on the development of new devices that integrate diffuse correlation (DCS) and time resolved near-infrared spectroscopy (TRS) and on broadening their field of applications.

Preterm newborn infants are one of the target populations for such a neuromonitor. Premature newborns are at a risk of impaired neurodevelopment due to brain lesions that can be developed during first hours and days of life. In spite of the fact that these lesions are often due to episodes of abnormalities of the cerebral haemodynamics, related to oxygen supply to the brain and its consumption, these parameters are not currently monitored due to the lack of an appropriate technology. In order to meet this need, the BabyLux project aimed at developing a hybrid diffuse optical device that could be used to assess the cerebral well-being of the premature newborn infants.

In the framework of this project, I have developed and built the BabyLux device. Specifically, I have integrated DCS, to measure microvascular blood flow, and TRS, to measure microvascular blood oxygenation, into a user-friendly device, a prototype for a future medical grade device. In this thesis I report results of tests in laboratory settings in order to assess the de-

vice performance in best-case scenario. Furthermore, I explore the device's limits in precision and accuracy, through simulated DCS and TRS data with realistic noise added, and I describe the influence of a variety of experimental and analysis parameters. In addition, I demonstrate a high correlation between cerebral blood flow (CBF) measurement performed by the BabyLux device and by the gold standard positron emission tomography with ^{15}O-labeled water on a neonatal piglet model. This proves the robustness of the BabyLux solution for blood flow measurement and provides a calibration formula to convert the DCS-measured blood flow index into traditional flow units.

Finally, the device was tested in clinical settings, on healthy term newborns. It allowed for following cerebral haemodynamics and metabolism during the transition after birth. Reproducibility over probe replacement appeared improved with respect to commercial oximeters for tissue blood oxygen saturation and comparable to other technologies for the blood flow.

For an additional study on adult healthy volunteers, I have constructed a hybrid device integrating a commercial DCS and a prototype for a TRS device. This could serve as a neuro-monitor for following the cerebral response to transcranial direct current stimulation. This is a non-invasive form of stimulating the brain that has proven to be effective for cognitive augmentation and for treating pathological conditions.

In conclusion, the work presented in this thesis paves the way to a new generation of neonatal neuro-monitors that can be developed for extensive, multi-center clinical testing and ultimately allow a robust and accurate assessment of the cerebral well-being of the newborns. As far as the adult brain is concerned, I have introduced a new method for monitoring the cerebral response during transcranial direct current stimulation that can be exploited for protocol and dosage definition and, eventually, for the on-line monitoring of the cerebral response to the stimulation, tailoring the intervention to each subject's condition.

Resumen

Las tecnologías de óptica difusa permiten estimar de manera no invasiva y continua la hemodinámica y el metabolismo cerebral a través de instrumentos manejables, de coste relativamente bajo y disponibles al lado de la cama o la cuna del paciente. En mi tesis doctoral he desarrollado un instrumento que combina dos técnicas de óptica difusa: "diffuse correlation spectroscopy" (DCS) y "time resolved near-infrared spectroscopy" (TRS). Además, he contribuido a explorar nuevas aplicaciones para estas tecnologías.

Los prematuros recién nacidos son unas de las poblaciones objetivos para este tipo de aparato de monitorización cerebral. El desarrollo cerebral de los prematuros es más susceptible de lesiones cerebrales desarrolladas en las primeras horas o días de vida. Aunque estas lesiones cerebrovasculares son generalmente causadas por anomalías en la hemodinámica cerebral, es decir en el flujo sanguíneo hacia el cerebro o en el nivel de oxigenación del tejido cerebral, estos parámetros no son monitorizados de forma continua porque no existe una tecnología que permita hacerlo. El proyecto BabyLux, en el que participé activamente, tenía el objetivo de desarrollar un instrumento que utilizara óptica difusa para monitorizar el cerebro de los bebés prematuros.

Con el consorcio del proyecto BabyLux, he desarrollado y construido un aparato que combina DCS, para medir el flujo sanguíneo microvascular, y TRS, que mide la oxigenación del flujo microvascular, con el objetivo de que fuera preciso, exacto y sólido como para poder utilizarse en aplicaciones clínicas. En

esta tesis se exploran sus límites de precisión y exactitud, simulando datos DCS y TRS, y cómo estos se ven influenciados por varios parámetros experimentales y de análisis. Además, se demuestra una fuerte correlación en lechones entre el flujo sanguíneo medido por BabyLux y lo medido por tomografía por emisión de positrones (PET) con ^{15}O como radiofármaco, técnica de referencia para medir el flujo sanguíneo cerebral. Esto demuestra la fiabilidad de la medida de flujo de BabyLux y, además, permite calibrar el flujo sanguíneo medido por la DCS y convertirlo en la unidad tradicional de medida de flujo.

Finalmente, el dispositivo fue ensayado en hospitales. La hemodinámica cerebral fue monitorizada en los minutos posteriores al nacimiento de bebés sanos. La reproducibilidad de las medidas de BabyLux demostró una calidad superior respecto a los oxímetros cerebrales actuales y comparables a otras tecnologías para medir el flujo cerebral.

Estudios adicionales han investigado la hemodinámica cerebral de voluntarios adultos y sanos con otro aparato que he construido combinando una DCS comercial y un prototipo para una TRS. He demostrado que este aparato puede ser útil para investigar la respuesta cerebral a la estimulación eléctrica transcraneal, una forma de estimulación no invasiva que ha dado buenos resultados para tratar condiciones patológicas o para mejorar capacidades cognitivas.

En resumen, el trabajo presentado en esta tesis abre el camino hacia una nueva generación de instrumentos capaces de monitorizar el cerebro de los bebés prematuros, que puedan ser utilizados en ensayos clínicos en varios hospitales y de forma extensiva. Además, he introducido una nueva técnica para monitorizar la respuesta cerebral a la estimulación transcraneal que pueda ayudar a la hora de definir protocolos y dosis de la estimulación y que permite adaptar el protocolo a cada sujeto.

Acknowledgements

The time as a PhD student is surely very stressful, with a mixture of complicated tasks and the uncertainty about the path you are following and the decision you have to make. It would be impossible to arrive at the end without a team of individuals supporting you and your research work.

I must start by thanking Turgut Durduran, who gave me the possibility to start and continue this journey. I have always appreciated his efforts to make us develop the ability of critical thinking. I also thank Udo M. Weigel, my co-supervisor. I have learned how to put attention in every detail with him.

During my PhD years I spent several months in Copenhagen. This was a very enjoyable period of my life and I must thank Gorm Greisen and Bjørn Andresen for giving me the opportunity to pursue this. I have learned a lot working closely to you and I have good memories of the time spent in your hospital.

Most of the work presented in this thesis have been developed within a collaboration with the Physics department of Politecnico di Milano. Going through these pages I cannot actually imagine what this thesis would have been without having worked closely with them. In particular I thank Davide Contini, Alessandro Torricelli and Lorenzo Spinelli. You have thought me a lot, the time spent discussing with you or working with you in the lab has been valuable and precious. Each time I addressed you a question or a doubt by email, I knew I could expect a prompt answer from you. Thank you for your

supervision to my work.

I thank all the BabyLux consortium. I am so grateful I could take part in such a project. I believe that with our meetings, our technical discussions and our phone calls we have reached very good results. In particular I want to thank Monica Fumagalli and Agnese de Carli for the enthusiasm they put in their research work. That was extremely inspiring.

I want also to thank the NeuroElectrics and StarLab team, especially Giulio Ruffini and David Ibañez. The study run in collaboration with you was the first one I was responsible of and it will have a special place in my memories.

I want to thank all the persons who joined the Medical Optics group over those years. I believe we have always created a supportive and pleasing environment, in spite of the stress we all faced while running our own research. This is something very precious, that not every research group has.

A costo di sembrare campanilista, voglio ringraziare tutti gli italiani che a ICFO hanno animato i miei pranzi e le pause caffè. Grazie per formare questa bolla di sapone che ci fa poi guardare a come le cose vanno in Italia con stupore. Essere una migrante economica insieme a voi ha tutto un'altro sapore.

Unas palabras de agradecimiento van al súper equipo de VyC, por estos cinco años de amistad, especialmente a Blanca, por corregir el resumen de esta tesis y porque cada vez que hablo contigo aprendo una nueva palabra en castellano, y a Laura, porque fuiste el cruce y el principio de todo.

Gracias a Pam, de Can Kairos, sobre todo por estos últimos meses, porque es muy difícil pensar en la tesis cuando estás boca abajo o colgada de una sola mano.

Moltes gràcies a tot l'equip del Barcelona Shag team. Quan vaig apuntarme a aquell curs de rutines de Shag no sabia que hauria trobat una família. Gràcies per tots els assajos, els sopars i dinars post assajos, els viatges en cotxe, les emocions pre i post actuació, els nostres shag attacks i els mojitos settle up! Gràcies a la Bàrbara i l'Adrià, per invertir tant d'energia en fer-ho possible. Moltíssimes gràcies a la Bàrbara per dibuixar la portada d'aquesta

tesi i, a més, per dur l'esmorzar aquell dia!

Grazie a miei amici di sempre, di Orvieto. Grazie a Marta, perché l'inizio della nostra amicizia lo considero l'inizio della mia vita adulta. Grazie a Sara, perché ci capiamo al volo. Grazie a Damiano, perché per noi sarà sempre il nostro crucco originario. Grazie a Simone (e a lui gliene devo doppio), per la gioia con cui ci si ritrova sempre e perché ci insegna come inseguire le proprie passioni.

Grazie alla mia famiglia. Grazie a Franco per esserci sempre e per gli innumerevoli viaggi da e per l'aeroporto che mi hanno reso più vicina. Grazie a tutte le donne della mia famiglia, presenti e passate, che mi hanno insegnato così tanto, probabilmente senza rendersene conto. Grazie a mia mamma, per il viaggio incredibile che è stato crescere e vivere con lei, per l'esempio che è stato ed è per me e per essere il mio rifugio.

Grazie a Emanuele, per la squadra incredibile che formiamo insieme.

Contents

List of Figures

List of Tables

List of Abbreviations

ASL-MRI	arterial spin labeling magnetic resonance imaging
ACZ	Acetazolamide
BFI	blood flow index
CBF	cerebral blood flow
CBFV	cerebral blood flow velocity
CDE	correlation diffusion equation
CI	confidence interval
$CMRO_2$	cerebral metabolic rate of oxygen
$CMRO_2I$	cerebral metabolic rate of oxygen index
CV	coefficient of variation
CW	continuous wave
CW-NIRS	continuous wave near-infrared spectroscopy
DC-tCS	transcranial direct current stimulation
DCE-NIRS	dynamic contrast-enhanced near-infrared spectroscopy

DCS	diffuse correlation spectroscopy
DPF	differential path-length factor
DTOF	distribution of time of flight
EEG	electroencephalography
$EtCO_2$	end-tidal CO_2
EZBC	extrapolated zero boundary condition
FD-NIRS	frequency domain near-infrared spectroscopy
fNIRS	functional near-infrared spectroscopy
FTOE	factor of tissue oxygen extraction
FWHM	full width half maximum
gCBF	global cerebral blood flow
Hb	haemoglobin
HbO_2	oxy-haemoglobin
HHb	deoxy-haemoglobin
HRRT	high resolution research tomograph
IRF	instrument response function
LME	linear mixed effects
MAP-TR	maximum a posteriori for transmission
MRI	magnetic resonance imaging
NIR	near-infrared

NIRS	near-infrared spectroscopy
nrCBF	normalized regional cerebral blood flow
OD	optical density
$PaCO_2$	partial pressure of carbon dioxide
PaO_2	partial pressure of oxygen
PCBC	partial current boundary condition
PDE	photon diffusion equation
PET	positron emission tomography
pH	acidity/alkalinity scale for an aqueous solution
rBFI	relative blood flow index
rCBF	regional cerebral blood flow
SaO_2	arterial oxygen saturation
SD	standard deviation
SNR	signal to noise ratio
SPAD	single photon avalanche photodiode
SPECT	single photon emission computed tomography
SpO_2	peripheral arterial oxygen saturation
StO_2	tissue oxygen saturation
TCSPC	time-correlated single photon counting
tHb	total haemoglobin

TOE tissue oxygen extraction

TRS time-resolved near-infrared spectroscopy

UPS uninterruptible power source

VOI volume of interest

Part I

Introduction, theory, instrumentation and algorithms

Chapter 1

Introduction

Personalized medicine is an old concept currently gaining more and more popularity. Modern medicine is being nowadays pushed towards treatment and intervention designed and optimized for each individual. This is today a concrete possibility thanks to the development of technologies that allow the patient to receive early diagnosis, risk assessment and to tailor the treatment to each individual [218].

In order to put in practice such a clinical routine, diagnostics is fundamental. Information on the state and evolution of the patient must be acquired, within time-scales that will depend on the specific condition and application. This is believed to be particularly important for the clinical condition when the brain is to be protected [208]. Specifically, the brain must be always correctly perfused of oxygen in order to sustain its metabolic activity. The necessary amount of oxygen to the brain must be provided and the sufficient level of cerebral blood flow (CBF) maintained to meet the metabolic demand [198]. Pathological conditions arise from episodes of compromised cerebral haemodynamics, referred to supply or consumption of oxygen by the brain.

Neuro-monitoring aims at preventing harmful pathological events by early detection of abnormalities in brain haemodynamics [182]. An on-line feedback

to treatment can be provided by monitoring the cerebral well-being continuously and routinely. Guidelines should suggest how to maintain the CBF and oxygenation of blood to the correct reference clinical values. The main purpose of such a brain-oriented care should be prevention, to avoid irreversible damage to the brain. Since such episodes may be unexpected and the condition of the brain may change rapidly, such a neuro-monitor should run continuously and be available at the bed- or cot-side. In addition it should be non-invasive, to be applied to a variety of populations, and relatively inexpensive, to be extensively available, ideally for each patients [182].

Preterm born infants are one target population which may benefit from continuous neuro-monitoring. This condition is unfortunately not rare in our society. Statistics reports a impressively large amount of infants born preterm (24-32 weeks of gestational age). A report by World Health Organization estimates fifteen millions of premature births worldwide every year and this number is rising [146]. Prematurity is now the leading cause of death of children under five years of age worldwide [142] and survivors often develop neurodevelopmental impairments (cerebral palsy, mental retardation, and sensory impairments) and dysfunction in other cognitive areas, such as attention, visual processing, academic progress, and executive function [193]. The high number of preterm infants and high rate of bad outcome produce high medical care costs, for the intensive care in the period after birth and for the life-time assistance that survivors with disabling conditions need [146, 193].

The neurodevelopment of preterm newborns can be negatively affected by brain lesions developed especially during the first hours and days of life, when preterm newborns often need intensive care due to the immaturity of the respiratory and cardiovascular system. The etiology of cerebral lesions is complex but seems to be mainly related to hypoxia and poor cerebral perfusion leading to hypoxia-ischemia [25]. Immaturity of the cardiovascular adaptive system compromises the balance between oxygen demand and delivery [161]. The degree of maturity of cerebral autoregulation, which represents the abil-

ity of maintaining CBF stable even when changes in blood pressure occur by changing cerebrovascular resistance (*i.e.* diameters of the vessels), is not yet understood in preterm infants [76]. The slope and limits in the CBF versus arterial blood pressure curve seems to vary consistently among infants [25].

This picture suggests that intensive care should be brain oriented and should adapt to the actual degree of development of each infant. This is currently not achieved because it is not possible to monitor at the cot-side the perfusion and oxygenation of the newborn brain [138]. The currently available technologies are not eligible for such a neuro-monitor. Whole-head haemodynamic monitors such as positron emission tomography (PET) [87], single photon emission computed tomography (SPECT) [222] and magnetic resonance imaging (MRI) based techniques [28] are bulky, expensive, need patient transport and immobility. All these are fundamental drawbacks especially when those technologies should be employed routinely in infants. While ^{133}Xenon clearance, an historically important methodology for measuring blood flow, requires a radioactive tracer [166]. These days, doppler ultrasound is the only method to monitor the brain haemodynamic widely exploited in the neonatology clinics [49]. It provides invaluable insight on the eventual pathological cerebral events, but it is operator-dependent and it only provides a one-shot picture of the cerebral haemodynamics of the infant. Due to this technology deficiency and scarcity of clinical studies, no reference clinical values have been defined for CBF and blood oxygenation in the brain [138]. Consequently, it is absolutely not clear how a care intended to maintain the cerebral haemodynamics parameter to a normal range would influence the rate of impaired neurodevelopment and disabling conditions [25].

Monitoring the supply and consumption of oxygen by the brain can be useful also for the adult population in a variety of conditions, involving the necessity of intensive care [208]. In this thesis, I, instead, focus on monitoring the evoked cerebral response to a stimulus. Specifically, monitoring cerebral haemodynamics can be used to measure cerebral activity thanks to the prin-

ciple of neurovascular coupling. When a brain region is activated and the rate of oxygen consumption ($CMRO_2$) in that region rises, the local cerebral blood flow is increased to supply the metabolic demand [199]. The processes involved in CBF recruitment are various, complex and not fully understood [185, 199] but haemodynamic monitors are now heavily employed in functional studies. Measuring cerebral evoked response is interesting for basic neuroscience knowledge but it has also application in several pathological condition. For example interest is growing on transcranial direct current stimulation (DC-tCS), a non-invasive form of brain stimulation that applies weak direct electrical currents from electrodes placed on the scalp [160, 179, 191]. It can have application both in healthy subjects, for improvement of cognitive function, and for several pathologic conditions [27]. Measuring cerebral response to the stimulation has a two-fold interest. At this stage it is still not clear how the stimulation works and what are the best protocols and dosages of application. Furthermore, it has been raised that the efficacy of the stimulation can be optimized by a personalized protocol, for which it would be important to have an on-line read-out of the effects of the stimulation, by measuring concurrently the cerebral response [17].

I have here reported different conditions that solicit an enabling technology that could provide continuous, non-invasive information of cerebral haemodynamics at bed- or cot-side. In the following section I will explain how photons of a selected range of the near-infrared can constitute "enabling" tools for this purpose. This thesis is indeed focused on development and application of diffuse optical technologies for monitoring brain haemodynamics, for clinical purposes as well as for neuroscience.

1.1 Diffuse optics for haemodynamic monitoring

Biological tissue are relatively transparent to photons in a range of the near-infrared (NIR) (between 650 and 950 nm) thanks to the low absorption of water

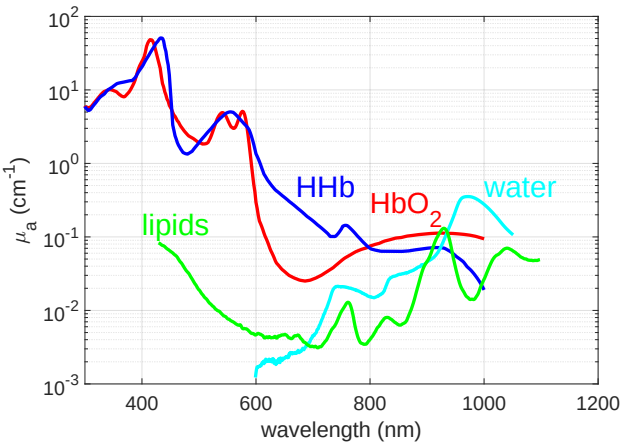

Figure 1.1: Absorption coefficients in the NIR range of the main chromophores (oxy- (HbO_2) and deoxy-haemoglobin (HHb), water and lipids) at their typical concentration values in tissue.

and blood [41]. This range is referred to as "physiological window" (figure 1.1).

In this wavelength range, biological tissues are diffusive media, photon propagation is mainly ruled by scattering and several scattering events occur before photons are absorbed. Therefore photons propagate in a random-walk and their propagation is described by a diffusion equation. In near infrared spectroscopy (NIRS) absorption properties (figure 1.1) are characterized at multiple wavelengths in order to retrieve information about oxy- (HbO_2) and deoxy-haemoglobin (HHb) concentration (c_{HbO_2} and c_{HHb}) [110].

The photon penetration depth depends on the experimental setup and on the illumination but it is usually 1-1.5 cm. However, depth sensitivity can be improved using short time pulses as the source and specific data analysis methods [147]. It is therefore possible to use NIR light to probe relatively deep tissue and, for example, reach the cerebral tissue by illuminating from the surface of the head. Information retrieved with diffuse optics refer to the

microvasculature of the tissue, because photons traveling in the arterial and venous compartment are completely absorbed.

Different diffuse optical technologies are available, depending on the source type [52]. Difficulties arise because, in order to obtain HHb and HbO_2 concentration and consequently the tissue oxygen saturation (StO_2=c_{HbO2}/c_{tHb}), it is necessary to decouple the effect of scattering and the effect of absorption. This requires to take advantage of more complex source of illumination.

In case a constant intensity light source is employed, only the light attenuation after propagation in the tissue is detected. This is referred to as continuous wave NIRS (CW-NIRS) and relates changes in attenuation to changes in HHb and HbO_2 concentration [41]. A single measurement does, therefore, not allow an absolute estimation of the chromophore concentrations but only of changes. Currently, various medical CW-NIRS devices are available, with the name of oximeters [195]. Most of them infer the StO_2 estimation from multi-distance measurements.

More complex technologies that collect more information on the light propagated into the tissue are necessary to solve both scattering and absorption properties, hence to measure oxy- (HbO_2) and deoxy-haemoglobin (HHb) in their absolute concentrations. In frequency domain NIRS (FD-NIRS), intensity modulated light is injected into the tissue and the amplitude and phase of the emerging light measured. From multi-distance measurements it is possible to retrieve absorption and scattering properties of the tissue [177, 224]. On the other hand, in time resolved NIRS (TRS) [170], the light source is a short pulsed laser whose shape after propagation into the tissue is studied. Differently from multi-distance FD-NIRS, from a single measurement it is possible to obtain absorption and scattering properties of the tissue at the wavelength used [35]. Moreover, the information in depth is naturally encoded in time in a TRS pulse, since the photons arriving early have, on average, traveled more shallow regions than photons arrived at later times. These are the advantages of TRS compared to FD-NIRS. Traditionally, FD-NIRS uses simpler

and cheaper components, but research on TRS is pushing towards miniaturization of components and improvement of cost-effectiveness [184]. Currently, a FD-NIRS device is commercialized by ISS, USA (Imagent or MetaOx) not as a medical but as a research device [29, 210]. While a TRS device is commercialized by Hamamatsu Photonics K.K., Japan (tNIRS-1) approved as medical device only in Japan [69].

Dynamic properties of the tissue can also be studied with diffuse optics. Moving scatterers, *i.e.* red blood cells, are present in the tissue and their movement influence the coherence property of the emerging light. Diffuse correlation spectroscopy (DCS) studies the electric field autocorrelation function to retrieve information of the blood flow in the microvasculature of the tissue. DCS has been commercialized by HemoPhotonics S.L., Spain (HemoFloMo) and ISS, USA (MetaOx, integrated with a FD-NIRS device).

In the previous section I have highlighted how the current technologies for measuring brain haemodynamics are not useful for monitoring the preterm newborn brain, since they are either invasive or minimally invasive, not portable and do not provide continuous measurements. Diffuse optical technologies can overcome all these problems and the neonatology community has shown interest since the early time of this technology [79]. The majority of commercial cerebral oximeters (CW-NIRS devices) have indeed a version specific for neonatal and pediatric use and they can be found in selected neonatology units. In addition, different randomized clinical trials have demonstrated that adding cerebral oximetry to the standard clinical care can reduce the burden of cerebral hypoxia in preterm infants [96, 173]. In spite of this, currently available monitors do not appear to be robust and accurate enough for accurately and precisely monitor the oxygenation of the infant brain and neonatologist claim that a further techology development is needed [78]. In addition these monitors do not provide information on oxygen supply but only on the oxygenation, not enough for characterizing some pathological conditions [21, 25].

1.2 Objectives

The present work of thesis is focused on the development of the integration of two diffuse optical technologies, diffuse correlation spectroscopy (DCS) and time-resolved near-infrared spectroscopy (TRS), for concurrent continuous monitoring of cerebral blood flow and oxygen consumption. This technological development is focused towards hybrid device application in neuroscience and in clinical monitoring of the premature newborn cerebral well-being.

In this section I will list the objectives set to reach the main goals of this thesis.

Instrumentation

BabyLux device

- To develop a hybrid DCS and TRS device that could be used as a neuromonitor for term and premature newborns at the cot-side, being robust and accurate
- To explore its limits of precision and accuracy through simulated data with realistic noise
- To test the device in laboratory settings

Hybridization of a commercial DCS device and prototype for a TRS device

- To develop the communication between the two devices in order to acquire simultaneously with the two and minimize the cross-talk
- To test the hybrid device in laboratory settings

Validation study of BabyLux device for CBF measurement

- To validate cerebral blood flow measurement by DCS with ^{15}O-labeled water positron emission tomography (PET) on a piglet model

Clinical studies to validate the BabyLux device in real-life settings

- To follow the cerebral haemodynamics during transition after birth in healthy term newborns born by an elective cesarean section
- To assess the variability over replacement of the BabyLux probe in healthy term newborns

Functional study

- To measure cerebral haemodynamics during and after transcranial direct current stimulation of the frontal cortex
- To monitor concurrently cerebral haemodynamics and electroencephalography (EEG) during and after transcranial direct current stimulation

1.3 Outline

This thesis is divided in three parts. The first part is dedicated to the theoretical and technical background. Chapter 2 explains the theory of photon diffusion in biological tissue and how to derive a solution of the photon diffusion equation. It also describes the theory for diffuse correlation spectroscopy. Chapter 3 explains the basis for DCS and TRS instrumentation, how to simulate realistic data and how to perform DCS and TRS data analysis. The second part of this thesis reports the work done in correlation with the BabyLux project and with the BabyLux device. Chapter 4 describes the BabyLux device and tests performed in laboratory settings, while chapter 5 explore the

limits in accuracy and precision of the device through simulated data. Chapter 6 reports the validation of CBF measurement by DCS towards ^{15}O-labeled PET on a piglet model, employing the BabyLux device. Chapter 7 shows results from the clinical studies run with the BabyLux device in two different clinical centers. Specifically, cerebral haemodynamics has been monitored during transition after birth in healthy term newborns. Another study aimed at assessing the variability over replacement of the haemodynamic parameters on the same population in the first day of life. The third and final part reports the work done combining a commercial DCS device and a prototype of a TRS device. In chapter 8 the development of the two device integration is explained and results of test in laboratory settings shown. In chapter 9 results from a study on healthy adult subjects is reported. Cerebral haemodynamics was measured with the hybrid device, concurrently with EEG, during transcanial direct current stimulation of the frontal cortex.

1.4 Disclosure

I disclose the following. Dr. Udo M. Weigel, co-supervisor of this thesis, is the CEO, has equity ownership in HemoPhotonics S.L. and is an employee in the company. HemoPhotonics S.L. was part of the consortium of the project "An optical neuro-monitor of cerebral oxygen metabolism and blood flow for neonatology (BabyLux)", funded by the European Commission Competitiveness for Innovation Program (grant agreement no. 620996). The work related to this project that I present in this thesis has been developed under Dr. Weigel's supervision. His role in the project has been defined by the project objectives, tasks and work-packages and was reviewed by the European Commission. Any conflicts of interest that may arise due to my involvement in this work was monitored by my institute (ICFO) and its Knowledge and Technology Transfer (KTT) unit. None were identified.

Chapter 2

Interactions of light with biological tissues

In this chapter I will describe the main physical processes that rule the propagation of photons in turbid media within the realm of this thesis work, *i.e.* absorption and scattering [148, 156, 221]. I will introduce the photon diffusion equation and specify under which assumptions it can be used for photon propagation in biological tissues. Afterwards, the photon diffusion equation will be solved for the semi-infinite homogeneous medium and considering a short laser light pulse as source type, this will be of interest for the experiments contained in this thesis [148, 170, 211].

The last part of the chapter is focused on how dynamic properties can be probed with diffuse optics by considering that part of the scatterers contained in the tissue, the red blood cells, are moving. The diffusion equation for the electric field autocorrelation function will be presented [19,20]. As before, it will be solved for semi-infinite homogeneous medium but considering a steady-state source [23, 52, 53]. This is the theoretical background for understanding time resolved near infrared spectroscopy (TRS) and diffuse correlation spectroscopy (DCS) that are the main technologies used in this thesis.

2.1 Introduction

Two main processes interest the propagation of light in biological tissue, absorption and scattering. A molecule can absorb a photon and raise an electron in an excited state. Consequently, the relaxation can happen with release of heat, in a non-radiative process, or in a radiative process, emitting another photon at a different wavelength. The former type of absorption event is what interests the work presented in this thesis [148].

On the other hand, scattering refers to the elastic interaction of photon with structural heterogeneities present into the tissue at the wavelength scale with a different index of refraction than the propagation medium [156]. Scattering events are associated to a change in direction of propagation.

The absorption coefficient describes the absorption property of the medium and is defined as the probability of photon absorption in the medium per unit infinitesimal path length [221]. Considering a medium with pure absorption, attenuation of light with intensity I traveling in the z direction in the interval $(z + dz)$ will be proportional to the absorption coefficient μ_a and dz

$$\frac{dI}{I} = -\mu_a dz \tag{2.1}$$

By integrating the above equation Beer's law is obtained for the transmittance $T(z)$

$$T(z) \equiv \frac{I(z)}{I_0} = e^{-\mu_a z} \tag{2.2}$$

Where $I_0 \equiv I(z = 0)$ is the incident light intensity. Typical biological tissue value of μ_a is 0.1 cm^{-1} in the range 650-950 nm.

Analogously, scattering coefficient μ_s is defined as the probability of photon scattering in a medium per unit infinitesimal path length [221]. In a purely scattering medium we can express the probability of no scattering events after

traveling a distance z as

$$\frac{I(z)}{I_0} = e^{-\mu_s z} \tag{2.3}$$

which is also referred to as ballistic transmittance. Typical value for μ_s at the wavelength typically used is 100 cm^{-1}. In biological tissues, where photons are both absorbed and scattered, we can define an extinction coefficient as $\mu_t = \mu_a + \mu_s$ [156].

Biological tissues contain many scatterers randomly distributed in space, therefore photons undergo multiple scattering events in their propagation. Since the average distance between scatterers is large compared to the scatterer size and the wavelength used in diffuse optics, we can consider each of the scattering event as independent [148]. Therefore, the optical properties of the media are related to the optical properties of the single scattering particle, described exactly by the Mie theory for spherical particles, or by the Rayleigh theory if the spherical particles are far smaller than the wavelength [148].

The statistical meaning of the absorption and scattering coefficient explained above gives a set of useful typical length-scales that describes the propagation of photon into the tissue. The reciprocal of the absorption coefficient is the absorption length l_a, which is the mean length traveled by a photon before being absorbed, while the reciprocal of the scattering coefficient, l_s the scattering length, is the mean length traveled by a photon before being scattered. l_s is also referred to as mean free path. Referring to the typical values explained above for μ_a and μ_s, l_a is typically 10 cm while l_s is 0.01 cm.

In a medium where propagation of light is described by multiple scattering events, photons accumulate change of direction in each of them up to a loss of memory of the initial one. This defines another distance, the transport mean free path l_{tr}, which is the average distance traveled by photons before their direction is completely randomized [164]. Its reciprocal is the reduced scattering coefficient $\mu_s' = (1 - g)\mu_s$, where g is the anisotropy factor and represents the degree of forward scattering. In particular $g = 0$ defines the

isotropic scattering, direction of propagation is randomized at each scattering event, since $l_s = l_{tr}$. While $g = 1$ means that all the light is scattered in the forward direction, the memory of the initial propagation direction is never lost in this limit. Typical g values for biological tissue are approximately 0.9, quite close to unity. Therefore l_{tr} is typically 0.1 cm and its reciprocal μ'_s is 10 cm^{-1}.

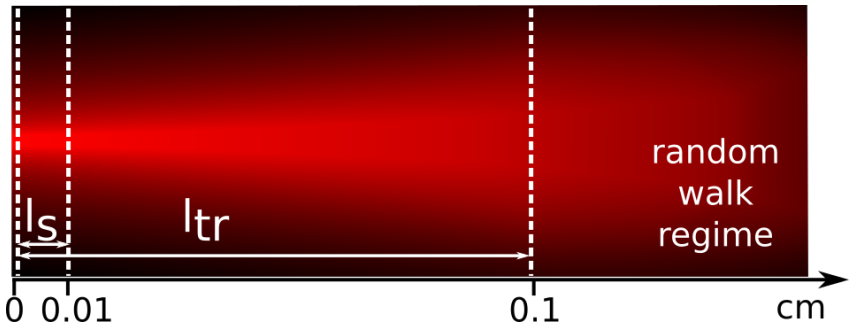

Figure 2.1: Schematic of fundamental length-scales of photon scattering into a typical biological tissue. This refers to typical values for biological tissue of μ_a=0.1 cm^{-1}, μ'_s=10 cm^{-1} and μ_s=100 cm^{-1}. After photon injection into the tissue, the photon propagation regime is ballistic within a length of $l_s = 1/\mu_s$. The direction of propagation will be completely randomized by several scattering events within a distance of l_{tr}=$1/\mu'_s$. At this point photon propagation into the tissue can be described as random walk. The third important length-scale for photon propagation into the tissue is l_a=$1/\mu_a$. This is not reported, being typically 100 times greater than l_{tr} and 1000 times larger than l_s, *i.e.* 10 cm in this example. All these values will depend on the specific tissue and on the wavelength used. Figure inspired by Ref. [164].

The length-scales that describe the scattering properties of biological tissue at the wavelength used in diffuse optics (650 nm-950 nm) are schematically depicted in figure 2.1. Even if the scattering events are mainly in the forward direction, the direction of propagation is ultimately lost, due to the accumulation of several scattering events. This happens within a length of approximately

0.1 cm and from this point photon propagation can be described as random walk regime. Figure 2.1 omits the third important length-scale, *i.e.* the absorption length l_a. This is about 10 cm, therefore 100 times larger than l_{tr} and than the drawing reported.

2.2 Photon diffusion equation

In the section above the main processes that rule the photon propagation in biological tissue are explained. An insight of the typical length-scale of this propagation, when using photon in the range 650 nm-950 nm has been given, highlighting that a random walk regime is reached after about 0.1 cm of propagation. Since the typical length-scale for direction randomization ($\sim$0.1 cm) is much greater than the absorption length ($\sim$10 cm), biological tissues are diffusive media and photon propagation can be described as a diffusion process.

Two assumptions are necessary for using this formalism: 1) the radiance (*i.e.* light power per unit area traveling in a certain direction) must be isotropic and 2) the photon flux (*i.e.* a vector sum of the radiance emerging from the infinitesimal volume) must vary slowly respect to the time scale $1/(v\mu_s')$ [148]. Both the requirements need the absorption to be small compared to the scattering ($\mu_s' \gg \mu_a$). In this way the propagation of photons is mainly affected by the scattering and photons undergo long path-lengths and their direction is randomized. In particular the mentioned time scale $1/(v\mu_s')$ equals 0.004 ns in a typical biological tissue (μ_s'=10 cm^{-1}, index of refraction n=1.4). This corresponds to a distance of 0.12 cm, far smaller than the absorption length (typically 100 cm). Therefore photon flux is not expected to vary in such a time scale.

We can thus write a diffusion equation for photon fluence rate $\Phi(\mathbf{r}, t)$(Wcm^{-2}), the total power per area going out from the infinitesimal value at position $\mathbf{r}$

and time t [221]:

$$\nabla(D(\mathbf{r})\nabla\Phi(\mathbf{r},t)) - v\mu_a(\mathbf{r})\Phi(\mathbf{r},t) + vS(\mathbf{r},t) = \frac{\partial\Phi(\mathbf{r},t)}{\partial t} \tag{2.4}$$

here $D(\mathbf{r}) = \frac{v}{3(\mu_s'(\mathbf{r})+\mu_a(\mathbf{r}))}$ is the photon diffusion coefficient and v the velocity of light in the medium. The photon diffusion equation (PDE), equation 2.4, relates the time derivative of the photon fluence rate to the gradient of the flux $\mathbf{J}(\mathbf{r},t) = D(\mathbf{r})\nabla\Phi(\mathbf{r},t)$, the loss due to absorption and the gain due to the source $S(\mathbf{r},t)$. In homogeneous medium, where the diffusion coefficient is space invariant, the PDE becomes

$$D\nabla^2\Phi(\mathbf{r},t) - v\mu_a\Phi(\mathbf{r},t) + vS(\mathbf{r},t) = \frac{\partial\Phi(\mathbf{r},t)}{\partial t} \tag{2.5}$$

where $D = \frac{v}{3(\mu_s'+\mu_a)}$. The photon diffusion coefficient is usually expressed as absorption independent $D \approx \frac{v}{3\mu_s'}$ using the assumption of $\mu_s' \gg \mu_a$ and making the diffusion coefficient proportional to the transport mean free path l_{tr} [54,148]. In this way the effect of absorption in the PDE is purely expressed in the loss term $(-v\mu_a\Phi(\mathbf{r},t))$.

2.3 Solution of the photon diffusion equation in time domain for a semi-infinite homogeneous medium

In order to solve the PDE, the geometry of the source and the diffusive medium must be defined. I will start considering a pulsed point source of unitary strength at the origin of space and time, *i.e.* $S(\mathbf{r},t) = \delta(\mathbf{r})\delta(t)$. Therefore the solution found will be the Green's function of the PDE. The most simple geometry that can be imagined is a homogeneous infinite medium. In this case the solution of the PDE for the fluence rate is [170]:

$$\Phi(\mathbf{r},t) = \frac{v}{(4\pi Dt)^{3/2}} e^{-\frac{r^2}{4Dt} - \mu_a v t} \tag{2.6}$$

The homogeneous infinite medium is a geometry easy to solve but, unfortunately, not usually applicable in real experiments, while the semi-infinite homogeneous medium is a more realistic geometry. Here an infinite boundary divides a diffusive from a non-diffusive medium. The boundary spreads to infinite in the x-y plane while the diffusive medium spans from $z = 0$ to infinite (figure 2.2). This is used when a large volume respect to source detector separation is being probed and the photon launching and detector positions are placed on the boundary of the medium. It must be noted that the source is not isotropic but directional, being emitted from a fiber. This violates the diffusion approximation since a directional source is not compatible with a random walk type of propagation. Nonetheless, it has been proven that the light source in this system can be approximated as an isotropic light source emitting at a distance $z_+ = l_{tr} = 1/\mu_s'$ from the boundary inside the diffusive medium [59], provided that the source detector separation is large enough respect to l_{tr} (about 0.1 cm).

Boundary conditions must be defined to solve the PDE in this geometry. The first boundary condition that will be here discussed is the partial current boundary condition (PCBC) [84]. It considers the fact that photons that emerge from the surface of the diffusive medium (Σ) do not enter back in the medium. Therefore the light entering the medium at the boundary is only due to the reflection of the radiance that emerges at the boundary into the non-diffusing medium, which depends on the index of refraction mismatch of the two media. It can be derived that in this case the following relation holds [148]:

$$[\Phi(\mathbf{r}, t) - 2A\mathbf{J}(\mathbf{r}, t) \cdot \hat{q}]|_{\mathbf{r}\in\Sigma} = 0 \tag{2.7}$$

where $\mathbf{J}(\mathbf{r}, t)$ is the flux, $\hat{q}$ the unit vector normal to the boundary surface Σ and $A = (1+R_{\text{eff}})/(1-R_{\text{eff}})$, R_{eff} being the effective reflection coefficient to account for the index mismatch between tissue and air. Its analytical expression is quite complex but it can be derived through a linear least square fit. Its value for

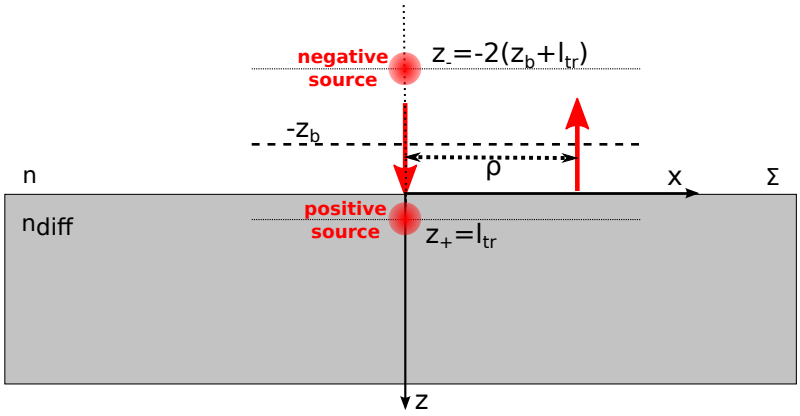

Figure 2.2: Schematic of the extrapolated zero boundary condition for the semi-infinite geometry. Here an infinite surface (Σ) separates a diffusive medium (index of refraction n_{diff}) from a non-diffusive medium (n). Arrows indicate the injection and detection point, separated by the distance ρ. The real source is approximated by an isotropic source at a depth $z_+ = l_{tr}$. The horizontal dashed line at $-z_b$ represent the extrapolated zero boundary surface. A negative source is considered at $z_- = -2(z_b + l_{tr})$. The solution of the PDE for this geometry will be the sum of the contributions from the positive and the negative source.

an index of refraction of n_{diff}=1.4 for the turbid medium and n=1 for non-diffusing medium is R_{eff}=0.493 [84]. By using the Fick's law that relates the flux at the fluence rate, relation 2.7 becomes

$$\left[\Phi(\mathbf{r},t) + 2AD\frac{\partial}{\partial q}\Phi(\mathbf{r},t)\right]\Big|_{\mathbf{r}\in\Sigma} = 0 \tag{2.8}$$

The PCBC is exact but difficult to use. For this reason an approximation has been introduced, called the extrapolated zero boundary condition (EZBC) [52, 148, 170]. Assuming that the derivative of the fluence rate in the non-diffusing medium remains constant at the value at the boundary, *i.e.* the fluence rate is linear, the distance where the fluence rate is null can be extrapolated. This happens at a distance $z_b = 2AD$ from the surface. At this point

the solution for the diffusion equation can be derived using the solution for the infinite medium and the method of the imaginary point sources. The geometry and the distance interesting for the problem are displayed in figure 2.2.

A solution for the fluence rate $\Phi(\mathbf{r}, t)$ is found summing the contribution of a positive source at distance $z_+ = l_{tr}$ inside the diffusive medium and of a negative source at a distance $z_- = -2z_b - l_{tr}$ in the non-diffusive medium. Subsequently, $\Phi(\mathbf{r}, t)$ is then inserted in the formula 2.7 to derive the reflectance $R(\rho, t)$, which is the outward flux at the boundary, [33, 148]

$$R(\rho, t) = \frac{v}{2A}\left(\frac{1}{4\pi Dt}\right)^{3/2} \exp\left(-\frac{\rho^2}{4Dt} - \mu_a v t\right) \times \left[\exp\left(-\frac{z_+^2}{4Dt}\right) - \exp\left(\frac{z_-^2}{4Dt}\right)\right] \tag{2.9}$$

The above equation represents the response of the system when a delta-shaped pulse is injected in the tissue, *i.e.* the Green function of the system. However, the real injected pulse has a finite width in time and this must be taken into account. In this case the reflectance collected $\tilde{R}(\rho, t)$ is the convolution of the Green function with the real pulse shape, referred to as the instrument response function IRF(t) [165].

$$\tilde{R}(\rho, t) = R(\rho, t) \otimes \mathrm{IRF}(t) \tag{2.10}$$

In the next chapter, I will show the shape of such curves and how they depend on the tissue and experimental parameters (figure 3.1).

2.4 Diffusion equation for temporal correlation functions

Photons diffusing in a turbid medium can also be used for probing the dynamics properties of the medium itself, *i.e.* the movement of the scatterers. When a laser beam of uniform intensity travels in a turbid medium, the intensity at the surface is not uniform but presents regions of dark and bright spots [74].

This is because photons have traveled different directions and path-lengths and they can interfere constructively or destructively at the surface. The speckle pattern emerging from biological tissue is not fixed in time, but the intensity of each speckle fluctuates. These fluctuations are affected by the movement of the scatterers, which, in biological tissue, is dominated by the movement of red blood cells [158].

Probing the electric field emerging in a fixed point $\mathbf{r}$, the electric field autocorrelation function $G_1(\mathbf{r},\tau) = \langle \mathbf{E}^*(\mathbf{r},t)\mathbf{E}^*(\mathbf{r},t+\tau)\rangle$ can be calculated. It gives a measurement of the loss of coherence between pairs of photons emerging from the surface with a delay τ. The brackets in the $G_1(\mathbf{r},\tau)$ formula refer to the ensemble average for theory and to time average for experiments. This equivalence requires the system to be ergodic, satisfied if only moving scatterers are present in the probed region [19].

$G_1(\mathbf{r},\tau)$ can be modeled as diffusing in the medium in a random walk manner, like photons. It propagates ballistically until being scattered by a small volume of sample and continues its ballistic propagation until being scattered by another small volume of sample. All these scattering events contribute to the correlation function and it itself depends on the movement of the scatterers in all these single small volumes of sample. Therefore a diffusion equation can be written for the electric field autocorrelation function $G_1(\mathbf{r},\tau)$, analogously to what I showed for the photon propagation in diffusive medium [20]. The set of hypothesis is hence equivalent to what explained for the photon diffusion equation (PDE). In particular photons must be diffusing and this is valid when the mean free transport length l_{tr} is smaller than the dimension of the sample and the absorption length. The problem must be isotropic, therefore the scatterers must be randomly oriented and their dynamics isotropic, like in Brownian motion or random flow. The time assumption requires the correlation time τ to be smaller than the time needed for a scatterer to move a distance equal to a wavelength of light [19].

With this assumption the correlation diffusion equation (CDE) is the fol-

lowing [20]

$$\left[\nabla(D(\mathbf{r})\nabla) - v\mu_a(\mathbf{r}) - \frac{\alpha}{3}v\mu_s' k_0^2\langle\Delta r^2(\tau)\rangle\right] G_1(\mathbf{r},\tau) = -vS(\mathbf{r}) \tag{2.11}$$

$D(\mathbf{r})$ is the photon diffusion coefficient previously seen; the square bracket contains the gradient of the flux of the correlation and the loss of correlation due to absorption and to the movement of the scatterers. α represents the fraction of scattering events which occur from moving particles, $k_0 = \frac{2\pi}{\lambda}$, and $\langle\Delta r^2(\tau)\rangle$ is the mean square displacement of the scatterers. CW source and steady state system are assumed, for this reason no temporal dependence is expressed. In a infinite homogeneous medium and considering a delta-shape CW source at position $\mathbf{r}_s$ of unitary intensity equation 2.11 can be written as [23]

$$\left(\nabla^2 - K^2(\tau)\right) G_1(\mathbf{r},\tau) = -\frac{v}{D}\delta^3(\mathbf{r}-\mathbf{r}_s) \tag{2.12}$$

where $K(\tau) = \sqrt{\frac{v}{D}(\mu_a + \alpha\mu_s' k_0^2\langle\Delta r^2(\tau)\rangle/3)}$

2.5 Solution of the diffusion correlation equation for a semi-infinite homogeneous medium

The process to solve the CDE equation is equivalent to the PDE, but, differently to what has been done in section 2.3, a CW source is being considered. Solution of equation 2.12 in an infinite homogeneous medium with a CW delta shaped source in position $\mathbf{r}_s$ is [52]

$$G_1(\mathbf{r},\tau) = \frac{v}{4\pi D|\mathbf{r}-\mathbf{r}_s|} e^{-K(\tau)|\mathbf{r}-\mathbf{r}_s|} \tag{2.13}$$

As before, we consider a semi-infinite homogeneous medium and the extrapolated zero boundary condition (EZBC), as illustrated in figure 2.2. Summing up contribution of a positive real source at position $\mathbf{r}_s = (\rho = 0, 0, z = z_+ = l_{tr})$ and a negative source at position $\mathbf{r}_{s,-} = (\rho = 0, 0, z = z_- = -2z_b - l_{tr})$ we

have

$$G_1(\mathbf{r},\tau) = \frac{v}{4\pi D}\left[\frac{e^{-K(\tau)r_+}}{r_+} - \frac{e^{-K(\tau)r_-}}{r_-}\right] \tag{2.14}$$

with $r_+ = \sqrt{(z-l_{tr})^2+\rho^2}$ as the distance between the detection point and the positive source and $r_- = \sqrt{(z+2z_b+l_{tr})^2+\rho^2}$ as the distance between the detection point and the negative source.

We have here an analytical solution for the electric field autocorrelation function, however only the normalized intensity field autocorrelation function $g_2(\tau) = G_2(\tau)/G_2(0)$ is measured experimentally, where $G_2(\tau) = \langle I(t)I(t+\tau)\rangle$. To link the intensity and the normalized electric field autocorrelation function $g_1(\tau) = G_1(\tau)/G_1(0)$ we use the Siegert relation [132], valid for ergodic system

$$g_2(\tau) = 1 + \beta|g_1(\tau)|^2 \tag{2.15}$$

β is a parameter that depends on the number of speckles detected and the injection and collection optics. β equals unity for an ideal experiment, while $\beta = 0.5$ for ideal optics when using unpolarized light [230].

The shape of the $g_1(\tau)$ and $g_2(\tau)$ will be shown in the next chapter, as well as their dependence on the tissue and experimental parameters (figure 3.3 and 3.4).

This chapter collected the basic theoretical background for DCS and TRS, the two diffuse optical technologies exploited in this thesis' work. The next chapter will explain the experimental and data analysis strategies relevant for the instrumentation and studies presented in Part 2 and 3 of this thesis.

Chapter 3

Techniques, instrumentation and algorithms

The previous chapter focused on the basic theory of photon propagation into biological tissue, while this chapter is focused on explaining how these models can be used to extract interesting information about tissues.

In time resolved near infrared spectroscopy (TRS), biological tissues are probed by injecting a short pulse of laser light and collecting it after few centimeters of propagation into the tissue. The photon diffusion equation (PDE) solution found in the previous chapter can be used to estimate the optical properties of the tissue from the shape of the collected pulse. It is explained here how to derive information on the oxygenation of the tissue by knowing the absorption coefficient at different wavelengths. It will be also explained how, in diffuse correlation spectroscopy (DCS), information about microvascular blood flow is extracted by measuring the intensity fluctuations in the speckle pattern.

In this chapter, for each of the two technologies, the main requirements for the instrumentation will be explained, while the instrument used in each experiment will be described in details in the following parts of this thesis. Furthermore, how to simulate DCS and TRS data with realistic noise will be

illustrated as well as the data analysis methods used along the thesis.

3.1 Time resolved near infrared spectroscopy

In this technique short pulses of laser light are injected into the tissue. In the experiments run through this thesis the pulse is then collected from the same surface where the light is injected, in a reflectance geometry.

The reflectance (equation 2.9) measured at distance ρ from the source depends on the optical properties and on the ρ itself [148,170]. Figure 3.1 shows how the reflectance changes varying these three parameters. The increase of ρ leads to a shift of the peak to the right and towards lower values, because photons have to travel more to reach the farther detector. An increase of μ_s' has the same effects on the peak, because it is associated to a decrease in the transport mean free path l_{tr}, hence to a increase in the path length traveled by the photons. Increasing μ_a not only lowers the peak, because more photons are absorbed, but it is also reflected in the tail of the curve.

The fact that μ_a and μ_s' changes affect two different properties of the curve, the tail and the center of mass respectively, suggests that from one single curve acquired from a biological tissue we can estimate both μ_a and μ_s' [35].

Estimation of the absorption coefficients at multiple wavelengths allows for extraction of tissue chromophore concentrations [41]. To do so, the linear dependence between the absorption coefficient and the concentration of chromophores is exploited:

$$\mu_a(\lambda) = \sum_{i=1}^{N_c} \varepsilon_i(\lambda) c_i \tag{3.1}$$

where c_i is the concentration of each of the N_c chromophores and $\varepsilon_i(\lambda)$ its molar absorption coefficients.

It has been already mentioned that the relevant chromophores for wavelengths in the range 650 nm-950 nm are oxy- (HbO_2), deoxy-haemoglobin

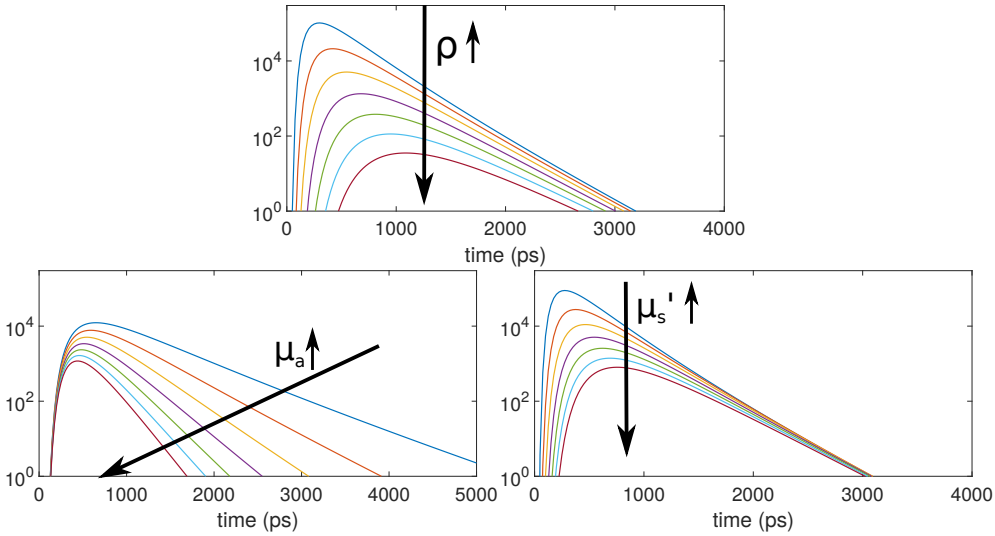

Figure 3.1: Reflectance $R(\rho, t)$ (given by equation 2.9) dependence on the parameters ρ, μ_a and μ_s'. The default value are ρ=3 cm, μ_a= 0.1 cm^{-1} and μ_s'= 10 cm^{-1}. In the upper plot ρ varies between 2 cm and 5 cm by steps of 0.5 cm. In the bottom row, left figure, μ_a varies between 0.05 cm^{-1} and 0.2 cm^{-1} with steps of 0.025 cm^{-1}. While in the right figure μ_s' varies between 4 cm^{-1} and 16 cm^{-1} with steps of 2 cm^{-1}.

(HHb), water and lipids [41]. The number of wavelengths to be used must equal at least the number of chromophores to be estimated. For brain application, water concentration is assumed fixed and constant at literature values, while lipids concentration is negligible. Three wavelengths are commonly used to estimate HbO_2 and HHb concentration, in order to have the system overestimated but still limit its complexity. Wavelengths must be chosen close to the isosbestic point (800 nm) where effect of water and lipid is low and HbO_2 and HHb have a characteristic response (see figure 1) [52]. If water and lipid content must be estimated, for example when the breast is the target tissue, more wavelengths in a wider frequency range must be used [175].

As suggested by equation 3.1 the molar absorption coefficients must be known to estimate the chromophore concentrations. Table 3.1 reports the molar absorption coefficients used in this thesis at the wavelengths of interest [149, 178].

λ (nm)	ϵ_{HbO_2} ($cm^{-1}/\mu M$)	ϵ_{HHb} ($cm^{-1}/\mu M$)	ϵ'_{H_2O} (cm^{-1})
685	6.36×10^{-4}	4.73×10^{-3}	4.72×10^{-3}
760	1.35×10^{-3}	3.57×10^{-3}	2.94×10^{-2}
785	1.70×10^{-3}	2.20×10^{-3}	2.50×10^{-2}
820	2.11×10^{-3}	1.60×10^{-3}	2.41×10^{-2}

Table 3.1: Molar absorption coefficients of HbO_2, HHb [178] and absorption coefficient per volume fraction of water [149] at the wavelengths (λ) of interest.

HbO_2 and HHb concentration (c_{HbO_2} and c_{HHb}) allows for determination of blood volume, *i.e.* concentration of total haemoglobin (tHb) and of oxygen saturation StO_2=c_{HbO_2}/c_{tHb}. The t subscript refers to tissue oxygen saturation, *i.e.* blood oxygen saturation in the microvasculature of the tissue.

3.1.1 Basic instrumentation

Here, I will describe the basic principle of the instrumentation used for a TRS experiment. Light sources employed are near-infrared pulsed lasers, with a full width half maximum (FWHM) of few hundreds of ps [211]. As previously mentioned, three wavelength are used in order to be able to estimate concentration of two chromophores (HHb and HbO_2). Optical fibers in contact with the tissue deliver the laser light from the device to the tissue of interest. Few cm away from the injection fiber another fiber collects the light that has propagated into the tissue. This is detected by a photon detector, traditionally a photocathode-based device [174]. The detector's output is a voltage pulse that marks the arrival time of each photon. This information is fed to a time correlated single photon counting (TCSPC) board that builds the distribution of

time of flight of photons (DTOF), *i.e.* the histogram of arrival time of photons with respect to the injection time of the pulse.

It was previously explained that the instrument response function IRF(t) must be known to do the convolution with the response to a delta-shaped pulse (equation 2.10). The IRF(t) is generally obtained by acquiring a TRS measurement facing the injection and the detector fibers. Therefore it depends not only on the laser source but also on the detection system [202].

3.1.2 Curve simulation with realistic noise

The analytical formulas derived in chapter 2 can be used to simulate TRS data, to which realistic noise can be added. A schematic of the simulation process to obtain simulated TRS curves is depicted in the upper row of figure 3.2, going from left to right.

First of all HbO_2 and HHb concentration values (c_{HbO_2} and c_{HHb}) and percentage of water with respect to the total chromophores concentration (c'_{H_2O}) are defined. This allows to calculate the absorption coefficients, at each wavelength of interest, through equation 3.1:

$$\mu_a(\lambda) = \epsilon_{HbO_2}(\lambda)c_{HbO_2} + \epsilon_{HHb}(\lambda)c_{HHb} + \epsilon'_{H_2O}(\lambda)c'_{H_2O}, \tag{3.2}$$

where ϵ_{HbO_2}, ϵ_{HHb} and ϵ'_{H_2O} are reported in table 3.1. On the other hand, scattering properties are derived from Mie theory, which defines how $\mu'_s(\lambda)$ scales with the wavelength:

$$\mu'_s(\lambda) = a\left(\frac{\lambda}{\lambda_0}\right)^{-b} \tag{3.3}$$

where λ_0 is a reference wavelength set to 600 nm and a and b are parameters that depend on the tissue [153, 157].

At this point, the reflectance in time resolved regime $R(t)$ is derived exploiting equation 2.9, and convoluted with the Instrument Response Function

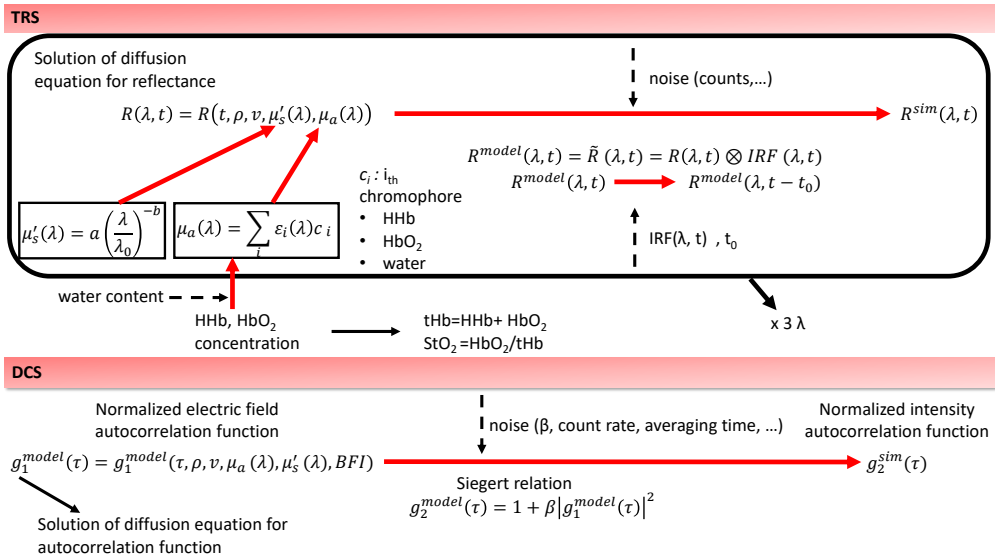

Figure 3.2: Schematic of the flow for TRS (top row) and DCS (bottom row) curve simulation (from left to right). After definition of HbO_2 and HHb concentrations and a and b parameters to obtain $\mu_a(\lambda)$ and $\mu_s'(\lambda)$, reflectance $R(\lambda,t)$ in time domain is calculated and convoluted with the instrument response function IRF(t). Noise is added and the curve is eventually shifted by t_0 to obtain $R^{\mathrm{sim}}(\lambda,t)$. In order to simulate DCS curves, a BFI level is chosen and the normalized electric field autocorrelation curve $g_1^{model}(\tau)$ calculated. Afterwards, the Siegert relation is used and noise is added to derive $g_2^{sim}(\tau)$.

IRF(t) of the system to obtain $R^{\mathrm{model}}(t)$. Next step requires to add realistic noise to obtain the simulated time-resolved curve $R^{\mathrm{sim}}(t)$. This technique is essentially affected by Poisson noise, being the measured light intensity at a certain time determined by counting the photons having the same time of flight [16]. Finally, the simulated curve could eventually be shifted by t_0 in order to simulate instability in the temporal TRS laser position. One curve for each wavelength of interest is generated.

3.1.3 Data analysis

Along the thesis, multiple TRS data analysis methods are used. All of them will be described in this section and for each experiment the method used will be explicitly reported.

To start with, experimental and simulated TRS data can be analyzed following the flow presented in figure 3.2 in the opposite direction (from right to left) respect to the simulation process. The DTOF curve simulated or measured is compared to the model $R^{\text{model}}(t)$ obtained from equation 2.10 by a Levenberg-Marquardt procedure that minimized the least square error between the two [202]. The fitting range includes all points with a number of counts higher than 90% of the peak value on the rising edge of the curve and 1% on the falling edge. The absorption, the reduced scattering coefficient and t_0, the shift of the TRS laser peak, could be considered as fitting parameters [35]. Usually t_0 is kept fixed in the analysis since there is not enough power to estimate three parameters, especially if count rate is not considerably high. This choice will be described for each experiment presented along the thesis. This type of analysis allows for estimation of absolute values of optical properties at three wavelengths. Thanks to this, the absolute concentrations of HbO_2, HHb and tHb and the oxygen saturation StO_2 can be calculated.

TRS data can be analyzed using purely the information about the intensity of the collected pulse and its change during time, that can be related to the change in time of chromophore concentrations. This is a way to simulate what a single-distance CW-NIRS device would measure and it will be referred to as DPF analysis [52]. First, the quantity optical density OD is introduced as $\text{OD} \equiv -ln(I(\mathbf{r}_d, t)/I(\mathbf{r}_s))$, where I refers to the intensity and $\mathbf{r}_s$ and $\mathbf{r}_d$ to the source and detection position, respectively. $I(\mathbf{r}_s)$ is thus the intensity injected. The quantity measured is the change in the optical density at time t respect to baseline

$$\Delta \mathrm{OD}(\lambda, \rho, t) = -ln\left(\frac{I(\mathbf{r}_d, t)}{I(\mathbf{r}_d, t=0)}\right)$$

where ρ is the distance between $\mathbf{r}_s$ and $\mathbf{r}_d$.
Assuming that the changes in the optical properties ($\Delta\mu_a$ and $\Delta\mu'_s$) are small compared to their baseline values (μ_a^0 and $\mu_s'^0$), the optical density expression can be truncated at the first order of the Taylor expansion [52]

$$\Delta \mathrm{OD}(\lambda, \rho, t) = \frac{\partial \mathrm{OD}(\mu_a^0, \mu_s'^0, \rho)}{\partial \mu_a}\Delta\mu_a + \frac{\partial \mathrm{OD}(\mu_a^0, \mu_s'^0, \rho)}{\partial \mu'_s}\Delta\mu'_s \tag{3.4}$$

Subsequently, the change in μ_a can be expressed as a function of the change in chromophore concentrations. Assuming that the scattering is unchanged and defining $d_a \equiv \partial \mathrm{OD}(\mu_a^0, \mu_s'^0, \rho)/\partial\mu_a$, we have

$$\Delta \mathrm{OD}(\lambda, \rho, t) = \sum_{i=1}^{N_C} \varepsilon_i(\lambda)\Delta c_i(t) d_a(\rho, t) \tag{3.5}$$

Usually it is assumed that $d_a(\rho, \lambda) = \mathrm{DPF}(\lambda)\rho$, where $\mathrm{DPF}(\lambda)$ is a differential path-length factor not dependent on ρ [51]. Thanks to equation 3.5, changes in OD at multiple λ can be used to obtain changes in chromophores concentration, specifically HHb and HbO_2.

The last method here explained has been developed in order to improve the sensitivity of TRS measurement to the deeper layers of the probed tissue (e.g. the cerebral cortex when measuring the brain) and reduce the influence of the contribution of the more superficial layers (e.g. the extra-cerebral tissue). Different moments of the DTOF are considered to extract this information [136]. Normalized k^{th} moment of a distribution $f(t)$ are defined as

$$m_k = \frac{\int t^k f(t) dt}{\int f(t) dt} \tag{3.6}$$

When considering an experimental DTOF the integral is substituted by a fi-

nite summation over the time channels [135]. Therefore, the 0^{th} moment corresponds to the total counts of the DTOF

$$m_0 = N_{TOT} = \sum N_i$$

while the first moment is the mean photon time of flight

$$m_1 = \frac{\sum t_i N_i}{m_0}$$

The variance of the DTOF V is defined as the second centralized moment [136]

$$V = m_2 - m_1^2 \qquad m_2 = \frac{\sum t_i^2 N_i}{m_0}$$

The relationship between these three moments and the changes in absorption can be considered linear, provided that the changes are small.

The different moments are used to retrieve absorption changes from different layers of probed tissue, if TRS data are acquired at different source detector separations and if the thickness of each layer is known [136, 137]. In this thesis this method is used considering the probed tissue and the absorption change as homogeneous and considering the linear relation between the absorption change and the change in variance

$$\Delta V = \mathrm{VSF}\Delta\mu_a \tag{3.7}$$

where VSF is the sensitivity matrix, usually obtained by Monte Carlo simulation. In this way, the only improvement in sensitivity to the deeper layer respect to the traditional analysis is purely due to the sensitivity of each moment to the different layers. Interestingly, the variance has found to be more sensitive than the attenuation to the deeper layers respect to the superficial layers [135]. Therefore, this method, even if applied to an homogeneous medium assuming homogeneous change, is more sensitive to changes in the deeper layer

than the DPF analysis, which uses the 0^{th} moment [108].

3.2 Diffuse correlation spectroscopy

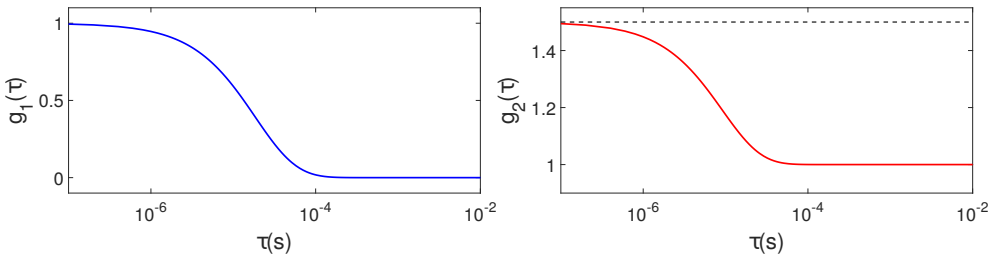

Figure 3.3: Example of electric field autocorrelation function $g_1(\tau)$ (left side) and intensity field autocorrelation function $g_2(\tau)$ (right side). The horizontal dashed line represent the value of $g_2(\tau = 0) = 1 + \beta$.

The diffusion theory for the normalized electric field autocorrelation function $g_1(\tau)$ was explained in the previous chapter, as well as the derivation of the analytical solution in a semi-infinite homogeneous medium [23, 52]. Figure 3.3 reports an example of $g_1(\tau)$ (equation 2.14) and of the intensity field autocorrelation function $g_2(\tau)$, which are linked by the Siegert relation ($g_2(\tau) = 1 + \beta|g_1(\tau)|^2$) [132]. The decay rate of the $g_1(\tau)$ curve depends on the mean square displacement of the scatterer particles $\langle \Delta r^2(\tau) \rangle$ [20]. It has been shown that the Brownian model is the best choice to describe diffusion of red blood cells in the microvasculature, therefore $\langle \Delta r^2(\tau) \rangle = 6 D_B \tau$ where D_B is the particle diffusion coefficient [22, 52]. The parameter extracted from analysis of DCS curve is the blood flow index BFI= αD_B, where α is the ratio of moving scatterers over the total scatterers (see equation 2.14). BFI is proportional to the blood flow and it has units of cm^2/s, being a diffusion coefficient [22]. The dependence of the electric field autocorrelation function $g_1(\tau)$ on the BFI is depicted in figure 3.4 together with the dependence on the

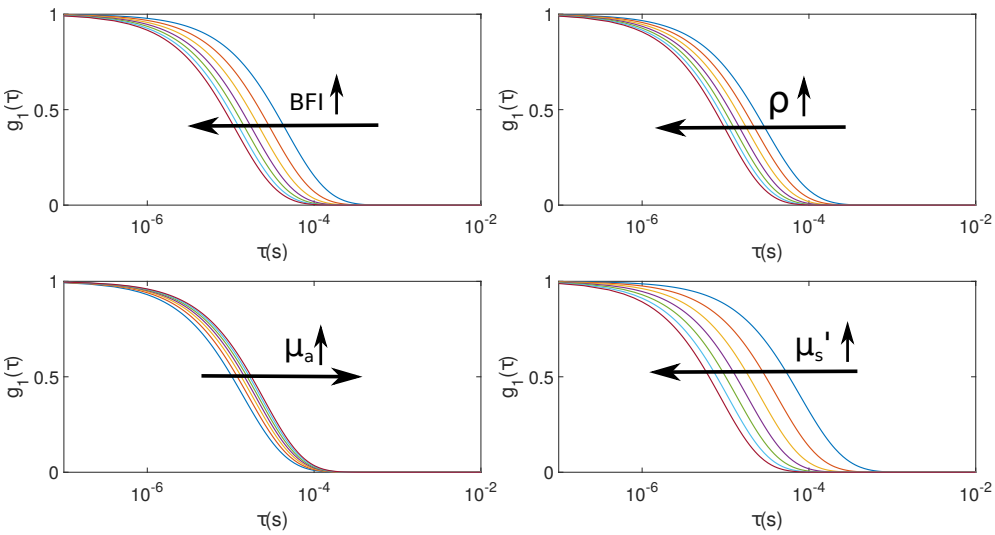

Figure 3.4: Dependence of the electric field autocorrelation function $g_1(\tau)$ given by equation 2.14 on the parameters BFI,ρ, μ_a, μ_s'. The default value are BFI $= 1 \times 10^{-8}\text{cm}^2/\text{s}$, $\rho = 3$ cm, $\mu_a = 0.1$ cm^{-1}, and $\mu_s' = 10$ cm^{-1}. In the upper row, graph on the left, BFI varies between $0.4 \times 10^{-8}\text{cm}^2/\text{s}$ and $1.6 \times 10^{-8}\text{cm}^2/\text{s}$ by steps of $0.2 \times 10^{-8}\text{cm}^2/\text{s}$. While, in the right figure, ρ varies between 2 cm and 5 cm by steps of 0.5 cm. In the bottom row, left figure, μ_a varies between 0.05 cm^{-1} and 0.2 cm^{-1} with steps of 0.025 cm^{-1}. While in the right figure μ_s' varies between 4 cm^{-1} and 16 cm^{-1} with steps of 2 cm^{-1}.

source detector distance ρ and on the optical properties. The higher the blood flow, the higher the BFI and the curve decays faster. The effect is similar for the μ_s', as can be expected from equation 2.14, where the BFI and the square of μ_s' are coupled.

3.2.1 Basic instrumentation

DCS uses a long coherence length laser as the injection source [53]. This property is necessary in order to not influence the coherence of the emerging

photons. In general the coherence length must be larger than the longest path-length traveled by the photons in the tissue. Laser light is coupled to the tissue with a multi-mode optical fiber. Collection is done preferably with a single mode fiber in order to collect the intensity from a single speckle and not lower the beta, to not compromise the signal-to-noise ratio (SNR), as suggested by figure 3.3. The collection fiber is connected to a single photon counting detector, usually a single photon avalanche photodiode (SPAD) [29]. The detector output is a TTL marking the arrival time of each photon. This signal is fed to a hardware correlator, which uses the difference of time of arrival of all pairs of photons to build the intensity autocorrelation function $g_2(\tau)$. The τ is discretized in the hardware correlator by defining time windows, referred to as bins, being τ the center of each bin. The definition of the time bins depend on the correlator design.

3.2.2 Curve simulation with realistic noise

Simulation process for DCS curves is explained in the bottom row of figure 3.2. Analytic expression for the $g_1^{model}(\tau)$, as expressed in equation 2.14 [20, 52], is calculated using the desired BFI value. Once defined the value for β and employing the Siegert relation (equation 2.15), $g_2^{model}(\tau)$ is calculated. Afterwards noise is added to obtain $g_2^{sim}(\tau)$.

An analytic expression for DCS noise is calculated in [231] and gives the standard deviation $\sigma(\tau)$ of $\overline{g_2}(\tau) = g_2(\tau) - 1$ as

$$\sigma(\tau) = \sqrt{\frac{T_m}{t_{av}}}[\beta^2 \frac{(1 + e^{-2\Gamma T_m})(1 + e^{-2\Gamma\tau} + 2m(1 - e^{-2\Gamma\tau})e^{-2\Gamma\tau})}{(1 - e^{-2\Gamma T})} + 2\langle n_m\rangle^{-1}\beta(1 + e^{-2\Gamma\tau}) + \langle n_m\rangle^{-2}(1 + \beta e^{-\Gamma\tau}]^{1/2} \quad (3.8)$$

Here T_m is the correlator bin time interval of the m^{th} bin, t_{av} is the averaging time and $\langle n_m\rangle$ is the average number of photons within the bin time T_m and it can be expressed as $\langle n_m\rangle = IT_m$, with I the measured photon count rate.

Lastly, Γ is the decay rate of $g_1(\tau)$ and it is obtained by fitting the electric field autocorrelation curve with an exponential decay model, as $g_1(\tau) = e^{-\Gamma\tau}$.

3.2.3 Data analysis

Simulated and experimental DCS curves are analyzed following the reverse of the simulation process. From $g_2(\tau)$, $g_1(\tau)$ is obtained through the reverse of the Siegert relation by estimating β from a weighted average of the first three points of the $g_2(\tau)$ curve or assuming a fixed value for it. The retrieved $g_1^{sim}(\tau)$ is then compared to the model, with BFI as the fitting parameter, using as a fitting range the τ where $g_1(\tau) < 0.5$. Optical properties are introduced as input parameters of the analysis process, because it is not possible to accurately extract, from a single DCS curves, both the optical properties and the BFI [48]. Multi-distance or multi-wavelength measurements are necessary for this [61, 207].

In the experiments reported in this thesis, concurrent DCS and TRS measurements are available, therefore optical properties measured by TRS are used in DCS analysis. In principle, this helps the accuracy of BFI estimation compared to using literature values for optical properties.

Part II

BabyLux project

Chapter 4

BabyLux device and its test in laboratory settings

The second part of this thesis reports the work done in relation with the BabyLux project (January 2014 - April 2017, http://www.babylux-project.eu/), whose aim was the development of a robust and accurate device based on diffuse optical technology that could be employed as a neuro-monitor for the premature newborns. In this chapter, the device which integrates DCS and TRS is described, reporting in details the hardware, the software and the probe. Results of tests in laboratory settings, both on phantoms and *in vivo*, developed in order to test the accuracy, precision and stability of the device, are shown.

The device was developed in a collaboration among the technical partners of the project, which defined the task to be developed by each of them. Specifically, PicoQuant GmbH (Berlin, Germany) has provided most of the photonic components for the device. On the other hand, Loop-Competitive Design Network (Sant Cugat del Vallès, Barcelona) has designed and built the external chassis of the device, while Fraunhofer Institute for Production Technology IPT (Aachen, Germany) has designed and built the probe. The main partners involved in the device development were ICFO (Barcelona, Spain), Diparti-

mento di Fisica of Politecnico di Milano (Milano, Italy), and HemoPhotonics (Castelldefels, Spain). In particular, ICFO was in charge of the DCS module, while Politecnico di Milano of the TRS module. On the other hand, HemoPhotonics main role was to develop the integration of the two modules into one device. Since my PhD was co-supervised by ICFO and HemoPhotonics, I have worked in the tasks assigned to the two institutions. In addition, I have followed closely the tasks of the other technical partners, in order to make sure that all the different parts were developed considering the final, integrated device. Finally, once the module components were chosen and the chassis developed, I have built the device under the supervision of HemoPhotonics and I have coordinated and performed the tests in laboratory settings.

The results reported in this chapter are contained in the manuscript Giovannella, M., Contini, D., Pagliazzi, M., Pifferi, A., Spinelli, L., Erdmann, R., Donat, R., Rocchetti, I., Rehberger, M., König, N., Schmitt, R., Torricelli, A., Durduran, T., Weigel, U. M. (2019). "BabyLux device: a diffuse optical system integrating diffuse correlation spectroscopy (DCS) and time resolved near infra-red spectroscopy (TR-NIRS) for neuro-monitoring of the premature newborn brain.", Neurophotonics, *submitted*.

4.1 The device

The BabyLux device can be used in two different configurations. Figure 4.1(a) shows the main unit which contains the optical and electronic components and the screen in its desktop configuration. In addition, the main case can be supported by a custom cart as depicted in figure 4.1(b). The cart consists of an upper drawer for storage purposes and a bottom drawer for an uninterruptible power source (UPS) battery (HAT 1101S, Hectronica, Spain) and for a medical grade isolator transformer (REO España 2002 S.A.). Wheels make the device portable.

A schematic of the main optical and electronics components of the DCS

(a) (b)

Figure 4.1: The BabyLux device in its desktop configuration (a) and on its custom cart (b).

and TRS module are presented in figure 4.2. The TRS module uses three pulsed laser diodes heads at 685 nm, 760 nm and 820 nm (PicoQuant GmbH, Germany, pulse duration < 100 ps and average power < 1 mW), driven by a compact pulse driver at 20 MHz (PicoQuant GmbH, Germany). The electrical connection between the pulse driver and the laser heads have a different length for each of the three lasers in order to introduce different temporal delays between the pulses. Each branch of pulsed light is divided by a 96%/4% fiber splitter (OZ Optics LTD., Canada). The 4% branch of the splitter is attenuated (OZ Optics LTD., Canada), combined into a single fiber connector (Lightech SRL, Italy) and sent directly to the detector (PicoQuant, Germany) (dashed red lines in figure 4.2) to monitor the temporal drift of the TRS lasers.

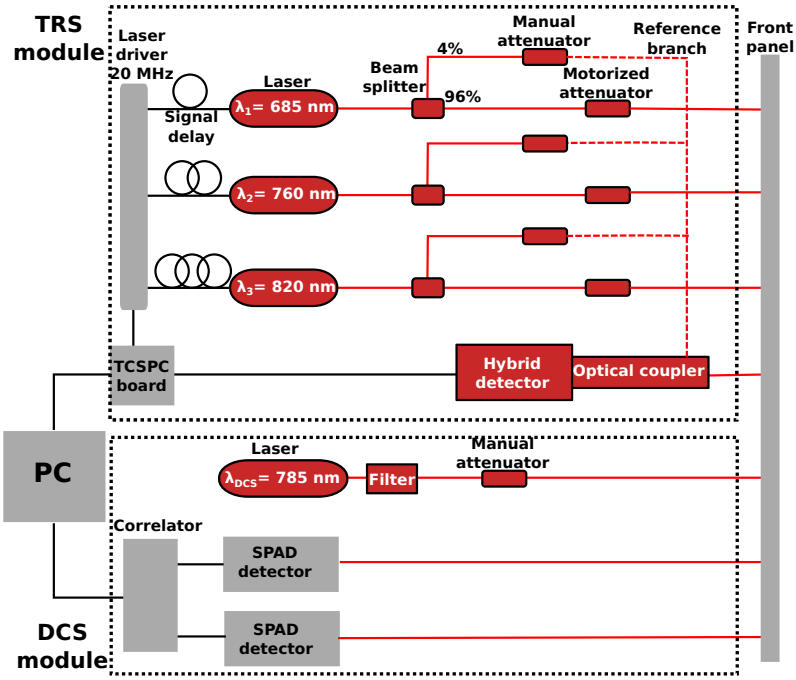

Figure 4.2: Schematic of the principal optical and electronic components of the BabyLux device. Red lines represent optical fibers while black lines are electronic connections.

The 96 % branch is directed to motorized software-controlled attenuators (OZ Optics LTD., Canada) and then, to the front panel of the device. At the detection side, the light is collected by an optical coupler and delivered to the detector (PicoQuant, Germany). The optical coupler combines the signal and the reference branches and contains a triple band pass filter (AHF Analysentechnik AG, Germany) to reduce the detection of the ambient light and the cross talk by the DCS signal. The output of the photon counting detector is fed into the time correlated single photon counting (TCSPC) board (PicoQuant GmbH, Germany) to reconstruct the distribution of time of flight (DTOF) of the detected photons.

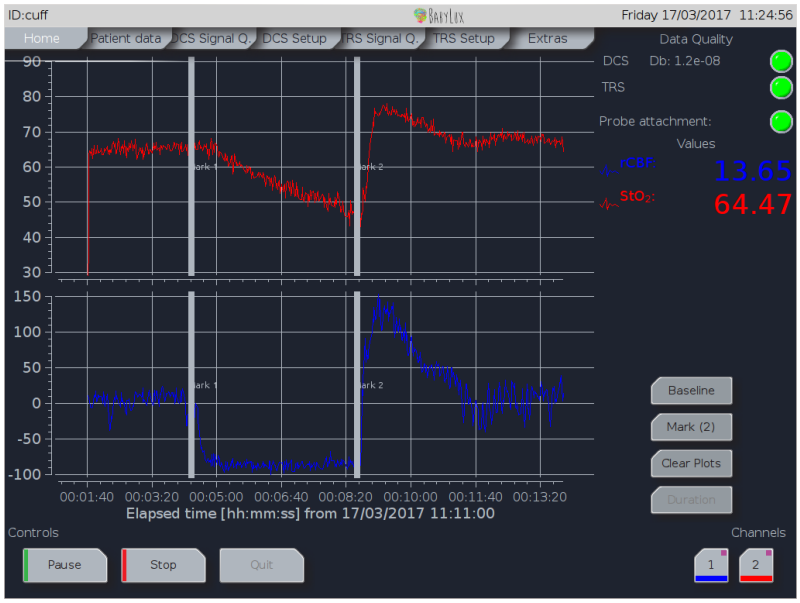

Figure 4.3: Screen-shot of the home window of the device during a cuff occlusion of an adult arm. Time series of the oxygen saturation (top) and relative BFI (bottom) are reported in the time plot. Color dots on the right top corner represent the optical quality of the data collected and the attachment of the probe as monitored by a capacitive sensor placed on the probe.

DCS module employs a long coherence length continuous wave laser at 785 nm at the source side. The laser light passes through a band pass optical filter centred at 780 nm and with 20 nm of band-width (Semrock Inc., U.S.A.) before being connected to the front panel. The filter's purpose is to cut the tails in the spectrum of DCS light, in order to have it fully blocked by the band pass filter in front of the TRS detector. A manual attenuator is adjusted in order to reach a power of approximately 20 mW at the probe head. Two single photon avalanche detectors are used at the detector side (PicoQuant GmbH, Germany). Their input FC/PC connectors are directly placed in the front panel of the device. The detectors' output is a train of TTL pulses marking the arrival

time of each photon. This is fed into a two-channel autocorrelation board (HemoPhotonics S.L., Spain) which calculates the intensity autocorrelation function of each signal.

The device is powered by two power supplies. An advanced technology extended (ATX) medical grade power supply, which provides 180 W, in voltage lines at 3.3 V, 5 V and 12 V, and a 24 V, 3.5 A power supply.

4.1.1 Software

A software developed by HemoPhotonics S.L. (Castelldefels, Spain) is used for the acquisition of both DCS and TRS measurements and for the communication with all the optical and electronic components of the device. The software, written in C++ language and running in Linux (Kubuntu 14.04) environment, was designed in order to be user-friendly. A normal user has access to the home window displayed in figure 4.3. The quality of optical data (for example the signal-to-noise ratio, stability, various parameters) is assessed on-line and is shown to the user with a color code (green for good, orange for intermediate and red for low quality) in the top right corner. The on-line analysis of the data is performed by procedures provided by ICFO for DCS and Politecnico di Milano for TRS and the results of all the hemodynamic parameters and a plot following their time evolution are shown in real-time. An example is given in figure 4.3 from the occlusion of an adult arm. Advanced users can use windows where raw DCS and TRS data curves are shown, whose screen-shots are displayed in figure 4.4. The intensity autocorrelation curve is shown for DCS (figure 4.4(a)) together with a time line of the relative BFI. In TRS data windows (figure 4.4(b)), both the reference and the DTOF peaks are shown for the three wavelengths. The IRF, measured usually before the actual measurement, is also displayed. In the bottom part of the window, results for the optical properties are shown on-line, while in the right side of the screen the DTOF statistic parameters (position of the peak, width, total counts) are reported. From these windows, available for advance users, acquisition and

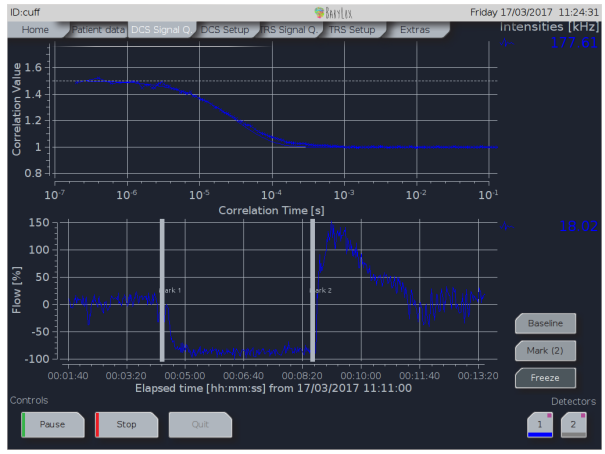

(a)

(b)

Figure 4.4: Windows for the advanced users of the BabyLux device software. (a) Intensity autocorrelation curve and the on-line results for the relative BFI are shown for DCS. (b) DTOF and reference peak for each of the three wavelengths are shown for TRS, together with results for the optical properties.

analysis parameters can be changed.

All the measurements reported in this thesis are acquired with 1 s of averaging/accumulation time.

4.1.2 Probe

		Type	core	NA	Provider
DCS	source	MM	400 μm	0.39	Thorlabs, Germany
	detector	SM	4.4 μm	0.13	Thorlabs, Germany
TRS	source	MM, GIF	62.5 μm	0.21	Thorlabs, Germany
	detector	MM, GIF, POF	1 mm	0.3	FIBERFINN, US

Table 4.1: Launching and detection fibers used in BabyLux probe, both for DCS and TRS. Abbreviations: NA, numerical aperture; MM, multi-mode; SM, single-mode; GIF, graded-index fiber; POF, plastic optical fiber.

Table 4.1 reports the details of the fiber used for light launching and detection in the BabyLux probe. Four fibers are used for light launching, one for DCS and three for TRS, one each wavelength, that shine in the same position. Two single mode fibers are used as the detection fibers for DCS, one for each detector, and one for TRS.

A monolithic small and lightweight probe has been built by Fraunhofer Institute for Production Technology (IPT, Aachen, Germany) to encase all the seven fibers. A picture of the probe is presented in figure 4.5 with a schematic of the source and detector fiber positions. Prisms are used to deflect the light in the perpendicular direction with respect to the surface of the probe which is sealed by sapphire windows to protect fiber tips and prisms. For both DCS and TRS, the distance between source and detector is 15 mm. A second DCS detector is placed at 5 mm distance from the DCS source to follow changes in the superficial extracerebral tissue.

A capacitive sensor is implemented in the probe in order to check whether

this is in contact with the skin. The state of the capacitive sensor is displayed in the home window, as shown in figure 4.3, with green and red to indicate attachment and displacement of the probe, respectively. This is also utilized for laser safety purposes.

The instrument response function (IRF) is measured by placing the probe over a reflective surface. A dedicated case to hold the probe in this position was designed and built.

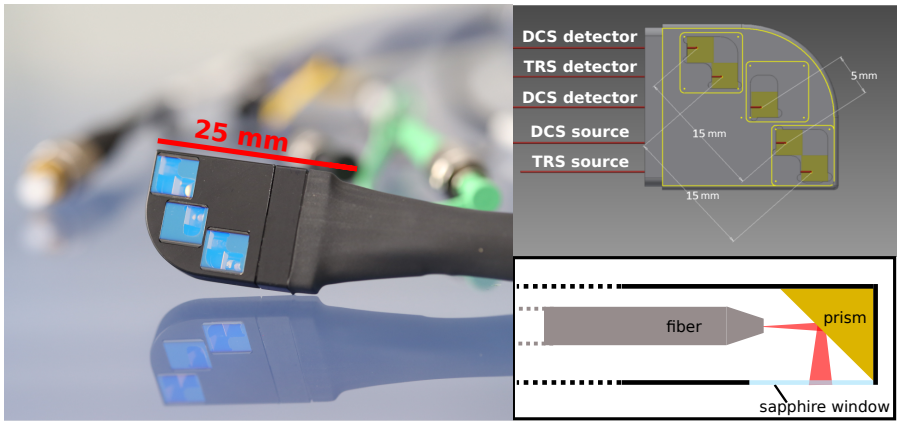

Figure 4.5: On the left side a picture of the head of the probe is shown. On the right side a schematic highlights the positions of the fibers and the distances between the pairs of source and detector fibers. A schematic explaining the mounting of the fibers and the prisms is also presented.

4.2 Tests in laboratory settings

4.2.1 Methods

Phantom tests

MEDPHOT protocol [176] was applied to assess the performance of the TRS module using a phantom kit of twenty-four solid phantoms, with three different

μ_s' (nominal values 5, 10, 15 cm^{-1} at 660 nm) and eight different μ_a (nominal values from 0 cm^{-1} to 0.49 cm^{-1} in 0.07 cm^{-1} steps at 660 nm).

This protocol is divided in five assays, a sixth one was added since relevant for the clinical measurement planned with the BabyLux device. The six assays are the following:

1. *Accuracy:* This test is designed to quantify the error made by the device on the optical property estimation. The error was defined as $\varepsilon = 100 \times (x_{meas} - x_{conv})/x_{conv}$, where x_{meas} was the quantity measured by the BabyLux device and x_{conv} the conventionally true value, obtained by measuring each phantom with a broadband TRS system with high temporal resolution.

2. *Linearity in μ_a and μ_s':* Measured μ_a values were plotted versus the conventionally true ones. In this case the measurements should ideally lie in a line passing trough zero with 45° slope. On the other hand, the measured μ_s' were plotted versus the conventionally true values of μ_a. Therefore, they should ideally lie in three horizontal lines corresponding to the three conventionally true values of μ_s'.

3. *Noise (or precision):* Thirty continuous measurements were acquired on one phantom with nominal optical properties of 10 cm^{-1} for μ_s' (690 nm)and 0.1 cm^{-1} for μ_a (690 nm) at different count level, in the range 10^3-10^8. In order to quantify the precision, we used the coefficient of variation (CV) over the thirty measurements $x = [x_1, ..., x_{30}]$, *i.e.* CV$= 100 \times \sigma(x)/\langle x \rangle$, where $\sigma(x)$ is the standard deviation and $\langle x \rangle$ the averaged value.

4. *Stability:* The same phantom used in the previous point was measured for approximately 10 hours after the device had been switched on. The time series of the derived optical properties was plotted to check the time necessary for reaching their final values, *i.e.* the warming up of the device, and to check the eventual presence of drifts or fluctuations.

5. *Reproducibility:* The same phantom was measured over five different days, at the same experimental conditions. Averaged value of optical properties over all the five days was calculated as well as the percentage deviation on each day with respect to them.

6. *Reproducibility over probe replacement:* The same phantom was measured over five different days, at the same experimental conditions. The probe was placed on the phantom, thirty measurements were acquired, then the probe was lifted, placed back on the phantom surface and other thirty acquisitions run. This was done until six sets of measurement were acquired. The coefficient of variation (CV) over the six replacements was calculated for each of the five days.

All the described measurements were acquired collecting 10^5 photon/s, if reachable, apart from point (3).

In order to test the DCS module, a liquid phantom provided by HemoPhotonics S.L., Spain [169] was employed in the last three points of the above protocol (*stability*, *reproducibility* and *reproducibility over probe replacement*). This phantom had nominal optical properties of 0.17 cm^{-1} and 7 cm^{-1} at 785 nm and a nominal particle diffusion coefficient of $1{\times}10^{-8}cm^2/s$.

Finally, to quantify possible mutual cross-talk between TRS and DCS, we have acquired thirty TRS and DCS measurements on a same phantom both simultaneously (*i.e.* DCS on and TRS on) and independently (*i.e.* DCS on and TRS off, or *vice versa*). Optical and dynamic properties are estimated in the two modes and mean and standard deviation of the thirty measurements calculated.

In vivo protocol

A protocol for arterial cuff occlusion of the arm was implemented on healthy adult volunteers to test the device in relevant settings closer to the operational

ones. This test was previously proposed as a controlled and easy to repeat test to check the *in vivo* performance of cerebral oximeters [97].

The studies were approved by the ethical committee of the Hospital Clinic Barcelona. Each subject signed an informed consent and the study was conducted according to the principles of the Declaration of Helsinki. The inclusion criteria was a skin-fold thickness of less than 8 mm as measured by a skin caliber. The probe was placed on the upper part of the flexor muscle of the lower arm. After two minutes of rest, arterial cuff occlusion at 230 mmHg was maintained for six minutes. The cuff was deflated and seven more minutes were recorded. This protocol was repeated three times sequentially for each subject in the same session.

Data analysis

In the following section, results from off-line data analysis are explained. The fitting procedure explained in chapter 3 was implemented both for TRS and DCS. Few words must be spent on t_0, the shift of the TRS laser peaks. The time t= 0 ps represents the photon launching time and it is considered as the peak of the IRF in the realistic case when the injected pulse is not a delta pulse. This holds true if IRF is measured by directly facing the source and detector fibers [165]. Since we have measured the IRF in a reflectance geometry, with some distance from the reflecting surface, a shift of the peak t_0 must be considered. This parameter was calibrated by measuring a solid phantom with known optical properties. We have used the model explained above for the fitting procedure and a spectral fit was performed by defining a spectral constraint for the reduced scattering coefficient according to the Mie theory. Specifically, $\mu_s'(\lambda) = a(\lambda/\lambda_0)^{-b}$ [105, 153, 157] where λ_0 is a reference wavelength and a and b are parameters that depend on the scatterers size and density. Curves at the three wavelengths were then fitted simultaneously considering $\mu_a(\lambda)$, a, b and t_0 as fitting parameters in order to define the best value for t_0.

Once t_0 was obtained for this system, the measured DTOF could be shifted with respect to the IRF and analyzed by fitting the DTOF with the model $\tilde{R}(t)$. An estimation of optical properties ($\mu_a(\lambda)$ and $\mu'_s(\lambda)$) for each wavelength was derived.

The same procedure was implemented in the on-line data analysis. Therefore the same results would have been obtained, provided that the same parameters were selected in the software.

As for the *in vivo* measurement, the response in each of the three occlusions was characterized by extracting the level of BFI and StO_2 reached during occlusion and after releasing the cuff. In order to test whether the response differed over multiple occlusions, a linear mixed effects (LME) model for those two variables was built with number of occlusion as fixed effect and subject as random effect.

4.2.2 Results and discussion

Figure 4.6 shows examples of IRFs and DTOFs acquired at the three wavelengths with the BabyLux device from a solid phantom. The curves resulted from the analysis are also shown and the vertical bars highlight the range used for the analysis. Analogously, g_2 measured from a liquid phantom by the DCS module is also shown, together with the results of the fit analysis and the range used for the analysis.

Phantom tests

As explained in the Methods section, the MEDPHOT protocol [176] was applied to assess performance of the TRS module. I will start explaining results of the five assays of this protocol, plus the one added specifically for this device.

1. **Accuracy**. Tables 4.2 and 4.3 report the error in optical properties estimation with respect to the conventionally true values. Value of interest for application in infant neuro-monitoring is 0.2 cm^{-1} for μ_a and 7 cm^{-1}

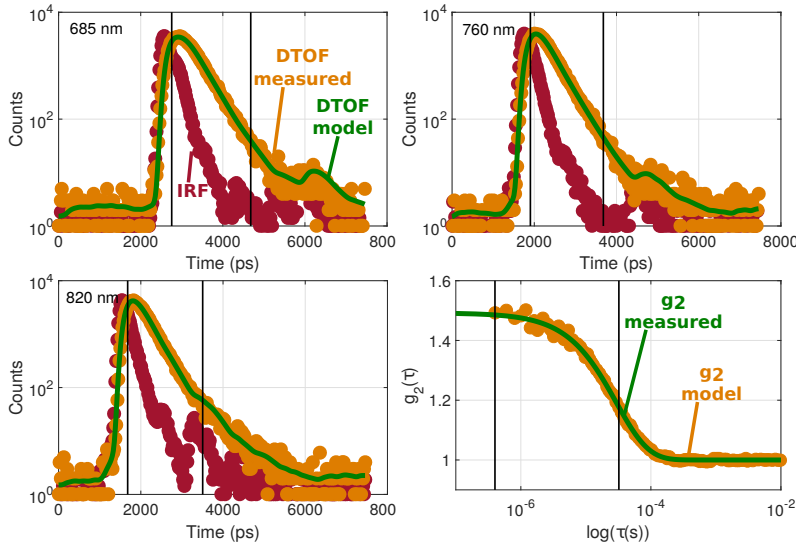

Figure 4.6: IRF and example of DTOF (collected from a solid phantom) are shown for the three wavelengths (a) 685 nm, (b) 760 nm, (c) 820 nm. The solid line represent the results of the fitting procedure. In (d), a DCS measured normalized, intensity auto-correlation curve collected from a liquid phantom is depicted, together with the results of the model, solid line. The black vertical lines highlight the region used for the fitting procedure.

for μ_s' [39]. Focusing on the phantom with optical properties of this range we find an accuracy of around 6-8% for μ_a at 685 nm and 760 nm and of about 8% at 830 nm. While the deviation for μ_s' is around 10% at the three wavelengths. This is comparable with other TRS devices performance [176] and with the intrinsic limits of employing the photon diffuse equation [35, 202]. It was fundamental to assess the accuracy in estimation of the optical properties for different reasons. Firstly, the absolute measurement of HHb and HbO_2 concentrations and consequently of StO_2 depends on the possibility to measure the absolute values of the optical properties of the tissue, in other words, on decoupling μ_a and

μ_s'. In addition, the optical property values are needed for the blood flow index estimation, since they are the input parameters of DCS analysis. It must be highlighted that the accuracy is tested not towards the true optical properties but towards the conventionally true values. This is motivated by the fact that assessing the true optical properties is particularly challenging, mainly because the accurate characterization of optical properties of the individual constituents of the phantoms is not feasible [176]. The conventionally true values have been obtained measuring the phantoms with a tunable multi-wavelength system. Optical properties were estimated with a resolution of 5 nm and using a spectral fit and measurements over several months have been averaged. In spite of this, the conventionally true values cannot still be considered as the true optical properties, therefore the MEDPHOT protocol tests a device accuracy towards the state-of-the-art and not the true values [176]. In addition, the accuracy in *in vivo* measurements is a different and more complicated issue. This can be assessed by testing the device against gold-standards (chapter 6 for the DCS) or checking the performances in clinical settings (chapter 7).

2. **Linearity in μ_a and μ_s'.** Left column of figure 4.7 shows the linearity of the system for absorption measurement by showing the behavior of μ_a estimation with respect to the conventionally true values for μ_a. The black line represents the expected values, therefore the distance of each point from this line gives an additional indication of the accuracy of the estimation. The right column of the same figure (figure 4.7) reports the measured μ_s' with respect to the conventionally true values for μ_a in order to show the coupling of μ_s' to μ_a. The horizontal lines represent the expected values for μ_s'. Linearity is good for low values of μ_a, while a coupling between μ_a and μ_s' affect results at higher values of absorption.

Error in μ_a			
685 nm			
	μ_s' conventionally true		
μ_a conventionally true	5.9 cm^{-1}	10.7 cm^{-1}	14.2 cm^{-1}
0.01 cm^{-1}	-42%	-2%	-5%
0.07 cm^{-1}	-6%	-5%	-5%
0.14 cm^{-1}	-9%	-10%	-13%
0.20 cm^{-1}	-4%	-6%	-8%
0.27 cm^{-1}	-6%	-8%	-10%
0.33 cm^{-1}	0%	-10%	-13%
0.40 cm^{-1}	-4%	-8%	-13%
0.46 cm^{-1}	0%	-2%	-11%
760 nm			
	μ_s' conventionally true		
μ_a conventionally true	5.20 cm^{-1}	9.50 cm^{-1}	12.70 cm^{-1}
0.01 cm^{-1}	-44%	-29%	33%
0.07 cm^{-1}	-13%	-6%	-8%
0.13 cm^{-1}	-10%	-8%	-9%
0.19 cm^{-1}	-7%	-8%	-7%
0.25 cm^{-1}	-8%	-6%	-8%
0.29 cm^{-1}	1%	-4%	-7%
0.36 cm^{-1}	-1%	-3%	-8%
0.42 cm^{-1}	-1%	-2%	-8%
820 nm			
	μ_s' conventionally true		
μ_a conventionally true	4.70 cm^{-1}	8.70 cm^{-1}	11.70 cm^{-1}
0.01 cm^{-1}	-88%	-1%	7%
0.07 cm^{-1}	-26%	-16%	-16%
0.12 cm^{-1}	-16%	-12%	-12%
0.18 cm^{-1}	-16%	-12%	-12%
0.23 cm^{-1}	-11%	-9%	-9%
0.28 cm^{-1}	-5%	-10%	-11%
0.34 cm^{-1}	-6%	-10%	-10%
0.39 cm^{-1}	-5%	-3%	-9%

Table 4.2: Error in μ_a estimation from BabyLux device compared to conventionally true values of the twenty-four solid phantoms measured.

Error in μ_s'			
685 nm			
	μ_s' conventionally true		
μ_a conventionally true	5.9 cm^{-1}	10.7 cm^{-1}	14.2 cm^{-1}
0.01 cm^{-1}	-17%	-21%	0%
0.07 cm^{-1}	-9%	-7%	-6%
0.14 cm^{-1}	0%	-5%	-3%
0.20 cm^{-1}	5%	-8%	-5%
0.27 cm^{-1}	5%	-5%	-7%
0.33 cm^{-1}	11%	-1%	-11%
0.40 cm^{-1}	17%	-4%	-14%
0.46 cm^{-1}	26%	-1%	-13%
760 nm			
	μ_s' conventionally true		
μ_a conventionally true	5.20 cm^{-1}	9.50 cm^{-1}	12.70 cm^{-1}
0.01 cm^{-1}	-17%	-21%	2%
0.07 cm^{-1}	-9%	-8%	-8%
0.13 cm^{-1}	-1%	-6%	-3%
0.19 cm^{-1}	5%	-9%	-5%
0.25 cm^{-1}	3%	-6%	-7%
0.29 cm^{-1}	7%	-2%	-10%
0.36 cm^{-1}	19%	-3%	-12%
0.42 cm^{-1}	24%	-3%	-10%
820 nm			
	μ_s' conventionally true		
μ_a conventionally true	4.70 cm^{-1}	8.70 cm^{-1}	11.70 cm^{-1}
0.01 cm^{-1}	-15%	-19%	-1%
0.07 cm^{-1}	-12%	-10%	-7%
0.12 cm^{-1}	-4%	-9%	-5%
0.18 cm^{-1}	-3%	-10%	-7%
0.23 cm^{-1}	-3%	-10%	-8%
0.28 cm^{-1}	1%	-5%	-9%
0.34 cm^{-1}	9%	-10%	-13%
0.39 cm^{-1}	14%	-6%	-12%

Table 4.3: Error in μ_s' estimation from BabyLux device compared to conventionally true values of the twenty-four solid phantoms measured.

3. **Noise (or precision)**. The coefficient of variation (CV) of optical property measurement at different count levels in a logarithmic scale are reported in the top row of figure 4.8. A value of 1% is reached with 5×10^5 counts. Due to the Poisson nature of the photon noise, the CV is expected to decrease as the square root of the counts. In order to test this, the logarithmic transformation of CV versus the counts, as plotted in figure 4.8 was tested for linear regression. For each wavelength and for both μ_a and μ_s', the 95% confidence interval of the slope contains -0.5, i.e. a square-root dependence, as expected.

4. **Stability**. Optical properties estimated from eight hours of measurement right after the starting of the device are reported in the bottom row of figure 4.8. The horizontal lines represent a range of $\pm3\%$ with respect to the average values calculated in the last hour of measurement. A warm up period of one hour is thus identified. After the warm up period no shifts or deviations are detected in the results.

5. **Reproducibility**. Table 4.4 reports results of the repeatability assay over different days, where the same solid phantom was measured under the same experimental condition. The deviation between different days of measurement is low, with a maximum value of 5% reached only in one day.

6. **Reproducibility over probe replacement**. Table 4.4 reports results for repeatability over replacements of the probe as well. This test was motivated by the fact that poor reproducibility in this scenario is a major drawback of current NIRS technologies. CV over replacements is always less than 2.5%.

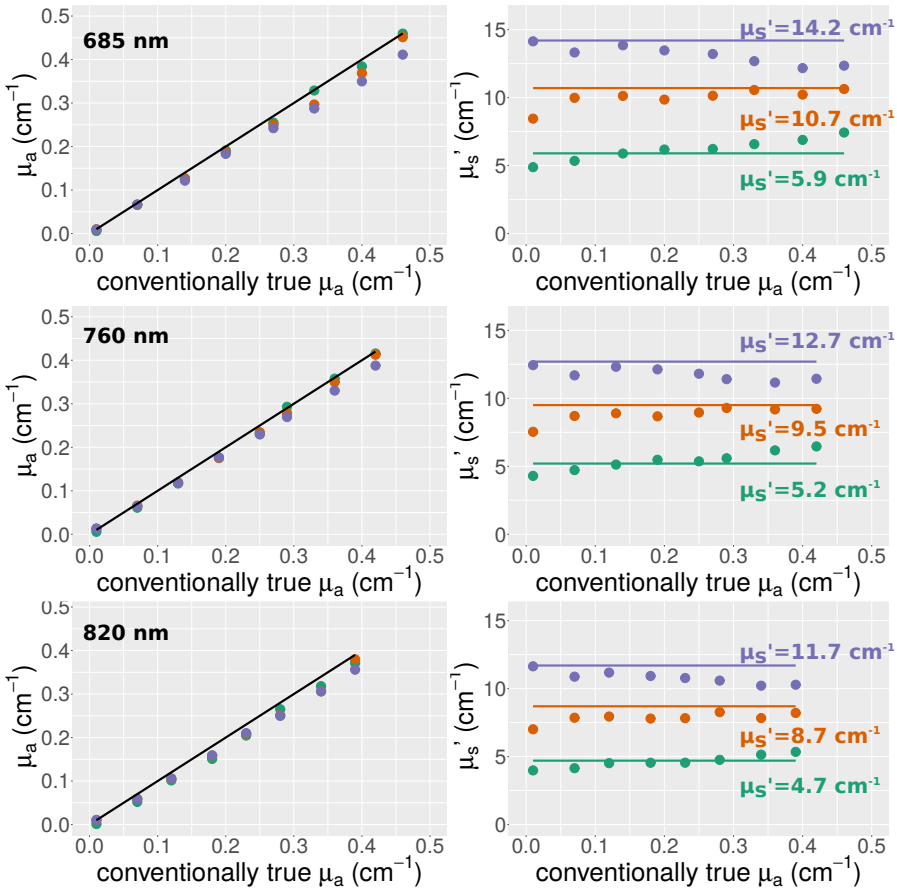

Figure 4.7: Optical properties retrieved from a series of twenty-four solid phantoms, built with three different levels of reduced scattering coefficient and eight levels for absorption are shown. Each row represents one wavelength (λ). In the left column the measured μ_a are plotted versus the conventionally true μ_a, different colors correspond to the different level of μ_s'. The black line represents the expected values. The right column reports the measured μ_s' with respect to the conventionally true μ_a. The horizontal lines represent the conventionally true μ_s'.

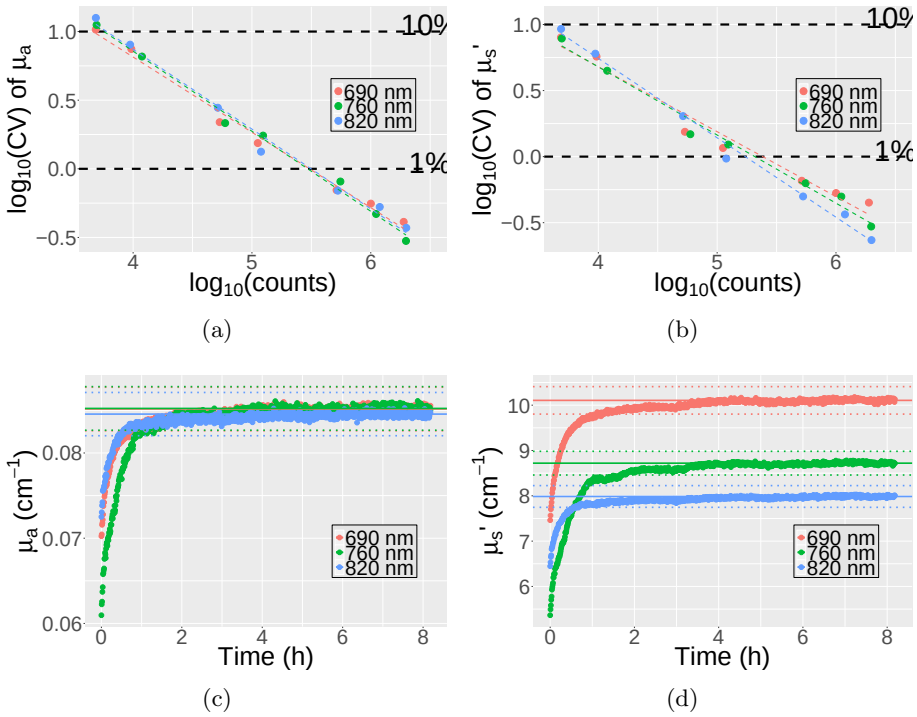

Figure 4.8: Top row reports the CV of μ_a and μ_s' estimation over thirty continuous measurements at different count levels. Both axis are in logarithmic scale, dashed lines represent the linear regression, whose slope is -0.5 for all of them, as expected by Poisson photon noise. 1% stability level is reached at $5{\times}10^5$ counts for the μ_a and already at 10^5 counts for the μ_s'. The bottom row reports results of μ_a and μ_s' over eight hours after turning on the device for the three wavelengths. The dashed horizontal lines represent the $\pm 3\%$ range of the average value obtained from the last hour of measurement, that is reached after one hour of measurement.

Absorption coefficient μ_a				
λ	Day	average value	deviation from average	CV over replacement
685 nm	1	0.078 cm^{-1}	-0.5%	2.3%
	2		-2.4%	2.5%
	3		5.4%	1.9%
	4		0.1%	2.5%
	5		-2.6%	1.6%
760 nm	1	0.076 cm^{-1}	-0.04%	2.2%
	2		-2.7%	2.4%
	3		5.9%	2.5%
	4		-0.2%	2.2%
	5		-5.2%	2.5%
820 nm	1	0.073 cm^{-1}	-0.6%	2.3%
	2		-0.2%	1.9%
	3		5.1%	2.0%
	4		0.9%	2.1%
	5		-5.1%	1.9%
Scattering coefficient μ_s'				
λ	Day	average value	deviation from average	CV over replacement
685 nm	1	11.5 cm^{-1}	1.2%	1.8%
	2		-0.6%	1.9%
	3		0.9%	1.5%
	4		0.2%	1.9%
	5		-1.7%	1.3%
760 nm	1	9.7 cm^{-1}	1.1%	1.6%
	2		0.2%	1.5%
	3		1.0%	2.0%
	4		-0.2%	1.5%
	5		-3.8%	1.7%
820 nm	1	8.7 cm^{-1}	0.8%	1.3%
	2		2.8%	1.4%
	3		-0.5%	1.4%
	4		0.7%	1.6%
	5		-3.8%	1.3%

Table 4.4: The same solid phantom was measured on five different days, acquiring six measurements per day replacing each time the probe on the surface of the phantom. In the table, for each wavelength and each day, the average value of optical properties is presented, together with the percentage deviation from the average values and the coefficient of variation (CV) over replacement.

A standard procedure to assess the accuracy of the DCS measurement does not exist, mainly due to the complexity of making a stable liquid phantom. A mixture of water, ink and lipid emulsions is usually used. Few techniques have been considered to change the particle diffusion coefficient in a controlled way, from changing the viscosity of the medium, its temperature or adding forced motion by pumps [23, 34, 70, 120, 140]. However the phantoms for dynamic properties are still to be improved. Therefore only stability and reproducibility was tested for both modalities.

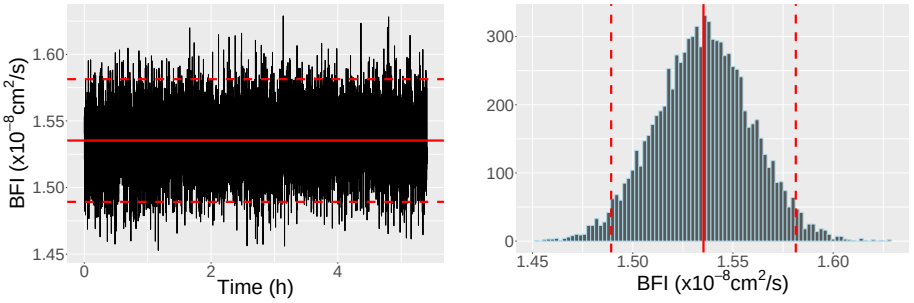

(a) (b)

Figure 4.9: BFI measurement of a liquid phantom by DCS over hours (a) and its histogram (b). The red continuous line indicates the average value, while the dashed line represent the ±3% range.

- **Stability**. The results of measurement on a liquid phantom over five hours are reported in figure 4.9. Retrieved BFI values show no trend over time and the coefficient of variation over the whole period is 1.5%.

- **Reproducibility**. The deviation from average value of BFI between days is reported in table 4.5. This is larger than those for optical properties, reaching 8%. It must be noted that variability of liquid phantom conditions plays an important role in dynamic property measurement,

mainly because the measured diffusion coefficient depends on the environmental conditions such as the temperature [55].

- **Reproducibility over probe replacement**. Results for CV of BFI over replacements, reported in table 4.5, are very good and similar to those obtained for TRS.

BFI			
average value	Day	deviation from average	CV over replacement
1.76×10^{-8} cm^2/s	1	-8.3%	1.5%
	2	-1.3%	1.5%
	3	7.0%	1.0%
	4	0.1%	0.8%
	5	2.5%	1.0%

Table 4.5: The same liquid phantom was measured on five different days, acquiring six measurements per day replacing each time the probe on the surface of the phantom. The table reports the average value obtained for BFI and, for each day, the deviation from the average value and the CV over replacement.

The final test performed on phantoms was aimed at assessing whether each module influences the other, to evaluate potential cross-talk, since DCS and TRS measurement are acquired simultaneously. Table 4.6 compares the results of DCS measurements on the same liquid phantom both in presence of TRS light shining from the probe and without TRS light. Intensity, β parameter and BFI are equivalent in the two configurations, within the standard deviation of the measurement. This is also confirmed for TRS. Table 4.7 shows the equivalent results for optical properties measured by TRS with and without DCS light shining from the probe. The results in the two modes correspond to each other within the standard deviation of the thirty measurements. The increase of background must be related to the counts in all the 2048 channel,

i.e. an increase of only 2 counts per channel on average, which does not affect the measurement.

TRS light	$BFI \times 10^{-8}$	β	Intensity (kHz)
OFF	1.95 (0.09)	0.50 (0.01)	153 (2)
ON	1.90 (0.08)	0.49 (0.01)	154 (1)

Table 4.6: The same liquid phantom was measured with and without TRS laser light shining from the probe, acquiring thirty curves. The table reports the mean BFI, β and intensity with the standard deviation (in brackets) over the thirty measurements. This shows that TRS light does not affect DCS measurements.

λ	DCS light	μ_a (cm^{-1})	μ'_s (cm^{-1})	Total background counts
685 nm	OFF	0.243 (0.002)	9.49 (0.06)	6144
	ON	0.242 (0.002)	9.42 (0.09)	8192
760 nm	OFF	0.232 (0.002)	8.38 (0.06)	4096
	ON	0.232 (0.003)	8.35 (0.09)	8192
820 nm	OFF	0.215 (0.002)	7.55 (0.05)	4096
	ON	0.214 (0.002)	7.49 (0.07)	8192

Table 4.7: Thirty TRS curves were acquired from a solid phantom with nominal properties of μ_a=0.27 cm^{-1} and μ'_s=10 cm^{-1} at 660 nm with and without DCS laser light shining from the probe. The table reports the mean optical properties with the standard deviation (in brackets) over the thirty measurements, as well as the total background noise, registered in all the 2048 channels.

In vivo protocol

Six subjects (three females, aged 23 to 29 years) were recruited for the cuff occlusion protocol of adult arm, designed in order to test the device during *in vivo* measurement and its performance when blood flow and saturation levels vary over a dynamic and wide range. The skinfold thickness of the overlying

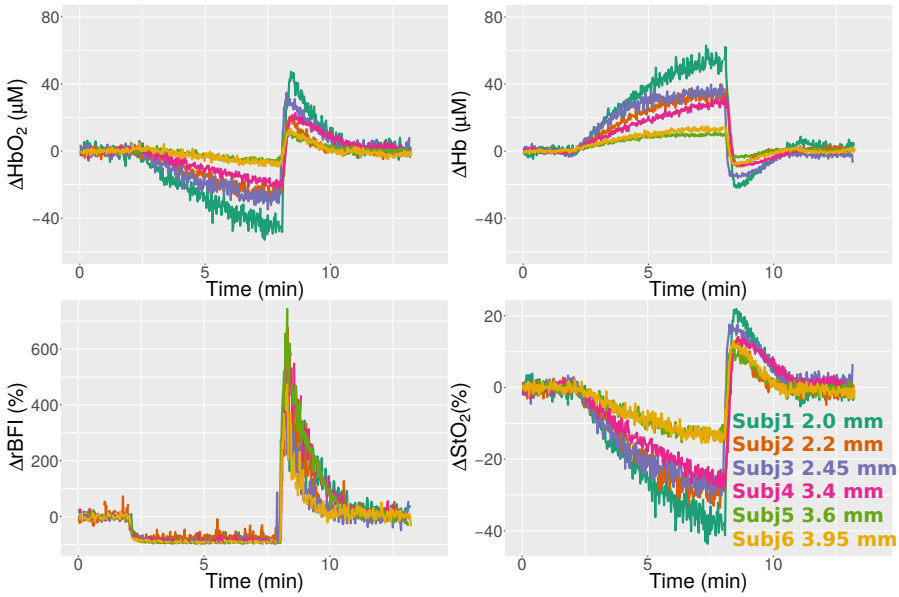

Figure 4.10: Time series of changes of HHb, HbO_2, StO_2 and rBFI during the cuff occlusion protocol. Curves are reported for each subject, who are color coded. Legend identifies the thickness for the superficial layer for each subject.

tissue ranged from 2 mm to 4 mm. The each repetition of occlusion did not differ from the others, as confirmed by the LME model ($p>0.05$). For this reason, the three repetitions of the protocol were averaged for each subject. Figure 4.10 reports the haemodynamic time series during the protocol for the six subjects, each of them represented by a different color. The legend reports the superficial layer thickness as assessed by the skinfold thickness. The deoxy-hemoglobin (HHb) concentration increased during the arterial occlusion, with a median increase over the population at the end of occlusion period of 32.4 μM (14.1 μM, 37.6 μM). Here the numbers in brackets are the I and III interquantile. This notation will be kept for the other parameters in this section. On the other hand, the oxy-hemoglobin (HbO_2) concentration decreased during the occlusion by -24.0 μM (-31.0 μM and -8.9 μM) as the median over

the population at the end of the occlusion period. These changes resulted in a decrease of StO_2 of -28.2% (-31.6%,-14.7%). Concurrently, the percent change of BFI (ΔrBFI) at the end of the occlusion was 85% (79%,89%) as the median over the population.

After releasing the cuff, HHb changed by -8.9 μM (-15.1 μM, -7.6 μM) and HbO_2 by 20.4 μM (12.1 μM,30.9 μM) with respect to the initial value. Consequently, StO_2 increased with respect to the initial value by a median value of 12.9% (11.9%, 16.6%) within 30 s after the release of the occlusion, this was followed by a recovery to baseline. Blood flow increased releasing the cuff, reaching a percentage change of 490% (380%, 510%) as the median over the sample population with respect to the initial baseline value. All these values tended towards recovery within two minutes after the release of the cuff.

Overall, the hemodynamic parameters changed in the expected manner. Within all the subjects, a wide range of level for StO_2 was reached during the occlusion period reflecting, presumably, differences in the oxygen metabolism of the muscles of those subjects. Furthermore, the decrease of StO_2 was dependent on the measured thickness of the superficial layer, which is not surprising since the source detector separation is optimized for probing relatively shallow regions, such as the infant brain. During the occlusion the reduction of StO_2 was larger in subjects with thinner superficial layer, since the active muscle tissue occupied a larger percentage of the probed volume respect to subjects with thicker superficial layer. StO_2 decrease reached 40% in the subject with a skin and adipose tissue layer of 2 mm. It has been proven that for thin superficial layer (7 mm for a source detector separation of 20 mm), the absorption properties retrieved using the model for homogeneous level are independent on the changes of the upper layer [72]. Even if this holds true, StO_2 changes depend on the amount of muscle tissue probed by the optics, which consumes more oxygen respect to the skin and adipose tissue, as it was demonstrated in a previous work changing the source detector separation on the same subjects [226].

In our case, for the blood flow we did not distinguish levels reached at the cuff release in the different subjects, the response during the hyperaemia was indeed homogeneous within the subjects. It increased by 490% as the median over the sample population with a narrow interquartile range of (380%, 510%). In the previously cited work, the blood flow level of hyperaemia was actually dependent on the source detector separation [226]. It must be noted that the occlusion in the mentioned work was kept for less time (3 minutes instead of 6 minutes) and the blood flow increase was far lower than in our protocol (3-fold increase instead of 5-fold). Different durations of occlusion may be the source of the discrepancy and the fact that the hypoxia here was more extreme due to the longer occlusion may be the cause of the response which was not dependent on the superficial layer thickness. Since it has been proven that the depth sensitivity of DCS is higher than CW-NIRS and the contrast to noise ratio of the deeper layer change equivalent [196], we do not expect DCS to be less sensitive to the muscle haemodynamics than TRS in this measurement.

4.3 Conclusions and outlook

The work presented in this chapter demonstrates that the BabyLux device can be a good candidate for monitoring cerebral haemodynamics in the infant brain for two reasons. First, by using DCS, it has a direct measurement of the blood flow to the cerebral tissue. Instead of having information only on the consumption of oxygen, as done by NIRS that measures blood oxygen saturation, the BabyLux device provides a direct independent measurement of the supply of oxygen. Secondly, TRS allows for the absolute measurement of the optical properties and, consequently, of HHb and HbO_2 concentrations and StO_2.

The laboratory tests showed good performance of the BabyLux device. The estimation of optical properties was accurate and precise. The results were stable over several hours of functioning and they were repeatable within

days and replacement of the probe. Good performance in the dynamic range and *in vivo* measurement has been proved by an arterial cuff occlusion of the adult forearm.

In the future, technological development can be pushed forward and more laboratory tests can be thought. For example the layered structure of the head can be considered as well as the role of the cerebral spinal fluid (CSF) with quite different optical properties from the tissue ones. This is currently not trivial and efforts are being done by the diffuse optical community to develop new realistic phantoms [44]. In addition, more distances between source and detector fibers could be considered. It is not straightforward to define the best distance to choose, considering the trade-off between reaching deeper regions and the signal to noise ratio or geometry of the head. Furthermore, studies are still ongoing regarding the sensitivity to the brain, which seems to be dependent on the specific method used [26,147,196]. Nonetheless the BabyLux consortium aimed at developing a prototype for a medical device, based on the start of the art of DCS and TRS technology. The device's performance was tested considering one of the current available protocols for TRS devices and translating this to DCS. Surely these tests assess the device performances in a controlled and ideal scenario and set the realistic limits to be expected from more complex clinical studies. However, this is only a starting point and more work has been developed within this thesis work to test the device. Firstly, the device precision and accuracy limits were investigated at different experimental and analysis configuration through realistic simulated data (chapter 5). Then, the cerebral blood flow measurement were validated towards ^{15}O - water PET in a piglet model (chapter 6). Finally, the device was tested in a more realistic scenario, performing measurement on infants over a dynamic range and to assess the variability over replacement of the probe (chapter 7).

Chapter 5

Precision and accuracy limits of the BabyLux device

In the introduction of this thesis it was highlighted that one of the objectives of the BabyLux project was to improve the precision and accuracy of the state-of-the-art. This chapter is focused on exploring the limit in precision and accuracy of the BabyLux device. For this purpose, DCS and TRS data with added realistic noise have been simulated with the procedure explained in chapter 3. The role of different experimental parameters is investigated by generating data at different settings. Analogously, different choices for the analysis as well as different settings for input analysis parameters are implemented to individuate the role of each of them. Throughout the chapter, the results in terms of precision and accuracy described for each simulation and analysis setting are reported. To conclude with, experiments have been performed on phantoms and on a piglet model to verify the performance of the system on precision of results.

These results are reported in Giovannella, M., Spinelli, L., Pagliazzi, M., Contini, D., Greisen, G., Weigel, U. M., Torricelli A., Durduran, T. (2019). "The accuracy and precision of tissue optical properties and haemodynamic

parameters estimated by the BabyLux device: a hybrid time-resolved near-infrared and diffuse correlation spectroscopy neuro-monitor.", Biomedical Optics Express, *submitted*.

5.1 Curve simulation and analysis process

The procedure used for curve simulation and analysis was explained in chapter 3. Specifically, in figure 3.2 the process implemented for the generation of DCS and TRS curves with realistic noise was depicted.

Briefly, starting with TRS, the desired level of HHb and HbO_2 concentration are converted into μ_a for the wavelengths of interest. Once the μ_s' values are also chosen, the analytical solution of the photon diffusion equation (PDE) for semi-infinite homogeneous medium is convoluted with a typical instrument response function IRF(t). Afterwards the curve is adjusted to the desired count level and Poisson noise is added. This is done for all the wavelengths of interest. These curves are analyzed as explained in section 3.1.3, in particular using the fit analysis to retrieve optical properties from each generated curve. This is equivalent to reverse the process depicted in figure 3.2.

Analogously to TRS curves, diffusion approximation is exploited for DCS data generation. As depicted in figure 3.2, normalized electric field autocorrelation function is derived from the solution of the correlation diffusion equation (CDE). Realistic noise is added using the method and formula explained in section 3.2.2. Again, the reverse process is used for DCS data analysis, by fitting the simulated curve with the solution of the CDE.

It must be pointed out that using the same modeling for curve generation and analysis allows for understanding the lower limits for precision and accuracy due to photon noise and how this changes with different experimental and analysis settings. This procedure excludes the error due to the limits of the diffusion approximation.

5.1.1 Parameters for simulation and analysis

Experimental parameters

TRS		DCS	
λ	685 nm, 760 nm, 820 nm	λ	785 nm
ρ	15 mm	ρ	15 mm
Counts	10^5	Count rate	100 kHz
		Averaging time	1 s
		β	0.48

Tissue optical properties

λ	μ_a	μ_s'
685 nm	0.178 cm^{-1}	8.21 cm^{-1}
760 nm	0.175 cm^{-1}	6.86 cm^{-1}
785 nm	0.201 cm^{-1}	6.47 cm^{-1}
820 nm	0.175 cm^{-1}	5.96 cm^{-1}

Tissue haemodynamic parameters

Chromophore concentration	HbO_2	50 μM
	HHb	30 μM
	water	90 %
	StO_2	62 %
	BFI	10^{-8} cm^2/s

Table 5.1: Experimental parameters and tissue properties as defined for DCS and TRS curve simulation, unless differently specified.

In order to generate and analyze simulated data, various parameters must be defined in their values. Table 5.1 reports the default values for experimental and tissue properties used for data generation, if not differently stated. The experimental parameters were chosen accordingly to the BabyLux device (chapter 4). While the tissue properties are comparable to what measured in newborns with the BabyLux device (chapter 7).

Since the purpose of this chapter is to understand the contribution of each parameter in precision and accuracy of the retrieved values, I have simulated

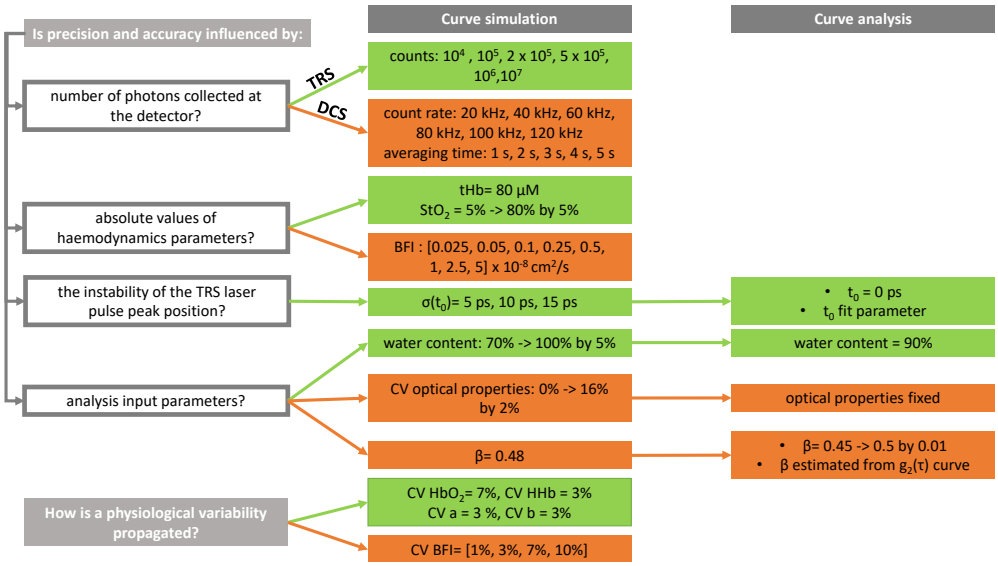

Figure 5.1: The left column lists the questions raised to characterize the influence of various parameters on the accuracy and the precision of optical and haemodynamic parameters. The central column explains how the settings for curve simulation were defined in order to answer those questions. Finally, the right column focuses on the settings for analysis input parameters.

different sets of data and varied the values of the parameters necessary for data simulation and analysis. Each sets of data consisted of thirty independent curves, generated keeping fixed all the parameters necessary for the simulation or assuming an *a priori* variability for some of them. This was defined by selecting a value for its coefficient of variation $\mathrm{CV} = \sigma_y/y$, where y is the mean value of an input parameter and σ_y is its standard deviation. Thirty values were randomly generated from a normal distribution centered at y and with a width of σ_y. Each of those thirty values was used for generating each of the thirty simulated curves.

In order to have some statistics in the variability and the error of the simulated data, this process was run ten times to generate ten sets of thirty

curves for each configuration.

Let me proceed by explaining how each set of data was generated. This is summarized in figure 5.1, that reports the values selected for each parameter either in the simulation (central column) or the analysis process (right column) in order to identify the contribution of each of them in precision and accuracy.

- **Parameters for TRS**
  To start with, DTOF curves were simulated changing the number of total collected photons from 10^4 photons to 10^7 photons. Afterwards, different absolute levels of StO_2 were considered, from a minimum of 5% to a maximum of 80%, with tHb concentration fixed at 80 μM. Then, an instability in TRS laser peak positions was simulated. TRS curves were shifted by t_0, generated from a normal distribution with a mean at 0 ps and a standard deviation (σ_{t_0}) of 5, 10 and 15 ps. In the analysis process, t_0 was either kept fixed or treated as a fitting parameters. Furthermore, an error in the water content estimation was introduced in the analysis. Data were simulated with a water content varying from 70% to 100% of the total chromophore concentration and analyzed considering it as 90% of the total chromophore concentration. Lastly, I have assumed a variability for HbO_2 concentration (7% of CV), HHb concentration (3% of CV) and for the Mie parameters a and b (3% of CV each) in the data simulation process.

- **Parameters for DCS**
  Figure 5.1 suggests how the same kind of effects were considered in DCS data simulation and analysis process as was done for TRS. As a first step, count rate was increased from 20 kHz to 120 kHz while the averaging time from 1 s to 5 s. In order to consider different BFI absolute values, this varied from $0.025\times10^{-8}cm^2/s$ to $5\times10^{-8}cm^2/s$. Afterwards, DCS data were simulated considering a variability for the optical properties (from 0.01% to 16% of CV). The same data were analyzed considering

the optical properties fixed at the mean of the thirty values used in the simulation. The other input analysis parameter is β, always considered fixed at 0.48 in the simulation, but either estimated from the $g_2(\tau)$ curve or varied from 0.45 to 0.5 in the analysis. Lastly, curves were generated with a BFI variability from 1% to 10% to check how the CV for BFI increased due to noise and analysis process.

5.2 Experimental measurements

All the measurements contained in this chapter have been performed with the BabyLux device, the hybrid DCS and TRS system described in chapter 4. In particular, the BabyLux probe was used, with a distance of 15 mm between the source and the detector fiber. This very same probe could be used on piglets because the extra-cerebral tissue thickness is comparable to the infant one.

5.2.1 Phantom measurement

Phantoms were measured to test the precision of the device over multiple continuous measurements for both TRS and DCS. A solid phantom made by epoxy resin as solid matrix, TiO_2 particles as scatterers and ink powder as absorber was measured by TRS. It was made with nominal optical properties of $\mu_a = 0.1$ cm^{-1} and $\mu_s' = 10$ cm^{-1} at 690 nm [176].

On the other hand, a liquid phantom, provided by HemoPhotonics S.L. (Castelldefels, Spain) [169], was employed for DCS, since this technique probes moving scatterers. The count rate for this measurement was 150 kHz.

Each set of phantom measurement, either solid or liquid, consisted of 30 curves.

5.2.2 Piglet model

The permit to perform the animal experimentation was obtained from the Danish animal experiments inspectorate (license no. 2016-15-0201-01021). Precautions were taken to reduce any animal suffering to a minimum. Anesthesia was induced shortly after arrival to our facility and sustained throughout preparation and experimentation until termination of the animal. Newborn piglets (Danish landrace) were delivered on the day of the experiment and rapidly anesthetized by intramuscular injection of Zoletil (xylazine 2 mg/kg, ketamine 10 mg/kg, methadone 1 mg/kg and butorphanol 1 mg/kg; Virbac, Denmark), intubated and put on a ventilator (Dameca, Denmark). Once the piglet was stable, the BabyLux probe was placed on the piglet head and 30 curves at 1 s time resolution were acquired. After the completion of the protocol of the main study, whose results are described in chapter 6, the piglets were euthanized with an overdose of intravenous pentobarbital 150mg/kg. Cerebral haemodynamics was continuously monitored with the BabyLux device during the euthanasia.

5.2.3 Analysis of experimental curves

Experimental curves were analyzed using the same flow explained for analysis of simulated curves (figure 3.2 from right to left). As explained in chapter 4 the shift of the TRS lasers was monitored independently from the TRS measurement. The measured shift was used to correct the position of the R^{exp}(t). Afterwards, in the fitting procedure only optical properties were used as fitting parameters, while t_0 was kept fixed at 0 ps.

As previously mentioned, different options are available for DCS input analysis parameters. The time average of the optical properties measured by TRS for each experimental set was used for DCS analysis. This means that they were kept constant over the whole set of measurements. An exception was made for the liquid phantom, where, in order to highlight the effect of the

variability of the estimates of the optical properties, they were inserted in the analysis by defining an *a priori* CV for them. The other input parameter for DCS analysis is β which was estimated from each experimental $g_2^{\exp}(\tau)$ curve.

5.3 Estimation of precision and accuracy

The precision over the 30 simulated or experimental curves was quantified considering either the standard deviation $\sigma(X)$, where $X = [x_1, x_2, ..., x_{30}]$ with x_i as each of the values obtained from the analysis, or as the coefficient of variation (CV). CV was defined as the ratio between the standard deviation and the mean value CV$= \sigma(X)/\langle X \rangle$. For the simulations, a relative error was also calculated to quantify the accuracy, defined as $\epsilon = (\langle X \rangle - x_{\text{true}})/x_{\text{true}}$, where x_{true} is the parameter value used for the simulation. As mentioned before, for the simulated curves, the generation of ten data sets of thirty curves for each setting allowed us to have a standard deviation of the variability ($\sigma(X)$ or CV) and of the relative error (ϵ).

5.4 Results and Discussion

Figure 5.2 shows example of DCS and TRS curves generated in the simulation process, both the model curve and the simulated ones with realistic noise are reported. Values used for simulating those data were the default ones reported in table 5.1.

5.4.1 Variability and error in simulated TRS curves

Figure 5.3 shows how CV of optical (a) and haemodynamic properties (b) decreases drastically with increasing total photon counts. Relative error decreases with increasing counts as well, but it is notably low (below 5%) for all the count levels considered. Increasing the count level from 10^5 photons, as used in the BabyLux device, to 10^6 would lead to a substantial improvement

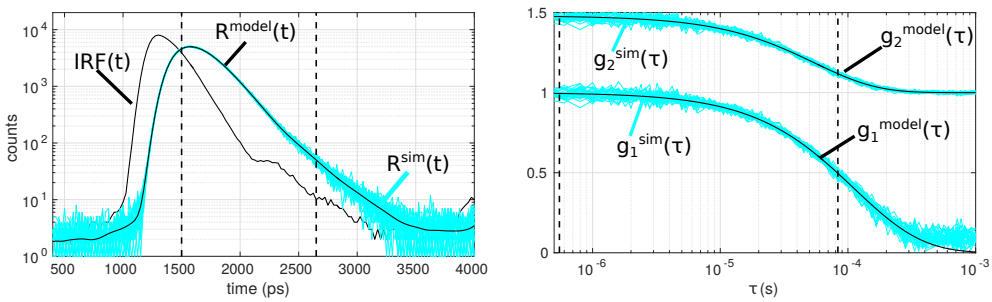

Figure 5.2: Right side, example of IRF(t), $R^{\mathrm{model}}(t)$ and of the thirty $R^{\mathrm{sim}}(t)$ generated at 760 nm. Left side, example of $g_2^{\mathrm{model}}(\tau)$ and $g_1^{\mathrm{model}}(\tau)$ and the thirty $g_2^{\mathrm{sim}}(\tau)$ and $g_1^{\mathrm{sim}}(\tau)$ generated in the simulation process. The dashed vertical lines highlight the fitting range.

in precision. This is crucial to improve the variability of current commercial cerebral oximeters, judged to be too high for clinical purpose [200].

The variability (CV) of StO_2 depends not only on the count level but also on its own absolute level. Specifically, CV and standard deviation decrease with increasing StO_2 level (figure 5.4). It was previously noted that accuracy in determination of optical properties by TRS depends on their absolute values [165, 202]. Better performance could be achieved with samples of high reduced scattering and low absorption coefficient. Those works simulated data with a method similar to the one used in this chapter, therefore their results did not depend on the limits of the diffusion approximation but on the shape of the collected curves. I have here shown that precision is dependent on the tissue properties as well. Nonetheless, it must be highlighted that the standard deviation of StO_2 does not vary as much as CV with the absolute StO_2 level. The high CV values at low StO_2 are mainly due to the fact that the denominator in the CV calculation is small.

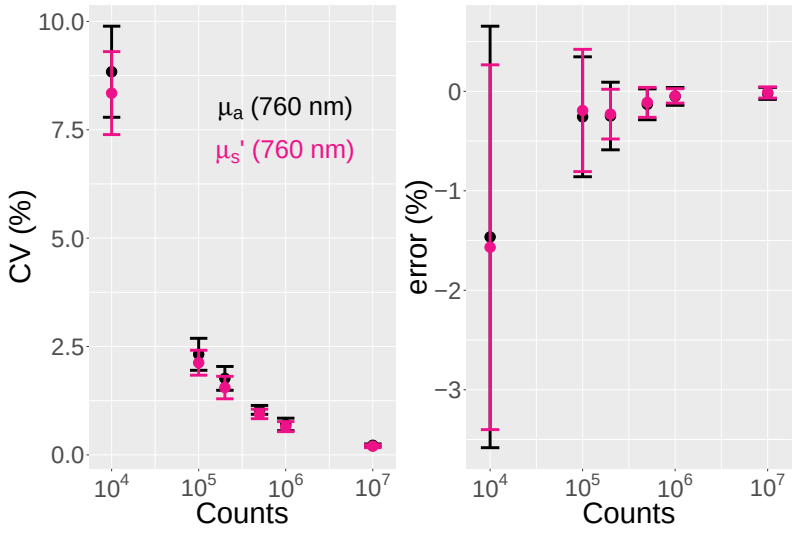

(a)

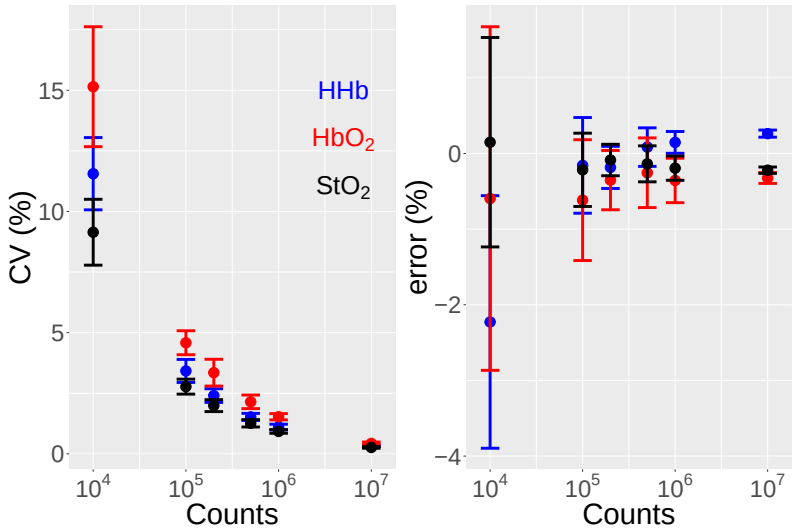

(b)

Figure 5.3: CV and relative error of the fitted absorption μ_a and reduced scattering coefficient μ_s' at 760 nm (a) and haemodynamics parameters (b) within thirty simulated curves at different counts levels. For optical properties, behavior of the other two wavelengths is equivalent. Error bars refer to the standard deviation over the ten sets of simulated data.

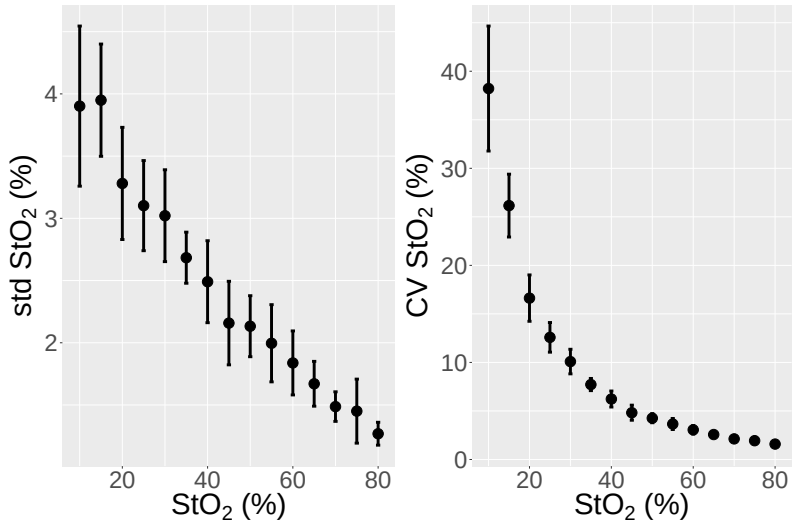

Figure 5.4: Standard deviation and CV of estimated StO_2 at different StO_2 levels within thirty simulated curves. Error bars refer to the standard deviation over the ten sets of simulated data.

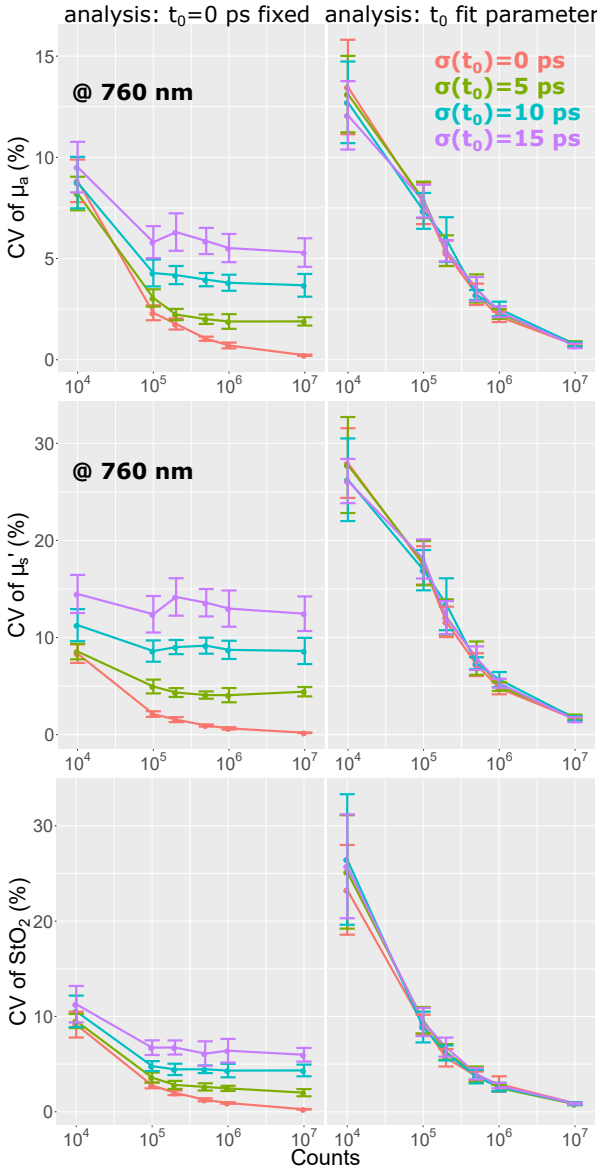

Figure 5.5: CV of absorption coefficient μ_a (top row) reduced scattering coefficient μ_s' (middle row) at 760 nm and oxygen saturation StO_2 (bottom row) at different counts level, when a variability in t_0 is considered in the TRS data simulation (standard deviation according to the legend). t_0 is either kept fixed in the analysis (left column) or treated as fit parameter (right column). Error bars refer to the standard deviation over the ten sets of simulated data.

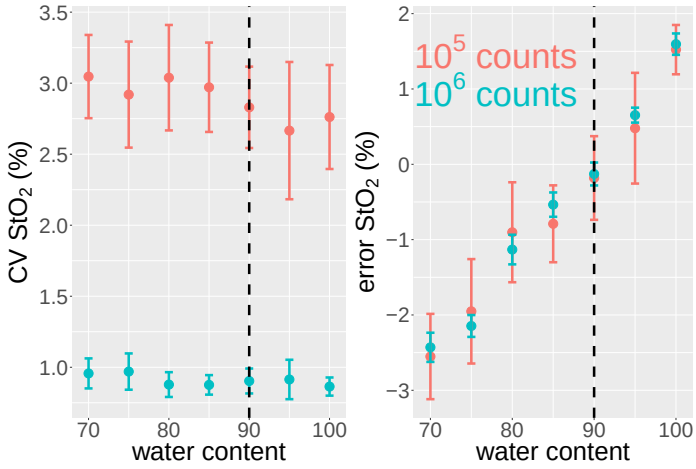

Figure 5.6: CV and relative error in oxygen saturation StO_2 when water content is either under- or over-estimated by the analysis (90%) compared to the value used for the simulation (according to the x axis). The dashed vertical black line indicates the only case where the true value is considered in the analysis. Results for only two count levels are shown. Error bars refer to the standard deviation over the ten sets of simulated data.

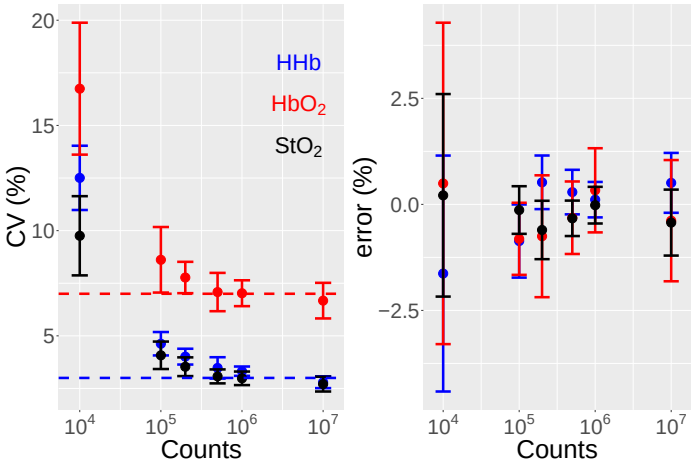

Figure 5.7: CV and relative error in haemodynamic parameters obtained by simulated data when an *a priori* physiological variability is considered, at different count levels. In particular a CV of 7% is assumed for HbO_2 concentration (red horizontal dashed line) and of 3% for HHb concentration (blue horizontal dashed line). Error bars refer to the standard deviation over the ten sets of simulated data.

Figure 5.5 summarizes how precision varies if considering the different available choices for t_0 determination in the fitting process, if an instability in the TRS peaks was simulated. The uncertainty in t_0 influences more drastically the μ_s' estimation than the μ_a, as expected. Two different behaviors arise increasing the count levels if two different approaches of the analysis are considered. If no correction for t_0 variability is considered (figure 5.5, left column) and if t_0 has a non zero standard deviation, CV of optical and haemodynamic properties is high even for high count levels. On the other hand, considering t_0 as a fitting parameter (figure 5.5, right column) leads to high CV for low counts level but provide a good correction and low CV for high count levels. In Ref. [165] it was demonstrated that an uncorrected shift of the peak of the spectrum resulted in large errors in the determination of the optical properties. For example, errors of 5% and 10% for μ_a and μ_s' were obtained with a shift of 20 ps. Such a large shifts were not considered in this simulation, since the Babylux device allows for monitoring the position of the TRS peaks concurrently to the measurement, as explained in chapter 4. The reference branch method works well for large and sudden change of the laser pulse but even the corrected peak position has a certain noise, that was simulated in this work. I have here shown that this kind of instability compromises the precision of results if no correction is applied, even at high count levels. Considering t_0 as a fitting parameter is a good method and gives good results only for high ($> 10^5$) count levels.

Water content is assumed fixed and estimated from literature values in TRS analysis for the BabyLux device, as done generally from TRS devices developed for neuro-monitoring. Figure 5.6 shows how StO_2 variability is stable if the water content is either over- or under-estimated, while the error in StO_2 increases.

Last simulation of TRS data focused on considering an *a priori* estimation of the physiological variability for haemodynamics. Figure 5.7 reports that at about 10^5 counts, the results for CV in the haemodynamic parameters already

match the input values.

5.4.2 Variability and error in simulated DCS curves

As expected, CV and relative error for BFI decrease increasing the averaging time and the count rate (figure 5.8). The improvement over the averaging time is not as drastic as shown for TRS, especially for high count rates. This is due to the fact that probability to detect pairs of photons within each bin time of the correlator does not increase linearly by increasing the averaging time [230].

Changing the absolute level of BFI leads to an increase in the standard deviation and a decrease in the CV at high BFI values (figure 5.9 for 100 kHz of count rate and 1 s of averaging time). This may be due to the higher noise registered in the (smaller) earlier delay times of the correlator [231], compared to the later ones, since DCS curves with higher BFI decay faster and are pushed towards the smaller delay times. This can be improved increasing the count rate and optimizing the correlator design.

The next point is about the effects of the input parameters in the DCS analysis, starting with the optical properties. They were considered as variable *a priori* in the data generation and figure 5.10 shows how CV of input μ_s' is drastically reflected in CV of the BFI, while the effect of a variability in μ_a is smaller. On the other hand the effect on the relative error is minimal. The drastic influence of μ_s' is explained by eqn. (2.14) that shows the coupling between BFI and ${\mu_s'}^2$ in the decay rate of the auto-correlation curve. Luckily, a change of μ_s' is not expected during haemodynamic changes. Since red blood cells account only for a tiny amount of the total scatterers, a change in their volume does not influence bulk scattering properties of the tissue. For this reason μ_s' is usually kept constant over measurements in DCS analysis. Moreover, the changes in μ_s' detected by TRS are often usually due to cross talk between μ_a and μ_s' in TRS analysis.

Proceeding with the input parameter for the analysis, the role of β was considered. If this is kept fixed, its under- or over-estimation did not compro-

mise CV of BFI while it did for the relative error of BFI (figure 5.11). On the other hand, estimating it from each curve lead to higher CV and relative error for low count rates, *i.e.* less than 50 kHz (table 5.2). We can conclude that for such low count rate is not convenient to estimate β from the first part of each single curve, since this is compromised by the noise. It is reasonable to keep β constant for an experiment as long as the laser source is known to be stable in coherence and that there is no significant leakage of external light.

To conclude with, a simulated *a priori* physiological variability for BFI was reflected in a comparable value in the CV of the estimated BFI at count rates larger than 50 kHz, while it was not reflected on the relative error, which depended only on the count rate (figure 5.12).

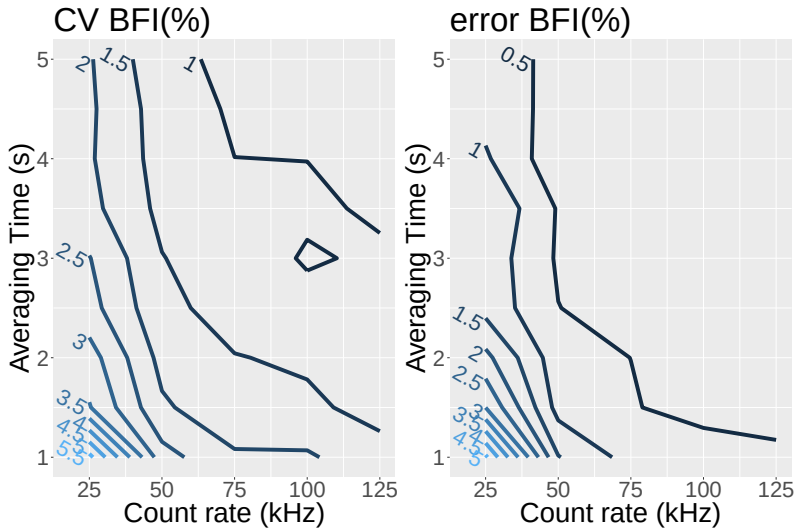

Figure 5.8: CV and relative error in BFI estimation from simulated curves at different count rate and averaging time.

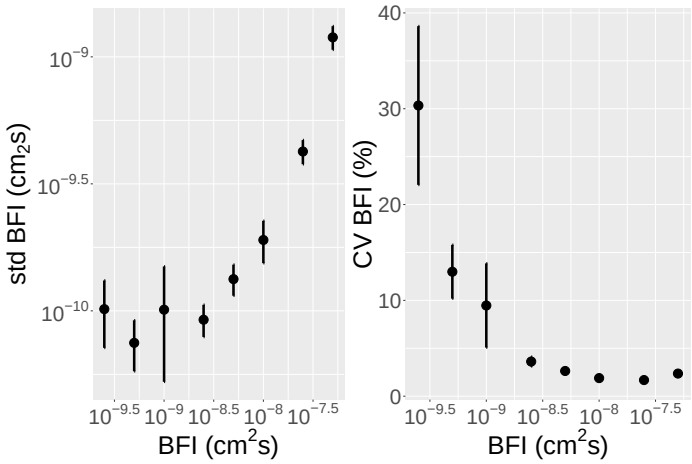

Figure 5.9: Standard deviation and CV of BFI estimation from simulated curves at different BFI levels. Error bars refer to the standard deviation over the ten sets of simulated data.

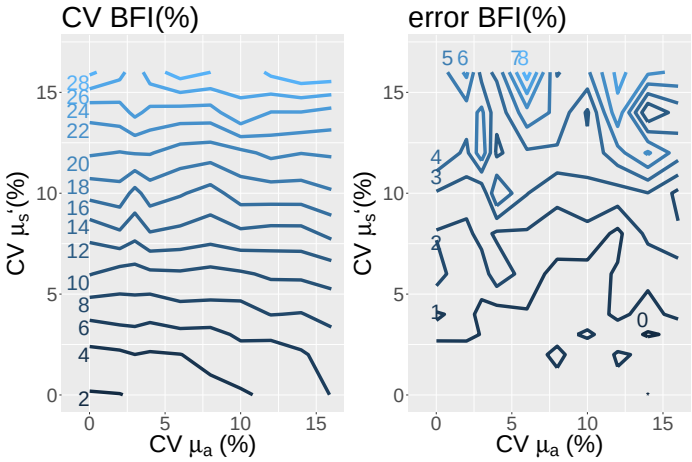

Figure 5.10: CV and relative error of BFI estimation from simulated data generated considering a certain CV for the optical properties in the data simulation, accordingly to the x and y axis. Count rate is 100 kHz and averaging time 1 s.

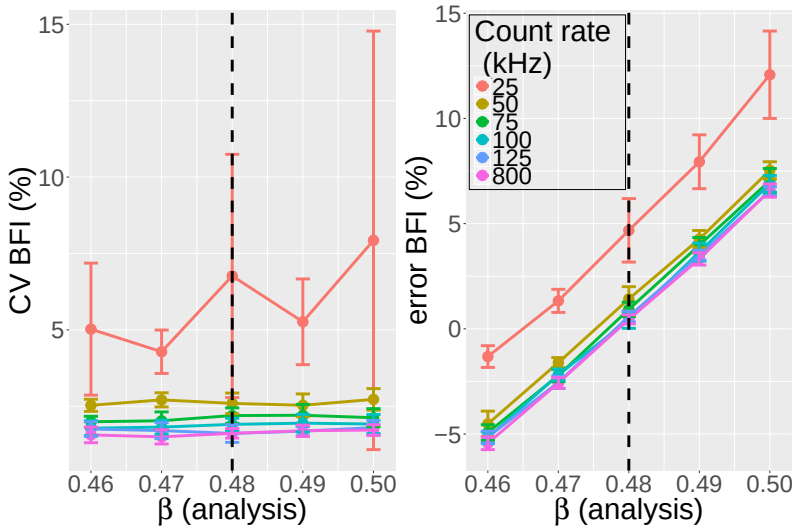

Figure 5.11: CV and relative error of BFI estimation from simulated data, at different count rate, when the value of β used for simulation (β=0.48) and the one used as input in the analysis (according to the x axis) do not coincide. The vertical dashed black line highlights the point when the two coincide. Error bars refer to the standard deviation over the ten sets of simulated data.

Count rate	CV BFI	error BFI
25 kHz	22% (5%)	3% (5%)
50 kHz	10% (2%)	0% (2%)
75 kHz	7% (1%)	-1% (1%)
100 kHz	5.4% (0.7%)	-1% (1%)
125 kHz	4.6% (0.6%)	-0.4% (0.7%)
800 kH	2.0% (0.2%)	-1.1% (0.3%)

Table 5.2: CV and relative error in BFI estimation from simulated data when β is estimated from each correlation curve, at different intensity levels. Standard deviation over the ten sets of data generation shown in brackets.

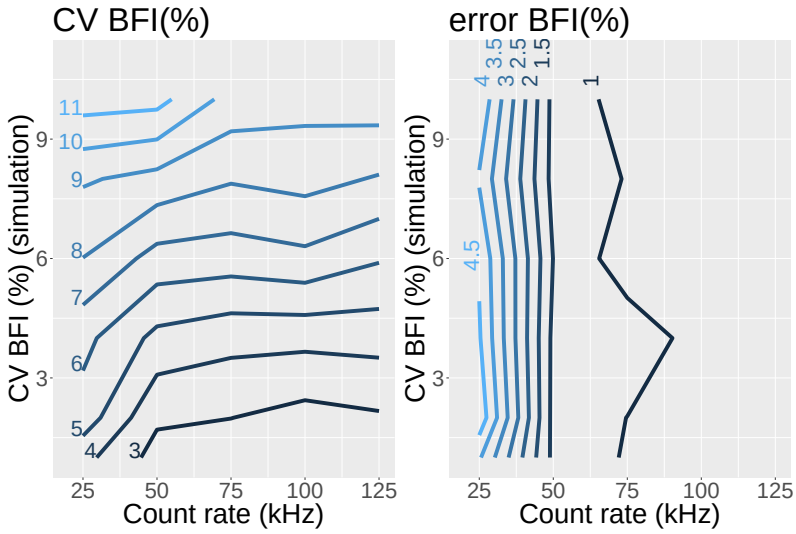

Figure 5.12: CV and relative error of BFI estimation from simulated data when a physiological variability is assumed for BFI, according to y axis, at different intensity levels, according to x axis.

5.4.3 Variability in experimental TRS and DCS curves

As described above, tissue simulating phantoms were measured by the BabyLux device to estimate the variability.

Thirty TRS measurements were acquired on a solid phantom at the three wavelengths at approximately 10^5 total photon counts to calculate its optical properties and their CV, shown in table 5.3. Results for the latter are comparable to those obtained from the simulated data. This is an indication of the good quality of the BabyLux device in terms of precision for optical properties. It must be noted that the solid phantom used for this measurement has different optical properties compared to the ones chosen for simulation (5.1). This phantom has been made specifically for the BabyLux device and it is kept in its drawer. It is measured every time the device is used and allows for monitoring the performance of the device during time. Therefore it is use-

ful to report performances on this phantom for future references. However, a phantom with optical properties closer to the values used for simulation can be considered. Among the solid phantoms used in the previous chapter, the one with μ_a(760 nm) of 0.19 cm^{-1} and μ_s'(760 nm) of 5.2 cm^{-1} has comparable CV over 30 s of continuous measurement as the one reported in table 5.3.

Analogously, thirty DCS measurements were acquired from a liquid phantom, with μ_a of 0.17 cm^{-1} and a μ_s' of 7 cm^{-1}, as measured by the TRS, with a count rate of 150 kHz. They were analyzed considering different levels of CV for input optical properties. The estimated BFI values are consistently increasing in variability with increasing variability of the input optical properties (table 5.4). Focusing on results considering no variability for optical properties, CV of DCS results from the liquid phantom is higher compared to the simulated data. The intrinsic variability of the liquid phantom can also influence this result.

In the experiments involving the piglet model, thirteen (N=13) piglets with a median weight of 3.25 kg (range 3.1 - 3.3 kg) and median age of 11 days (range 10 - 12 days) were measured. All TRS measurements were acquired at 10^5 counts in a approximately 1 s integration time. On the other hand, different count rates for DCS were collected from each piglet, since the output power for DCS light is constant. The median of the count rate was 150 kHz, with a minimum value of 100 kHz and a maximum value of 200 kHz. The optical and haemodynamic properties, and their CV, were retrieved and averaged over the sample population and reported in table 5.5 and table 5.6. Results for optical property and saturation variability are comparable to those obtained from simulated and phantom data, considering the absolute value of StO_2, lower than what was previously measured in infants [60] probably because the piglets were anesthetized. CV for BFI is slightly larger than in simulated data and comparable to phantom data.

The last experiment focused on registering the variability over a range of values changing dynamically in time by following changes after the euthanasia

of the piglets. This measurement was performed for eleven (N=11) piglets. In order to quantify the variability during these dynamic changes, ten second windows of measurements taken at one second resolution, *i.e.* ten data points, were selected instead of thirty as was done with the simulations. I have opted for this because choosing thirty second time windows with thirty data points would have resulted in a too variable of haemodynamics in each time window due to the rapid changes following euthanasia. The CV for BFI and StO_2 over ten seconds of measurement during the euthanasia decreased with increasing BFI and StO_2 absolute values (figure 5.13). Measurements over wide ranges of physiological values have to face this limit. This needs to be further explored and accurate confidence intervals must be established when reporting values in the ultimate clinical use.

λ	μ_a (cm^{-1})	CV μ_a	μ'_s(cm^{-1})	CV μ'_s
685 nm	0.070 (0.002)	2.3%	9.4 (0.2)	1.8%
760 nm	0.070 (0.001)	1.9%	7.7 (0.1)	1.6%
820 nm	0.066 (0.001)	1.7%	7.0 (0.1)	1.7%

Table 5.3: Optical properties estimation (with standard deviation in brackets) and their CV for thirty TRS measurements on solid phantom at the three wavelengths (λ) employed in the BabyLux device.

CV optical properties	BFI $\times 10^{-8}$ (cm^2/s)	CV BFI
0%	1.62 (0.08)	4.7%
3%	1.61 (0.09)	5.8%
7%	1.55 (0.15)	9.5%

Table 5.4: BFI, with standard deviation in brackets, and its CV as obtained from thirty DCS measurements on a liquid phantom. Different CV of optical properties are assumed in the analysis, as indicated by the first column.

Absorption coefficient		
	$\mu_a(\text{cm}^{-1})$	CV μ_a
685 nm	0.18 (0.15, 0.33)	2.3% (1.7%, 3.6%)
760 nm	0.16 (0.14, 0.31)	2.2% (1.6%, 3.6%)
820 nm	0.14 (0.12, 0.27)	2.1% (1.7%, 2.6%)
Reduced scattering coefficient		
	μ_s' (cm^{-1})	CV μ_s'
685 nm	10.3 (7.8, 11.9)	2.0% (1.6%, 3.4%)
760 nm	9.9 (7.4, 11.3)	2.1% (1.5%,3.6%)
820 nm	9.2 (6.9, 10.8)	1.8% (1.4%, 2.4%)

Table 5.5: Optical properties and their CV obtained from 30 s measurement at 1 s time resolution on a piglet head. N=13 piglets were measured, median (minimum, maximum) values over the population are reported.

Variable	Value	CV
HbO_2	25(18, 67) μM	7.3% (5.9%, 12.2%)
HHb	28 (23,50) μM	3.1% (2.4%, 5.9%)
StO_2	48% (37%, 60%)	5.3% (3.8%, 9.7%)
BFI	2.0 (0.7, 3.3) $\times 10^{-8}$ (cm^2/s)	4.5% (3.4%, 11.3%)

Table 5.6: Haemodynamic properties and their CV obtained from 30 s measurement at 1 s time resolution on a piglet head. N=13 piglets were measured, median (minimum, maximum) values over the population are reported.

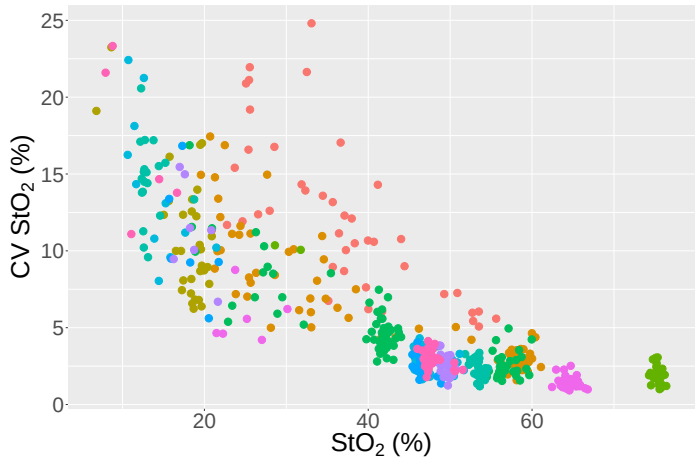

(a)

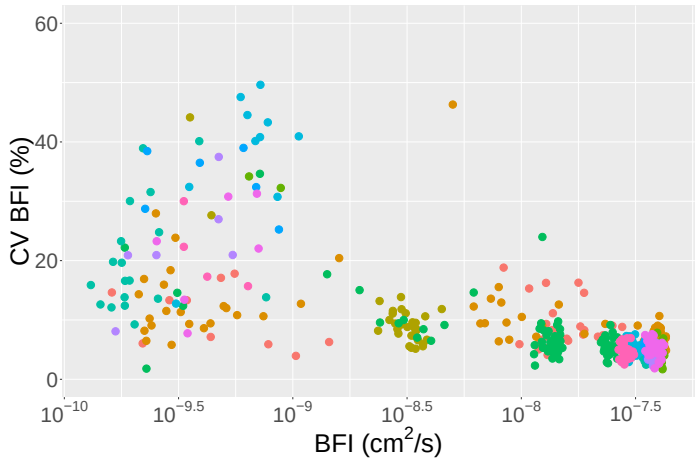

(b)

Figure 5.13: Variability of continuous DCS and TRS measurement on a piglet model during euthanasia. CV of StO_2 (a) and BFI (b) over 10 s measurement, at 1 s time resolution, is shown as a function of the mean absolute value in the 10 s bin. Color codes represent the different N=11 piglets.

5.5 Conclusion

Overall, these results define a lower value for CV and error for the BabyLux data, valid in the ideal scenario, considering the experimental parameters used for the real measurements (count rate, averaging time, temporal instabilities of TRS lasers, etc...). In addition, these results can be a guidance on how to choose parameters in the analysis process in order to maximize precision and accuracy. Surely, the picture here drawn is incomplete, since the error due to employing the diffusion approximation has not been considered. Nonetheless, this would minimally influence the precision of DCS and TRS measurements, while it would be more heavily reflected in accuracy. In spite of this, the conclusion on how to set the analysis process and how to select experimental parameters in order to obtain the best results are valid.

Good results were obtained for the precision of the optical property estimates from the phantom and piglet model which were equivalent to the simulation results. This proved good performance in terms of precision of optical properties of the BabyLux device. This was true also for the tissue oxygen saturation, while blood flow index variability in phantom and piglet resulted slightly higher than in simulations.

Chapter 6

Validation of CBF measurement by DCS with ^{15}O - water PET

This chapter is dedicated to the validation of cerebral blood flow measurement by the BabyLux device. As explained in Part 1 of this thesis, DCS assesses locally the microvascular blood flow in units of cm^2/s. This measurement is here validated on a piglet model towards the gold standard positron emission tomography (PET) using ^{15}O-labeled water as the tracer. I also provide a calibration formula to convert BFI measurement in flow units (ml/100g/min).

These results are reported in the manuscript Giovannella, M., Andresen, B., Andersen, J. B., El-Mahdaoui, S., Contini, D., Spinelli, L., Torricelli, A., Greisen, G., Durduran, T., Weigel, U. M., Law, I. (2019). "Validation of diffuse correlation spectroscopy against ^{15}O-water PET for regional cerebral blood flow measurement in neonatal piglets.", Journal of cerebral blood flow and metabolism, *submitted*.

6.1 Background

Positron emission tomography (PET) using ^{15}O-labeled water ($H_2^{15}O$) as a free diffusible tracer is the gold standard for measuring regional cerebral blood flow (rCBF) [87, 181]. This technology measures rCBF distribution with a time sampling of few minutes, since the tracer has a relatively short half-life (two minutes). Spacial resolution is limited to about 5 mm because of the high positron energy of the ^{15}O decay and the noise limitation. This technique is not a routine clinical modality, especially due to the short half-time of the tracer that requires it to be produced on-line and makes it costly. Only few centers around the world have it available.

Even when available, it cannot be extensively used on infants. One reason is that it requires patient transport out of the intensive care unit and stabilization for a prolonged period of time. Most importantly, it requires the patient to be exposed to a relatively high doses of ionizing radiation. Effort has been made to improve this and to develop methods to quantitatively measure rCBF by PET in neonates with a small injected $H_2^{15}O$ dose [6]. In spite of this, PET with ^{15}O-labeled water is still far to be used as a neuro-monitor in the clinical routine and most probably it will never be.

DCS, the technology implemented in the BabyLux device, offers an appealing opportunity to overcome the major drawbacks of ^{15}O - water PET listed above. As already explained along this thesis, it allows to continuously and at the cot-side monitor cerebral blood flow (CBF), being completely non-invasive and implemented in optical devices.

This chapter presents a study conducted on a piglet model that aims at validating DCS against the gold standard ^{15}O - water PET. rCBF was concurrently measured by DCS (the BabyLux device) and by ^{15}O - water PET during a protocol with acetazolamide injection and hypoxic challenges in order to explore a range of CBF values. I have investigated whether the BFI by DCS was correlated with rCBF and global CBF (gCBF) measured by ^{15}O -

water PET. In addition, I have calculated a conversion formula and its limit of agreement to turn BFI into flow units ml/100g/min. I have applied it to baseline haemodynamic measurements of another group of piglets, measured by the BabyLux device as well, and to measurements in infants (see chapter 7).

6.2 Methods

All animal procedures were approved by the Danish animal experiments inspectorate (license no. 2016-15-0201-01021). Precautions were taken to reduce any animal suffering to a minimum. Anesthesia was induced shortly after arrival to our facility and sustained throughout preparation and experimentation until the termination of the animal.

6.2.1 Animal model and preparation

Seventeen newborn piglets (Sus scrofa domesticus, Danish landrace) with a median weight of 3.2 kg (range 3.0 - 3.4 kg) and median age of 11 days (range 10 - 12 days) were included in this study. Two different protocols were applied. Group 1 involved six piglets, while the other eleven were included in Group 2. The animal preparation explained in this section is relevant for both groups, unless further specified.

The piglet was delivered on the day of the experiment and anesthetized by intramuscular injection of Zoletil (xylazine 2 mg/kg, ketamine 10 mg/kg, methadone 1 mg/kg and butorphanol 1 mg/kg; Virbac, Denmark), intubated and put on a ventilator (Dameca, Denmark).

During the protocol, electrocardiography was performed and pulse oximetry was measured continuously. In addition continuous monitors of rectal temperature (IntelliVue MP70, Philips, The Netherlands) and end-tidal carbon dioxide (Secma, Skævinge, Denmark) were established. Analgesia and anesthesia were sustained with intravenous fentanyl 10 μg/kg/h and propofol 20 mg/kg/h in

an ear vein using an infusion pump (B.Braun, Melsungen, Germany). Intravenous catheters were placed in the femoral arteries and veins bilaterally. An arteriovenous shunt was meant to continuously monitor the tracer activity in the blood (left femoral artery to left femoral vein). While the other was for monitoring arterial blood pressure (right femoral artery) and for fast administration of the tracer (right femoral vein). For Group 2 only the one relevant for arterial blood pressure was used. Additionally, an intravenous catheter was placed in the superior sagittal sinus through a craniotomy for cortical venous blood samples. All these monitors and measurements allowed for acquiring a complete picture on the physiology of the animal.

All catheters were flushed with heparinized saline every hour during preparation and subsequent stabilization. Intravenous antibiotics (ampicillin 200 mg/kg and gentamicin 4 mg/kg) were administered as sepsis prophylaxis, and, intravenous heparin (100 IE/kg; LEO Pharma, Ballerup, Denmark) to prevent blood clotting. A continuous infusion of isotonic glucose (15-20 ml/kg/h) compensated for fluid losses and maintained blood glucose levels.

6.2.2 PET measurements

The PET scans were performed on a high resolution research tomograph (HRRT, Siemens, Erlangen, Germany) with the piglet in prone position supported by a vacuum pillow. Only the head and neck were inserted in the scanner, which had 25 cm of axial field of view. First, a transmission scan using a Cesium-137 (^{137}Cs) point source was performed for attenuation correction. Afterwards, for each measurement, dynamic scans were started approximately 30 seconds before injecting a bolus of 100 MBq ^{15}O - water in the right femoral vein, which was subsequently flushed by heparinized saline. After the injection, data was collected for seven minutes in list mode. During this time, tracer activity in the blood was continuously measured every half second using the shunt between the left femoral artery and vein driven by a peristaltic pump (Allogg ABSS, Mariefred, Sweden) with a flow of 4 ml/min.

Transmission list mode data were histogrammed with emission contamination correction, and the transmission scan was reconstructed using the HRRT maximum a posteriori for transmission (MAP-TR) method [114]. The data were sorted as 1x25 seconds, 15x2 seconds, 11x5 seconds, 4x10 seconds, 9x30 seconds with a fast implementation [90] of the software OP-OSEM 3D (10 iterations, 16 subsets) including point spread function modeling [205], attenuation, random scatter and decay correction. The image size was 256 x 256 x 207 voxels with a 1.22 x 1.22 x 1.22 mm voxel size. Image frames were preprocessed using a 5 mm 3D Gaussian filter. A minimum time of 10 minutes (5 half-lives) between the scans was kept to allow for decay of the tracer.

PET image analysis

All quantitative PET image analyses were performed in PMOD v3.3 (PMOD Technologies, Zürich, Switzerland). Results from two volumes of interest (VOIs) were calculated. One contained the cortex of both hemispheres and I will refer at this result as regional CBF (rCBF). Then the global CBF (gCBF) was calculated by considering the whole brain. Time activity curves were generated for the VOI for kinetic modeling using a single tissue compartment model adapted for ^{15}O - water tracer studies by applying the equation

$$C_{PET}(t) = vBC_a(t)+(1-vB)\left(\tau k_1 C_a(t) + (1-\tau k_2)k_1 e^{-k_2 t}\int_0^t C_a(\tau)e^{-k_2\tau}d\tau\right) \tag{6.1}$$

where $C_{PET}(t)$ is brain tissue activity at the time t (count/s/ml), τ is dispersion of the tracer (s), k_1 is the unidirectional blood to brain clearance of the tracer (CBF; ml/min/100ml tissue), k_2 is the efflux rate constant (1/min), $C_a(t)$ is the arterial input function (counts/s/ml) and vB is the arterial blood volume fraction. Parameters k_1, k_2 and the tracer arrival time delay was fitted simultaneously by the Meyers method [152]. Dispersion was set to 3 seconds based on prior experience [5]. The arterial input function was derived from

the automated sampling from the femoral shunt. The measured activity was corrected for decay and was aligned with the start time of the scan. Only the first 3 minutes of the dynamic scan was used for kinetic modeling. rCBF and gCBF in ml/min/100ml as derived from the kinetic model was converted to the usual units of ml/100g/min by dividing for the brain tissue density 1.05 g/ml [125].

6.2.3 Optical measurement

The BabyLux device described in chapter 4 was used for the piglet measurement.

Data analysis

BabyLux measurement were analyzed off-line as explained in chapter 3. Some additional settings specifically chosen for these measurements will be here explained.

Specifically, baseline DTOF were fitted with both absorption (μ_a) and reduced scattering coefficient (μ_s') as fitting parameters in order to retrieve the baseline optical properties. Subsequently, the whole measurement was fitted fixing the μ_s' value at baseline and allowing for free shift of the temporary position of the IRF as previously explained [35]. Scattering properties are indeed expected not to change during haemodynamic changes and this improves the stability of the estimated μ_a. From the retrieved values of $\mu_a$at the three wavelengths, concentration of oxy- (HbO_2) and deoxy-haemoglobin (HHb) can be calculated. Water content was fixed at the 85% of the total chromophore concentration [89].

Few words must be spent on how the optical properties measured by TRS were used in DCS analysis. μ_a concurrently measured by TRS was used in the DCS analysis, while μ_s' was kept fixed during the protocol at the baseline value, as was done for TRS analysis. A second choice was made to define μ_s' to

be used in DCS analysis in order to reduce the effects of the variability of μ_s' on the DCS signal. First, a individual μ_s' for each piglet, as measured by TRS, was introduced in the DCS equation. Then a sample average of baseline μ_s' was calculated and DCS analysis was repeated using this value for all the piglets. This choice was reasonable since the piglets were of all the same breed, similar age and weight and were raised in a controlled manner.

6.2.4 Experimental protocol

After the preparation of the animal (described above), piglets of Group 1 were allowed to stabilize for at least 30 minutes before transport to the PET facility. Heating bags, blankets and manual ventilation were used to keep the animal stable for the duration of the transport.

Once in the PET facility, and after assuring that the piglet was still stable after transport, the BabyLux probe was placed over the left hemisphere of the piglet head using an auto-adherent bandage. 30 s of measurement was acquired and, subsequently, the bandage was released and the probe was placed again in approximately the same spot. An other measurement was run for 30 s and this was repeated until six sets of measurement were acquired. This protocol allowed us to define the variability within replacement of the probe. It was added on a later stage of measurement, therefore it was not available for all piglets. Afterwards, the probe was kept in place for the remaining protocol and acquisition run continuously. BabyLux device concurrently measured DCS and TRS with a sampling time of 1 s.

A series of ten PET scans were planned for each piglet, including three scans during baseline, three scans after a dose of acetazolamide (ACZ) and four scans during two levels of hypoxia. ACZ inhibits the carbonic anhydrase enzyme in red blood cells, which leads to an accumulation of carbon dioxide in the blood stream [130]. Since carbon dioxide is a potent vasodilator of cerebral arterioles and arteries, cerebral blood flow is increased [219]. Likewise, hypoxia is matched by an increase in cerebral blood flow to try to meet the

nutrient and oxygen demands of the metabolic processes [115, 216]. After the baseline scans 10 mg/kg acetazolamide (ACZ, Mercury Pharmaceuticals, Croydon, Great Britain) was administered intravenously and after 15-20 minutes to produce the increase in blood flow three new scans were acquired. Thereafter, hypoxia was induced by lowering the inspired oxygen and adding nitrogen trying to target a SpO_2 of 85% (Hypoxia A) for the next two scans and a SpO_2 of 50% (Hypoxia B) for the last two scans. Respiratory rate and tidal volume was adjusted to target an $EtCO_2$ near 5.5 kPa during baseline and below 8.5 kPa after ACZ injection. Upon completion of the protocol, or if humane endpoints were reached, piglets were euthanized by an overdose of Pentobarbital 150 mg/kg.

Piglets of Group 2 were not transported to the PET facility. After preparation and stabilization of the animal, the same replacement protocol of BabyLux probe was performed as in Group 1 above. It was again used for defining variability of DCS measurement but also for measuring baseline cerebral haemodynamics. A separate experimental protocol followed as the animals were being prepared for another study, but, since it was not object of the present study, it not reported in details.

6.2.5 Statistical data analysis

Statistical data analysis was performed through R [209] and threshold for significance for p-values was defined as 0.05. Firstly, I calculated the variability of BFI over replacements of the optical probe. For each of the six replacements BFI was averaged over the thirty seconds of continuous measurement. Variability was quantified as the coefficient of variation (CV) defined as the ratio of the standard deviation and the mean over the six replacements. As far as PET method is concerned, CV over the three baseline scans is calculated for its variability. Mean and standard deviation over the population of the CV for the two methods were considered.

In order to compare BFI obtained by DCS measurement with rCBF and

gCBF results from the PET scans, DCS measurement acquired in the three minutes after each ^{15}O - water injection was averaged and considered as corresponding to the concurrent scan. A visual check was performed for each scan to ensure that BFI did not vary considerably during the three minutes of averaging.

For each scans, a paired Wilcoxon signed rank text was performed to check whether the haemodynamic (BFI, rCBF and gCBF) and arterial blood gas parameters (partial pressure of carbon dioxide $PaCO_2$, of oxygen (PaO_2), saturation (SaO_2), haemoglobin concentration (Hb) and pH) changed respect to baseline in Group 1. Mean and standard deviation over the population of those parameters are reported.

The first hypothesis to be tested was whether BFI was correlated with rCBF and gCBF. For this purpose the Pearson correlation coefficient (R) was calculated. In order to estimate the slope and intercept between the two methods Deming regression was used [141]. This kind of regression is preferable when the reference method cannot be considered as without error. The sample average CV over the three baseline scans was computed and used as the error for PET and the sample average variability in replacement protocol was defined as the error for DCS. The Deming regression was performed with the R package mcr [145].

Subsequently, I have tested the hypothesis that the two methods were in agreement in rCBF measurement. Since they measure two different physical quantities, each of them with different units, I have converted the two into a unitless measure of rCBF (nrCBF) by diving each value calculated by one method by the average value of all the measurements performed by the method itself. First, a Bland-Altman plot was built by plotting the difference of the two methods versus the average. In case of heteroscedasticity, *i.e.* different variance for different values of nrCBF, a logarithmic transformation is performed.

In order to calculate the limits of agreement, the fact that measurements were repeated in each animal had to be taken into account through the pro-

cedure explained in [30]. In case of repeated (replicated) measurements, an error due to the interaction between animal and replicate, independent from the method, must be considered, together with the error due to the interaction between animal and method, independent from the replicate. Ultimately, a measurement variation is also due to the interaction between animal, method and replicate. To estimate the variance corresponding to these effects and their interaction, a linear mixed effect model was built and those errors are considered as random effects. The model gives the estimates of the variance for each random effect, which are squared summed for calculating the limits of agreement [30].

This method allowed for retrieving a conversion formula (and its limits of agreement) from BFI to rCBF to be used for single BFI measurements conversion. Therefore it was employed to convert each BFI measurements of the Group 2 piglets into flow units. A Wilcoxon signed rank text was used to check whether the measured rCBF in Group 1 was different from the BFI-derived rCBF in Group 2. This is different from comparing the BFI from the two groups because I convert individually each BFI from Group 2 instead of using a group conversion.

6.3 Results

Let me start with the optical property estimation for the piglets brain. The average μ_a and its standard deviation (SD) measured in the whole population of piglets (N=17) at 760 nm was 0.18(SD 0.06) cm^{-1} while μ_s' was 9.8(SD 0.8) cm^{-1}. I report results only for 760 nm since this is the closest wavelength to what used for DCS (785 nm).

A recording from one piglet of Group 1 is shown in figure 6.1 that also helps visualizing the protocol. BFI was measured by DCS with 1 s sampling time, concurrently ten PET scans were performed, with a minimum of 10 minutes between them.

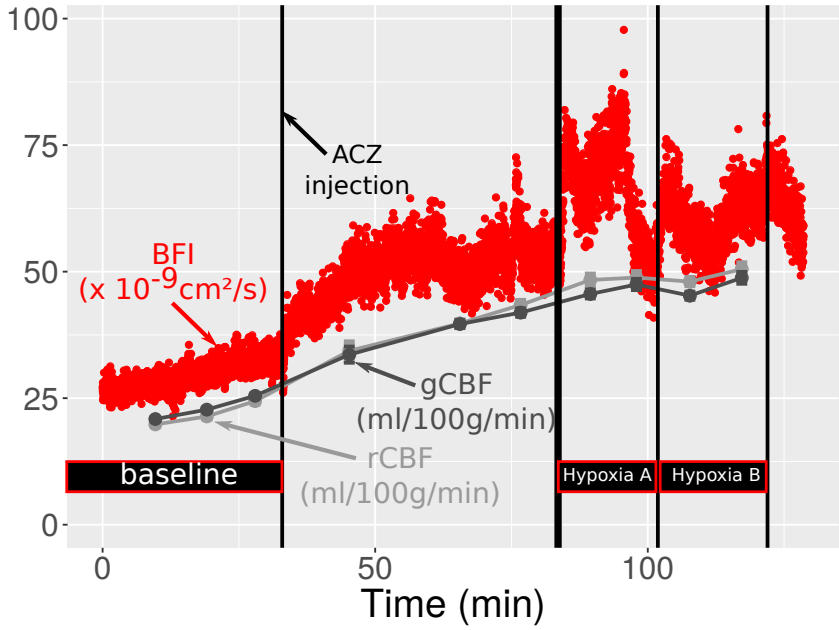

Figure 6.1: Example of the recording of rCBF and gCBF by PET and BFI by DCS during the whole protocol in a piglet of Group 1. Red dots represent the time series of BFI with 1 s time resolution. Light grey line shows rCBF values while dark grey line gCBF as measured by PET in each scan, synchronized with the DCS acquisition. After a period of baseline where three PET scans were performed, acetazolamide (ACZ) was injected, followed by three PET scans. Hypoxia was subsequently induced aiming at a SpO_2 level of 85% (Hypoxia A) and at a SpO_2 level of 50% (Hypoxia B).

An abrupt decrease of BFI was measured in this piglet at the end of Hypoxia A, as shown in figure 6.1. This happened simultaneously to a decrease in mean arterial pressure (not shown). This suggests a pressure-passive BFI, that might be due to the fact that, after ACZ injection and hypoxia, the cerebral artery system is already maximally dilated. PET measurement appears to be not equally sensitive because it happened in the last period of the about

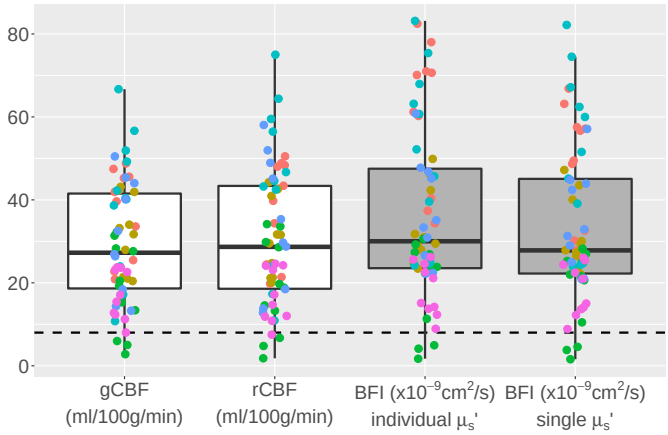

Figure 6.2: The white boxplots collects rCBF and gCBF measurements resulted from all the sixty-two PET scans performed in the six piglets. Grey boxplots refer to the BFI measurements by DCS corresponding to the PET scans by using an individual μ_s' for DCS analysis and a common μ_s' for all the piglets. Individual piglets are coded in different colors. The horizontal dashed line highlights the limit of 8 ml/100g/min.

three minutes of tracer activity, which weights less in PET signal. It must be noted that, in addition, DCS is sensitive to the extra-cerebral perfusion. This particular piglet showed an increase both in BFI and CBF at the beginning of the protocol, before ACZ injection. This may suggest that the piglet was not stable enough at the beginning of the protocol, even if, after the preparation of the animal, some time was considered to stabilize it. The measurements are still valid for our purpose, since BFI and CBF were measured concurrently.

Two of the six piglets of Group 1 had one additional scan (one after ACZ injection and the other during Hypoxia A). Therefore a total of 62 scans are available in Group 1 of piglets (figure 6.2). Some of those scans, corresponding to the hypoxic challenge, resulted in a very low rCBF value (<8 ml/100g/min). This was concurrent to a bradycardia (reduction in heart rate of 50% from

baseline) and to very low mean arterial pressure, below 20 mmHg. This value corresponds to a region where CBF is pressure-passive. This picture represents a pathological condition for the brain.

Baseline BFI values were available for both groups of piglets. Averaging over Group 1, baseline BFI resulted to be 25(SD 7)$\times 10^{-9}$ cm^2/s as mean (standard deviation) if an individual μ_s' was used for the analysis while 23(SD 5)$\times 10^{-9}$ cm^2/s if a common μ_s' was considered. On the other hand, for Group 2, it was 24(SD 7)$\times 10^{-9}$ cm^2/s and 24(SD 5)$\times 10^{-9}$ cm^2/s, if μ_s' was inserted in the analysis as individual or common value, respectively. Baseline PET measurements resulted in a rCBF of 18(SD 3) ml/100g/min and a gCBF of 18(SD 4) ml/100g/min as averaged in Group 1.

The variability over DCS and PET measurement was quantified in this protocol. For the former, a replacement protocol was applied to thirteen out of the seventeen piglets (four of Group 1 and nine of Group 2). It gave a coefficient of variation (CV) of 7% (SD 3%) as mean (standard deviation) of the thirteen piglets. On the other hand, CV over the three baseline PET scans resulted to be 18%(SD 12%) as averaged over the population for rCBF and 18%(SD 12%) for gCBF.

Blood gas and haemodynamic parameters were averaged in Group 1 over the different challenges (table 6.1 and 6.2, respectively). ACZ challenge provoked an increase in CBF and a small increase in $PaCO_2$, while PaO_2 and SaO_2 stay constant. The statistical test confirms a small decrease in pH after ACZ injection compared to baseline. Hypoxic state was demonstrated by the decrease in PaO_2 and of SaO_2. This did not provoke a concurrent change in rCBF and gCBF relative to baseline, if the whole piglet population was considered.

BFI and rCBF resulted to be highly correlated using both the DCS analysis configuration of μ_s' ($R>0.9$, $p<0.0001$) (figure 6.3). The Deming regression resulted in 1.34 (confidence interval (CI) 1.16, 1.55) (cm^2/s)/(ml/100g/min) and -4.43 (CI -9.79,-0.01) (cm^2/s) for slope and intercept respectively if DCS

Event	$PaCO_2$ (kPa)	PaO_2 (kPa)	SaO_2 (%)	Hb (mmol/l)	pH
Baseline	6.6 (0.9)	21.6 (3.5)	99.8 (0.9)	4.4 (1.5)	7.29 (0.08)
ACZ1	7.4 (0.7)	22.4 (2.6)	100.0 (0.3)	4.1 (1.2)	7.23 (0.06)*
ACZ2	7.7 (0.9)*	22.3 (2.5)	100.0 (0.2)	4.0 (1.1)	7.20 (0.06)*
ACZ3	8.0 (0.8)*	21.4 (2.5)	100.0 (0.3)	3.9 (1.1)	7.19 (0.06)*
Hypoxia1-A	8.3 (0.8)*	6.4 (1.8)*	61.6 (17.8)*	4.0 (1.1)	7.17 (0.06)*
Hypoxia2-A	8.3 (0.8)*	7.1 (1.2)*	68.3 (10.9)*	3.9 (1.0)	7.15 (0.08)*
Hypoxia3-B	8.3 (1.0)*	6.0 (1.5)*	53.2 (15.4)*	4.0 (1.0)	7.1 (0.1)*
Hypoxia4-B	8.5 (1.2)	5.7 (1.9)*	47.1 (18.2)*	4.1 (1.2)	7.1 (0.1)*

Table 6.1: Mean (standard deviation) of parameters estimated by blood gas analysis at baseline, after acetazolamide (ACZ) injection and during the two hypoxic challenges (Hypoxia A and B). Each event corresponds to a PET scan. Arterial partial pressure of carbon dioxide ($PaCO_2$) and of oxygen (PaO_2), arterial saturation (SaO_2), arterial haemoglobin concentration (Hb) and arterial pH are presented. * highlights statistically significant difference from baseline as confirmed by a paired Wilcoxon signed rank test ($p<0.05$)

analysis was performed with a individual μ_s' for each piglet, and, in 1.15 (CI 1.05, 1.27) (cm^2/s)/(ml/100g/min) and -1.54 (CI -4.88, 1.47) (cm^2/s) if DCS analysis was performed with a common μ_s' for all the piglets.

Interestingly, high correlation was also obtained between gCBF and BFI ($R>0.9$, $p<0.0001$) (figure 6.4). Linear regression by Deming method resulted in a slope of of 1.35 (CI 1.21, 1.45) (cm^2/s)/(ml/100g/min) and intercept of -5.08 (CI -8.64,-1.75) (cm^2/s), considering a common μ_s' in DCS analysis.

Apart for testing the correlation, I have also checked the agreement between the two using a untiless rCBF (nrCBF), calculated by dividing each value obtained by the two methods with the average of all the sixty-two measurements. This resulted to be 30 ml/100g/min for rCBF and 34×10^{-9} cm^2/s for BFI. In order to build the Bland-Altman plot (figure 6.5), a logarithmic transformation of nrCBF was performed to avoid heteroscedasticity. The variance component model estimated a bias of 0.004, practically zero,

Event	BFI individual μ_s' ($\times 10^{-9}$ cm^2/s)	BFI common μ_s' ($\times 10^{-9}$ cm^2/s)	rCBF (ml/100g/min)	gCBF (ml/100g/min)
Baseline	24.8 (7.1)	22.7 (5.1)	17.5 (4.4)	17.9 (4.5)
ACZ1	34.9 (14.2)*	31.9 (10.5)*	30.6 (9.1)*	29.8 (7.7)*
ACZ2	36.3 (14.1)*	33.4 (10.9)*	32.6 (8.0)*	31.5 (7.2)*
ACZ3	40.4 (17.4)*	37.0 (13.7)*	35.0 (8.5)*	33.4 (7.7)*
Hypoxia1-A	45.0 (25.5)	41.3 (21.5)	39.1 (16.6)	36.5 (14.0)
Hypoxia2-A	40.2 (24.2)	37.0 (21.1)	34.0 (17.7)	32.3 (15.9)
Hypoxia3-B	42.1 (27.9)	38.7 (25.2)	37.4 (22.9)	34.6 (20.4)
Hypoxia4-B	46.4 (34.5)	42.7 (31.7)	39.0 (28.9)	36.4 (25.4)

Table 6.2: Mean (standard deviation) of cerebral blood flow (CBF) at baseline, after acetazolamide (ACZ) injection and during the two hypoxic challenges (Hypoxia A and B). Each event corresponds to a PET scan. Blood flow index (BFI) measured by DCS and derived either using an individual μ_s' for each piglets and a common μ_s' is presented. Regional CBF (rCBF) and global CBF (gCBF) as obtained from the PET scans are also reported. * highlights statistically significant difference from baseline as confirmed by a paired Wilcoxon signed rank test ($p<0.05$)

considering the range in the y axis, as expected from the normalized measurement, with a standard deviation of 0.224, corresponding to (-0.445,0.452) as the limits of agreement. The bias in the logarithmic could be translated as $\text{nrCBF}_{PET}=1.004\times\text{nrCBF}_{DCS}$. By re-introducing the units for the two, a conversion factor can be calculated as rCBF=0.89 (ml/100g/min)/(cm^2/s)$\times 10^9\times$ BFI, with (0.56, 1.39) (ml/100g/min)/(cm^2/s) as the corresponding limits of agreement.

Baseline BFI measurement of Group 2 of piglets were converted to rCBF in flow units. No statistical significant difference was detected between the two groups by a Wilcoxon signed rank test (p=0.06).

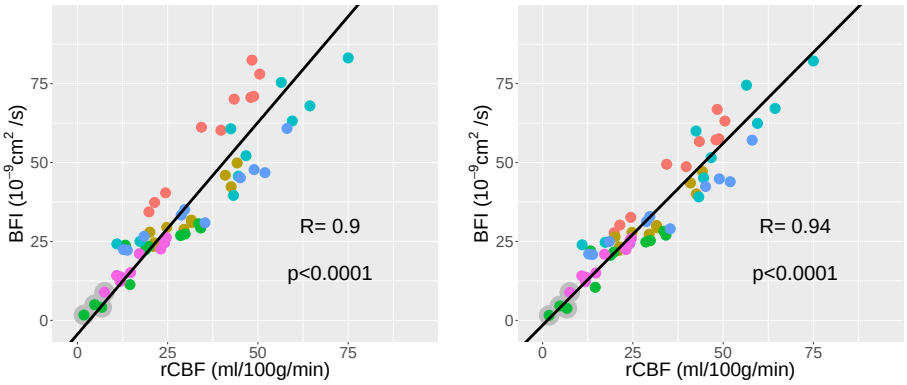

(a) individual μ_s' for each piglet (b) common μ_s' for population

Figure 6.3: BFI by DCS plotted against rCBF as measured by PET. Pearson coefficient (R) with its p-value is shown, while the line was obtained by the Deming regression. This has a slope and intercept of 1.34 (1.16,1.55) (cm^2/s)/(ml/100g/min) and -4.43 (-9.79,-0.01) (cm^2/s) respectively if DCS analysis was performed with a individual μ_s' for each piglet (a) and of 1.15 (1.05, 1.27) (cm^2/s)/(ml/100g/min) and -1.54 (-4.88, 1.47) (cm^2/s) if DCS analysis was performed with common μ_s' for all the piglets (b). Numbers in brackets represent the 95% confidence interval (CI). Colours code individual piglets (N=6). The grey circles highlight the scans which resulted in a rCBF<8 ml/100g/min

6.4 Discussion

This chapter presents the validation of DCS towards the gold standard ^{15}O - water PET for measurement of rCBF on piglets. Such an animal model is commonly used for the study of cerebrovascular pathophysiology in infants.

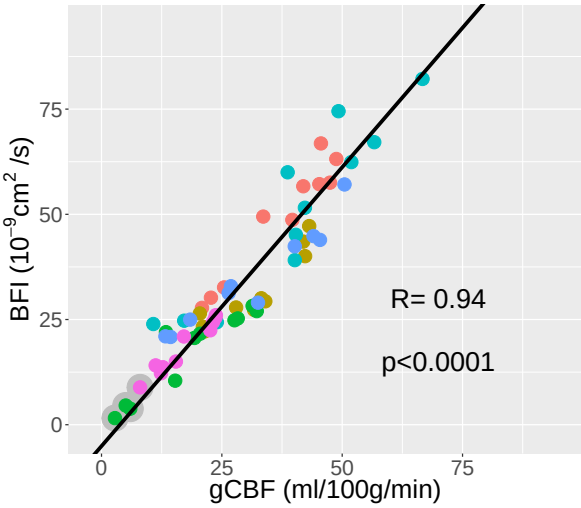

Figure 6.4: BFI by DCS (common μ_s' analysis) is plotted against global CBF (gCBF) as measured by PET. Pearson coefficient (R) with its p-value is shown, while the line was obtained by the Deming regression. This has a slope and intercept of 1.35 (1.21,1.45) (cm^2/s)/(ml/100g/min) and -5.08 (-8.64,-1.75) (cm^2/s) respectively. Numbers in brackets represent the 95% confidence interval (CI). Colours code the individual piglets (N=6). The grey circles highlight the scans which resulted in a rCBF<8 ml/100g/min.

6.4.1 Haemodynamic and blood gas parameters at baseline and during challenges

I will start comparing the CBF and BFI values found in our experiment with the literature. The same PET scanner was used in a previous study with older piglets (22 days instead of 11 days) [4]. They measured a higher baseline gCBF (median 26 ml/100g/min, in a range between 16 ml/100g/min and 38 ml/100g/min), but the divergence in age could explain the difference.

As far as BFI is concerned, values presented here were lower that what reported in another study using DCS on piglets [45,215]. Again, the comparison is not straightforward, since they used a different anaesthesia and CBF, hence

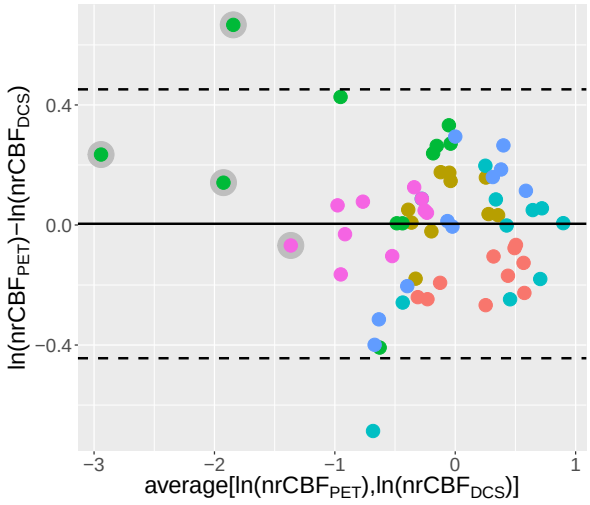

Figure 6.5: Bland-Altman plot for the logarithmic transformation of nrCBF. The calculated bias is 0.004 and is shown by the black thick line. The standard deviation estimated by the model is 0.224, which results in the limit of agreement highlighted by horizontal dashed lines (-0.445,0.452). The bias in the logarithmic could be translated as $\text{nrCBF}_{PET}=1.004\times\text{nrCBF}_{DCS}$. By re-introducing the units for the two, we have rCBF=0.89(0.56, 1.39) (ml/100g/min)/(cm^2/s)$\times 10^9\times$ BFI as the conversion factor and the corresponding limits of agreement in brackets. Colours code the individual piglets (N=6). The grey circles highlight the scans which resulted in a rCBF<8 ml/100g/min.

BFI, depends on the anesthesia [215].

Evolution of blood gas parameters and cerebral haemodynamics was followed throughout the protocol. In particular, ACZ injection caused an increase in $PaCO_2$ and CBF, as expected [219]. The hypoxic challenge was confirmed by the decrease of PaO_2 and SaO_2, however the expected CBF increase was not significant considering the whole group of piglets. This was due to a very diverse response among different piglets. Bradycardia was observed and mean arterial blood pressure decreased drastically in some of them and this caused a

decrease in CBF, suggesting compromised autoregulation capacity. Nonetheless, these measurements were still useful for the purpose of the study, since PET and DCS measurements were always acquired simultaneously.

6.4.2 μ_s' in DCS analysis

In chapter 5 of this thesis and in various pieces of literature [48, 100], it was reported how an accurate measurement of μ_s' is fundamental to assure accuracy in BFI estimation and how error and poor precision in μ_s' is propagated in BFI value.

For this reason, even when optical properties are measured concurrently, a population average of μ_s' is usually used in DCS analysis [60, 139], in order to not propagate in DCS the error of μ_s'. It must be noted that here the distribution of BFI values did not considerably differ if a common value of μ_s' was used compared to using an individual estimation of μ_s', except from one piglet. μ_s' estimated value in this piglet, encoded with red dots in figure 6.2, was the only one notably different from the average.

I have opted for presenting the complete results only using a common μ_s'. However, results would not have notably changed with the other analysis configuration, as demonstrated from the correlation results.

Chapter 7 discusses results related to the different choices for μ_s' in DCS analysis when measurements are performed on infants.

6.4.3 Correlation between BFI and rCBF or gCBF

Correlation between absolute BFI values and rCBF was strong ($R>0.9$) with high significance ($p<0.0001$) for both configurations of μ_s' evaluation. The correlation coefficient was slightly higher if using a common μ_s' for all piglets. In any case, the confidence intervals for slope and intercept estimated by the Deming regression overlapped in the two configurations. Notably, the confidence interval of the intercept did not contain zero in the individual μ_s' configuration

and this was not expected, given the proportionality between BFI and rCBF. One reason for this may be the increased, false, variability or a bias due to the μ_s' estimates.

It is of high interest that the BFI values highly correlated with the gCBF. It means that the local measurement of perfusion by DCS is, in this protocol, representative of the global CBF.

It has been highlighted that four PET scans resulted in a very low rCBF (<8 ml/100g/min) due to a low mean arterial pressure and heart rate. Those measurement were kept in the analysis and marked in the figures 6.3, 6.4, 6.5. The fact that the correlation between BFI and rCBF or gCBF holds even with these very low CBF measurements is a positive results. They surely emerge in the Bland-Altman plot (figure 6.5), due to the low mean. In spite of this, the difference between the methods is comparable to the range of all the other measurements for three of them.

6.4.4 Calibration formula

The bias in the Bland-Altman plot built with the logarithm of the normalized rCBF is practically zero (0.004), as expected from this normalization. For this reason the scaling factor is approximately the ratio of the normalization factors. Notably, it was comparable to the slope found with the Deming regression. Thanks to the method used, limits of agreement were defined for the scaling factor. Those are useful for conversion of single BFI measurements. The range defined by the limits of agreement was surely quite wide (approximately the 90% of the scaling factor) and this limits the reliability of this calibration for clinical purpose, for which it is necessary to have high confidence in a single absolute value. Another limitation is due to the fact that the whole cerebral cortex is used as the VOI to represent rCBF. It was not possible to consider a smaller volume, close to the BabyLux probe, because of high noise in small VOI that would have compromised the comparison between methods.

I have used the calibration formula to derive rCBF by single DCS mea-

surements on second group (Group 2) of piglets, with the same age and weight and prepared and monitored with the same protocol. Satisfactorily, converted rCBF in Group 2 is not statistically significantly different to rCBF of Group 1 by PET (p=0.06). They lied in a quite wide range due to the limits of agreement of the conversion formula. This procedure is not equivalent of comparing BFI from the two groups because the conversion formula is derived from all the measurements of Group 1 while rCBF in Group 2 is obtained by single BFI measurements.

Our formula can be compared with the few previous studies that investigated a calibration of the absolute BFI values in different population, such as piglets, infants and adults [45, 85, 106]. It must be noted that these works used different methods (phase contrast MRI and a combination of time-resolved dynamic contrast-enhanced near-infrared spectroscopy (DCE-NIRS) and DCS) and estimation of absolute CBF may not be consistent among them, thus the conversion formula may be dependent on the method.

The same piglet model was measured using DCE-NIRS, *i.e.* a flow tracer, and DCS. They report a slightly higher scaling factor (1.14 (ml/100g/min)/(cm^2/s)) than ours but still inside our limits of agreement [45]. This factor was confirmed by another recent calibration study employing the same method on adults [85]. On the other hand, the work measuring gCBF with phase contrast MRI on 4 days neonates with congenital heart disease reported a smaller factor of 0.4 (ml/100g/min)/(cm^2/s) [106]. This may be expected since it has been suggested that phase contrast MRI measures usually larger gCBF values then PET [180, 217].

6.5 Conclusion

The study presented in this chapter validated regional CBF measurement by DCS against the gold standard ^{15}O - water PET in piglets. DCS measurements were highly correlated with regional CBF and with global CBF. A conversion

formula for this population was derived for obtaining rCBF in flow units by single BFI measurement. The limits of agreement of the scaling factor are too wide for a clinical use that would require high confidence in each single CBF value.

Chapter 7

Clinical studies on infants

In the previous chapters I described the BabyLux device, explored its limits in precision and accuracy and reported validation measurements of CBF towards the gold standard positron emission tomography with ^{15}O - water PET as a tracer. After this, performance of the device in real clinical settings and on the target population can be explored. This chapter is dedicated to the clinical studies performed with the BabyLux device in two different neonatology units. First of all, cerebral haemodynamics in healthy term newborns was measured right after birth. In addition, a probe replacement protocol was implemented to assess measurement reproducibility. Results from the measurement of the transition at birth are reported in the manuscript: De Carli, A., Andresen, B., Giovannella, M., Durduran, T., Contini, D., Spinelli, L., Weigel, U. M., Passera, S., Pesenti, N., Mosca, F., Torricelli, A., Fumagalli, M., Greisen, G. (2019). "Cerebral oxygenation and blood flow in term infants during postnatal transition: the BabyLux project", ADC Fetal Neonatal Edition, *submitted*.

In the framework of the BabyLux project I was involved in the study design, data acquisition and data analysis and interpretation. I acknowledge Bjørn Andresen and Gorm Greisen for conducting the study in Copenhagen and Agnese de Carli and Monica Fumagalli for conducting the study in Milan, finalizing

the statistical data analysis and writing the manuscript for the delivery room protocol.

7.1 Background

The BabyLux project aimed at proposing a diffuse optical device that could be a neuro-monitor for the preterm infant. As explained in chapter 1, this was motivated by the current lack of a technology that can assess non-invasively and continuously the cerebral haemodynamics at the cot-side. The BabyLux device would allow to monitor the cerebral well-being of these infants that may suffer cerebrovascular lesions during the first hours and days of life [25, 138, 193]. Continuous monitoring at the cot-side of brain haemodynamics could help defining real-time clinical reference values to develop a brain-oriented clinical care for the preterm newborns [25].

As explained in the previous chapters, the BabyLux device was developed integrating time resolved near infrared spectroscopy (TRS), to measure blood oxygenation in the microvasculature of the tissue, and diffuse correlation spectroscopy (DCS), to measure microvascular cerebral blood flow (CBF). The device was tested in laboratory settings and the regional CBF measurement was validated towards gold standard positron emission tomography. Ultimately, two devices were built and translated into two different neonatology units, one in Rigshospitalet in Copenhagen, Denmark and the other in Fondazione IRCCS Ca Granda, Ospedale Maggiore Policlinico in Milan, Italy. Clinical studies involving healthy newborns were designed in order to test the device performance and feasibility in clinical settings.

To start with, we tested the performance of the device by measuring cerebral haemodynamics right after birth on healthy term newborns delivered by an uncomplicated elective cesarean section. First of all this was intended to assess whether the BabyLux device could measure in a complicated environment such as the delivery room and fast enough to catch the response in

the first minutes of life. BabyLux measurement of StO_2 were intended to be compared with previous works that employed commercial cerebral oximeters [3, 11, 62, 102, 172, 213, 214]. Moreover this study added information on CBF and cerebral metabolism, by measuring concurrently with DCS. These two parameters had not been measured before due to the lack of technologies to measure non-invasively CBF in the delivery room, right after birth.

The second study objective was to assess the variability of the BabyLux measurement over probe replacement. This is interesting because poor precision over different replacements of the probe is an issue in the commercial cerebral oximeters [78]. A replacement protocol on a healthy newborn head, during its first days of life, was implemented.

7.2 Methods

The study was conducted according to ISO 14155:2011 with external monitoring. Local research ethics committees approved the same study protocol in two centers (Rigshospitalet, Copenhagen, Denmark and Fondazione IRCCS Ca Granda, Ospedale Maggiore Policlinico, Milan, Italy). The protocol is registered at ClinicalTrials.gov, identifier NCT02815618. Written informed consent was obtained from parents or legal guardian prior to inclusion. The clinical investigation has been monitored by external consultants according to ISO 14155:2011 "Clinical investigation of medical devices for human subjects- Good clinical practice".

7.2.1 Measurement protocol

Infants with gestational age of at least 37 weeks were included in the study if planned to be delivered by an uncomplicated elective cesarean section. Exclusion criteria were congenital malformation apparent at birth, need for any additional assistance immediately following delivery and need for resuscitation or supplementary oxygen during the first 10 minutes after birth. Parental

consent was obtained before the elective cesarean section.

The protocol consisted of two phases, the first one took place immediately after birth and the other the following day. After birth the infant was wrapped in warm towels and the head and right hand or wrist were cleaned to remove vernix and amniotic fluid, to ensure good probe attachment. Afterwards the BabyLux probe was positioned in the fronto-parietal region, while a pulse oximetry was placed in the right hand or wrist, to measure peripheral saturation (SpO_2) and pulse rate. Both probes were held by a self-adherent bandage. The measurement were started as soon as the probe was in place and it lasted for at least 10 minutes, while standard neonatal care was provided.

The same infant was measured on the following day in a protocol aimed at assessing the repeatability of measurements. The probe was placed on the fronto-parietal region with the infant at rest, maintained by a self-adherent bandage, and 30 s of measurement acquired. Subsequently the bandage was lifted and the probe released and put back on approximately the same position. This was repeated until 6 sets of 30 s of measurement were acquired.

7.2.2 Data analysis

The BabyLux measurement were analyzed off-line, with the same procedure explained in chapter 3 optimizing parameters for the infant measurement. In particular, water content was assumed to be 90% [46]. DCS measurements from all the infants were analyzed with the same μ_s', averaged from the whole sample population.

Technical exclusion criteria were established for both DCS and TRS results. A threshold was defined for the count level of each DTOF curve (1000 counts) and for count rate registered by DCS detector during correlation curve acquisition (10 kHz). Once performed the fit analysis, the mean of the residuals for each data point were calculated and points where it exceeded 2 standard deviation from the mean of the whole measurement in the infants were excluded.

The continuous data acquired in the delivery room by the BabyLux device

were aligned with the pulse oximetry measurements. BFI and StO_2 were averaged in 10 s time windows as well as SpO_2 from pulse-oximetry. Tissue oxygen extraction was calculated as TOE=SpO_2-StO_2 and cerebral metabolic rate of oxygen extraction index as $CMRO_2I$=TOE $\times$ BFI.

Data from the replacement protocol were further cleaned. Specifically, the 30 s blocks with less than 50% of valid measurements were discarded. Only the infants with 6 valid repetitions for DCS and for TRS, independently, were further considered in the analysis.

7.2.3 Statistical data analysis

The relationship between each variable and time during the first 10 minutes of life was studied with linear mixed effect (LME) models, with time as fixed effect and subject as random effect. BFI and $CMRO_2I$ were previously log-transformed to adjust their right-skewed distribution. BFI and StO_2 values were extracted for each infant averaging data from 10 minutes after birth until completing the acquisition.

Data from replacement protocol were analyzed in order to define baseline optical and haemodynamics properties. Mean and standard deviation (SD) over the population were calculated, as well as median and I and III interquartile. From the same protocol, the coefficient of variation (CV) of BFI and StO_2 during 30 s of continuous measurement and within replacement of the probe was obtained. CV is defined as the ratio between the standard deviation and the mean value.

BFI and StO_2 measured in the delivery room after 10 minutes of life were compared with the baseline values measured during the replacement protocol by a paired Wilcoxon signed-rank test. Infants with successful measurement for both protocols were selected for this purpose.

7.3 Results

7.3.1 Study population

Thirty infants were enrolled. Four of them were excluded: one because needed resuscitation at birth, two due to parental consent withdrawn and the last one because of a software crash of the BabyLux device. Mean (SD) gestational age was 38.4 (0.7) weeks; mean (SD) birthweight was 3258g (393g); male were 13 (50%); median (range) Apgar 1' was 10 (8-10); median (range) Apgar 5' was 10 (9-10).

After validity check of data, the final number of accepted infants measurements from the delivery room protocol were 23 for SpO_2, 23 for StO_2 (TRS), 25 for BFI (DCS) and 20 for calculated TOE and CMRO2I. As far as the replacement protocol is concerned, the number of infants with six repetitions was 21 for StO_2 (TRS) and 20 for BFI (DCS).

7.3.2 Baseline values

Table 7.1 reports the baseline values for optical properties and haemodynamic parameters as measured in the first day of life during the replacement protocol. BFI and StO_2 measured after birth, right after transition, were calculated for each infant averaging measurements from minute 10 after birth until completing the protocol. These values were compared to the baseline measurement performed during the first day of life, considering only the infant with available measurements for both the protocols. DCS measurement from N=18 infants were therefore available, median (I-III inter-quartile) for BFI was 23 (19, 28)$\times 10^{-9}$cm^2/s as measured in the delivery room while 28 (23, 39)$\times 10^{-9}$cm^2/s as measured during the replacement protocol. No statistical difference is registered between the two days by a paired Wilcoxon sign-rank test. StO_2 measurements were available from N=19 infants. 65% (59%, 70%) is the median (I-III inter-quartile) measured in the delivery room, while 61% (57%, 66%) what measured in the replacement protocol on the following day.

Optical properties			
		mean (SD)	median(I, III interquartile)
μ_a (cm^{-1})	685 nm	0.18 (0.03)	0.183(0.166, 0.194)
	760 nm	0.19 (0.03)	0.194(0.170, 0.218)
N=21	820 nm	0.19 (0.04)	0.192(0.151, 0.209)
μ'_s (cm^{-1})	685 nm	8 (2)	8.52(7.54, 9.53)
	760 nm	7 (2)	7.01(5.54, 8.16)
N=21	820 nm	6 (2)	5.98(4.64, 6.78)
Haemodynamic properties			
HbO_2(μM)	N=21	47 (15)	47.7(32.8,57.9)
HHb (μM)		29 (4)	30.3(28.0, 32.4)
StO_2		60% (6%)	60.7 %(57.7%, 65.5%)
BFI ($\times 10^{-9} cm^2/s$)	N=20	31 (11)	28.8(23.1, 38.7)

Table 7.1: Baseline values for optical and haemodynamic properties in healthy term newborns as measured by the BabyLux device in the first day of life. Mean, standard deviation (SD), median and I and III inter-quartile range are reported.

No statistical difference between the two days is found.

7.3.3 Cerebral haemodynamics after birth

The average starting time for the measurement after birth was 3.5 min (standard deviation of 1.5 min). Only measurements from minute 3 were considered. Figure 7.1 reports measurements acquired from all the infants for StO_2, SpO_2, BFI, OE and CMRO2I. Black lines referred to the results of the LME model, a change over time was found to be significant for all the variables in the first ten minutes after birth. Specifically SpO_2 increased over time (estimate 3.05 %/min; CI: 2.78, 3.31 %/min; p<0.001) as well as StO_2 (estimate 3.95 %/min; CI: 3.63, 4.27 %/min; p<0.001), whereas BFI (estimate -2.84$\times 10^{-9} cm^2/s$/min; CI: -2.50$\times 10^{-9}$, -3.24$\times 10^{-9} cm^2/s$; p<0.001) and TOE (estimate -0.78%/min; CI: -1.12, -0.45 %/min; p<0.001) decreased. Analogously $CMRO_2I$ decreased (estimate -7.94 10-8/min; CI: -6.2610-8, -9.6210-8 /min; p<0.001).

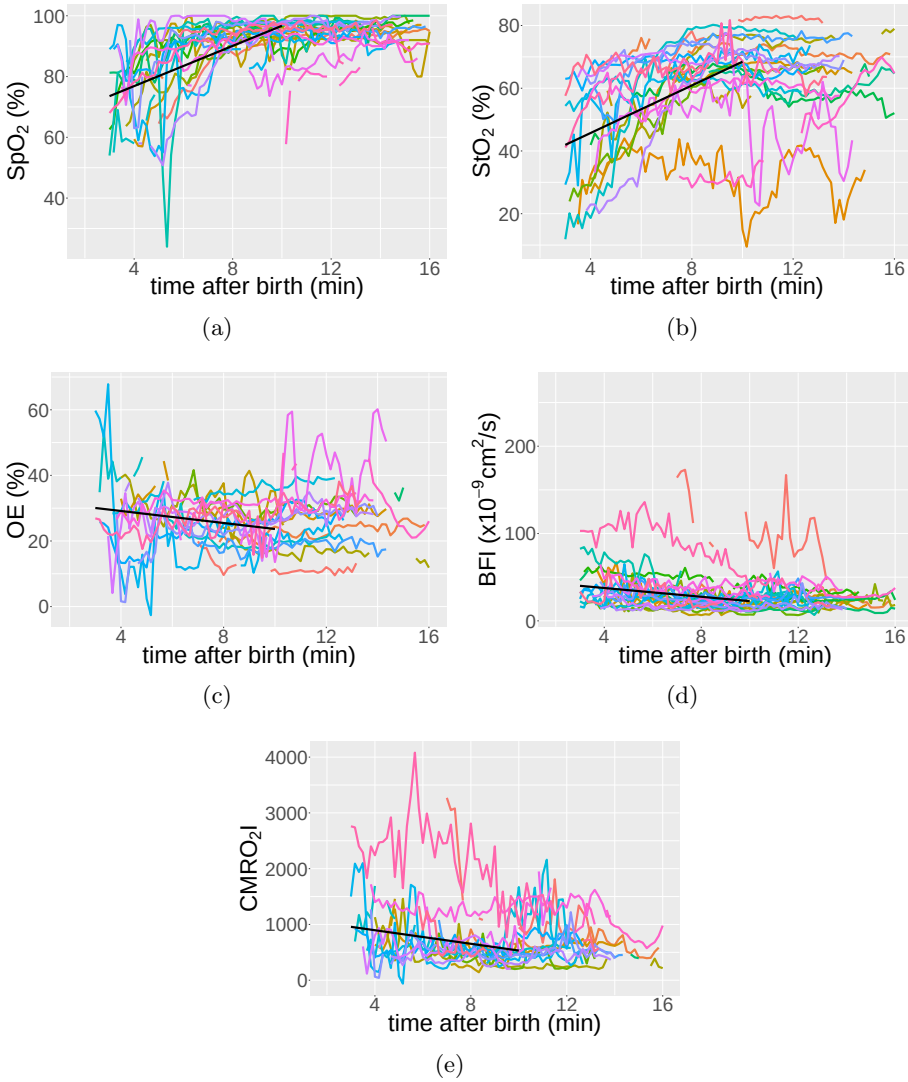

Figure 7.1: Peripheral arterial saturation (SpO_2) (a), tissue oxygen saturation (StO_2) (b), tissue oxygen extraction (TOE) (c), blood flow index (BFI) (d) and cerebral metabolic rate of oxygen extraction index ($CMRO_2I$) (e) in the minutes after birth measured in all the infants. Black lines indicate the results of the LME model.

7.3.4 Variability over replacement

Figure 7.2 shows the six measurements of StO_2 and BFI acquired on each infant included in the study. StO_2 results to have a mean CV of 4.3% within 30 s of continuous measurement and 5.2% over the six replacements. On the other hand BFI has a mean CV of 11% and 21,6% within 30 s of continuous measurement and over the six replacements, respectively (table 7.2).

Variability over 30 s			
StO_2	SD_{30s}	mean	2.4%
		median	2.2%(1.8%,3.0%)
	CV_{30s}	mean	4.3%
		median	3.6% (2.9%, 5.3%)
BFI	SD_{30s}	mean	3.4 ($\times 10^{-9}$cm^2/s)
		median	3.1 (2.1,4.1) ($\times 10^{-9}$cm^2/s)
	CV_{30s}	mean	11.0%
		median	9.5% (8.0%, 12.9%)
Variability over probe replacement			
StO_2	SD_{repl}	mean	3.0%
		median	2.6% (1.8%, 4.0%)
	CV_{repl}	mean	5.2%
		median	4.0% (2.8%, 7.2%)
BFI	SD_{repl}	mean	6.4 ($\times 10^{-9}$cm^2/s)
		median	5.6 (3.9, 8.4) ($\times 10^{-9}$cm^2/s)
	CV_{repl}	mean	21.6%
		median	21.5% (15.0%, 23.5%)

Table 7.2: Standard deviation (SD) and coefficient of variation (CV) over 30 s of continuous measurement and over six replacements of the probe for StO_2 and BFI. Mean and median (I, III interquartile) over the population are presented.

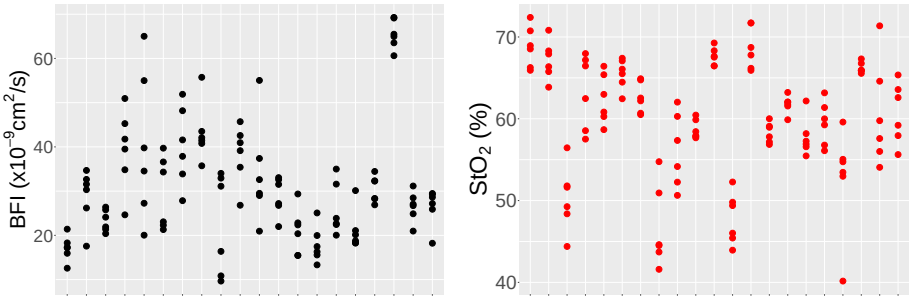

(a) (b)

Figure 7.2: BFI (a) and StO_2 (b) measurement over the six replacements of the probe for each infant.

7.4 Discussion

7.4.1 Baseline parameters

I reported baseline optical and haemodynamic properties as measured by the BabyLux device in 21 healthy newborns (20 for BFI). Values we found for optical properties are in the quite wide range reported in previous literature, considering both FD-NIRS and TRS [43, 60, 98, 203, 228].

Analogously, reported absolute values of StO_2 are not uniform within different studies and different devices. Our values are comparable to what measured by FD-NIRS on healthy infants [42, 60], but slightly lower than what measured previously with TRS [203] and much smaller than measurement with pediatric or neonatal sensor of commercial cerebral oximeters [12, 18]. It has been observed that cerebral oximetry devices with neonatal sensor display higher value than the adult device and in general measurement over different commercial sensors are not comparable [50, 122]. This considerable variability between instrumentations is an issue when a threshold for normal StO_2 values must be defined, as done in guidelines for ongoing clinical trials [96]. This must be im-

proved, on one side, working on standardization procedure and better protocols for assessing accuracy and precision. From the other side, more multi-center clinical studies enrolling a large number of infants should be run. Focusing on inter subject variability, our results are comparable to what measured with CW-NIRS [12, 18] and equal or lower with what measured with FD-NIRS or TRS [42, 60, 203].

BFI absolute measurements on infants have also been previously reported. An average BFI value (standard deviation) of 21 (8) $\times 10^{-9}$ cm^2/s has been recently measured in a group of 30 healthy term infants [60]. Nonetheless, a higher value (35 $\times 10^{-9}$ cm^2/s with a inter-subject coefficient of variation of 30%) has been measured in a control group of 13 healthy infants [40]. Our measurements lie between these two results. Variability among subjects is also comparable between our study and those previous works [40,60], being 35% the ratio between standard deviation and mean over the sample in our protocol. It must be noted that other standard technologies for blood flow measurement have a considerable inter-subject variability, but usually lower than what we found. For example, a recent PET study on four healthy newborns report a variability of 23% among infants, while a between-subject variability of 27% is associated to ^{133}Xe clearance method [10]. PET-measured CBF variability among subjects seems lower in adults, being around 15% [1, 86].

Few words must be spent on the fact that a common value for reduced scattering coefficient was used for all infants in DCS analysis. Chapter 6 reported that a slightly higher inter-animal variability was registered for BFI if an individual μ_s' for each piglet was considered in DCS analysis. Along these results, the BFI variability among infants increased drastically if an individual value of μ_s' was inserted in DCS analysis, reaching a value higher than 50%. The error in μ_s' is clearly being translated into an error in BFI, as explored in chapter 5 and in other pieces of literature [100]. For this reason we decided to consider a common μ_s' for all infants, as it is usually currently done for infant protocols [60, 139]. Surely, it is necessary to improve the accuracy of *in vivo*

μ_s' estimation for an accurate absolute estimation of BFI.

No statistical difference was detected between BFI and StO_2 measured in the delivery room and on the following day for the replacement protocol. Nonetheless, the tendency to increase for the former and to decrease for the latter is comparable to what previously observed in the first weeks of life [187].

To conclude discussion on baseline measurements, DCS measured CBF can be converted in flow units using the calibration formula found for piglets in chapter 6. Converting the sample average BFI results in a flow of 27 ml/100g/min, slightly higher than what is assumed to be the baseline CBF in healthy newborns (20 ml/100g/min) [77]. It must be reminded that very few studies have measured CBF in this population and generally a wide range of values is reported.

7.4.2 Cerebral haemodynamics after birth

The BabyLux device was used to study the cerebral haemodynamics during the first minutes of life, after an elective cesarean section, in healthy newborns. Measurement acquisition in this environment is quite complicated and the rate of valid measurement is a success, being comparable with the commercial pulse oximetry success rate.

After birth the circulation of the newborn changes from the fetal to the mature, extra-uterine one. After the first breaths the pulmonary vascular resistance drops, the circulation undergoes a transition from parallel to serial and the ductus arteriosus shunt started to close [162]. The peripheral arterial saturation is known to increase from around 60% to the usual 90% [38]. The increase we see in SpO_2 is comparable to the expected and previously measured behavior. Tissue oxygen saturation increases due to the increase in the arterial saturation. The StO_2 increase is comparable with what reported from previous studies [3, 11, 62, 102, 172, 213, 214]. It must be considered that all these works employed commercial cerebral oximeters, measuring higher values than ours as already noted. The measurement of both SpO_2 and StO_2 were

used to estimate the TOE, considering a compartmental model where arterial to venous fraction is constant [37]. Notably, this may not be true when a drastic change in saturation happens [225]. Nonetheless, most of the already cited works investigated oxygen extraction. They all measured FTOE = (SpO_2-StO_2)/SpO_2 instead of TOE and the two cannot be compared in values due to the high increase in SpO_2. In any case, all of them measured a decrease as in our measurement [3,11,172,214]. None of the previous work measured the CBF in the transition after birth and this is what our study adds. A decrease in CBF is measured from minute 3 to minute 10 of life. This decrease is in accordance with a measurement on sheep model with injected radionuclide-labeled microspheres [103]. In addition CBF velocity (CBFV) was found to decrease during transition after birth in humans, as measured in the middle cerebral artery from minute 5 of birth, with a resolution of about 5 minutes [163]. This is in accordance with our measurement even if they do not coincide temporally and CBFV is just a surrogate measurement of blood flow. This decreases in CBF can be motivated by a compensatory response to the increased oxygen content in the arterial compartment. It has also be related to changes in cardiac system. In particular the compensatory increase of the left ventricular output may be inadequate considering the increase of left to right shunt across the ductus arteriosus.

With the added information on blood flow, we could measure the metabolism. This is not expected to change especially after a cesarean section, which does not cause any stress to the baby. In particular, infants born by uncomplicated cesarean section have low levels of catecholamine, an indirect measure of the metabolic activity, compared to those vaginally delivered. Therefore they are not expected to be significantly stressed or asphyxiated and to have developed an oxygen "debt" during delivery [99, 134, 206]. In any case metabolism has never been measured before and the 50% decrease during the first ten minutes of life we found cannot be compared to other works. We can speculate that arousal occurring at birth could be associated with higher $CMRO_2I$ and

that we are measuring its descending curve. Our results therefore may suggest that even an uncomplicated cesarean section involves some physical stress and strain. It must be noted that, this calculation of $CMRO_2I$ can hide different source of errors, due to the variables that enter the formula. Furthermore errors may be oxygen content-dependent. The main weak point is calculation of oxygen extraction using all-optical measurements. This assumes a stable arterial to venous fraction components, which may not be valid in the drastic change in oxygenation we are measuring. Specifically, there are some evidences that this ratio is dependent on the saturation level itself [225]. $CMRO_2I$ calculation by all-optical measurements has been previously validated in piglets with good results [215]. Even if they explore a wide range of StO_2 by varying the anesthesia, SaO_2 is stable in their experiment, differently from ours.

7.4.3 Variability of BabyLux measurement

To start with, I will focus on the variability during 30 s of continuous measurements that can be directly compared to results on simulated, phantom and piglet data as reported in chapter 5. Remarkably, precision for StO_2 is perfectly comparable to simulation results at the same count level and StO_2 absolute value. On the other hand, 30 s precision for BFI in infants is higher than the simulation results. The range over the sampled infant population is quite narrow and is comparable to the largest values found for piglets. Different factors may have increase the variability of the BFI during continuous measurement in infants compared to piglets. Piglets were anesthetized, therefore, on one side, those measurements do not suffer from motion artifacts. On the other side, intrinsic variability is expected to be smaller during anesthesia.

The other aim of this clinical study was to investigate the variability over replacement of the BabyLux probe. This was motivated by the fact the standard deviation for StO_2 within probe replacement found with commercial oximeters was considered too high for clinical purpose [78]. Standard deviation over probe replacement for StO_2 was here 3% on average. This is lower than what

measured in commercial cerebral oximeters [88,95,200], a part from the FORE-SIGHT device. It must be noted that StO_2 as measured by the latter changed less than expected in the transition after birth [88], giving doubt on the validity of those measurements. In addition, it should be considered that we measured lower absolute value of StO_2. From the simulation results reported in chapter 5 it is clear that the CV and standard deviation are higher at lower StO_2 values. It has been demonstrated a much lower precision (less than 2%) if SpO_2 and continuous StO_2 measurement are concurrently registered and used to account for physiological and cerebral variation [123]. This was not implemented in the current protocol, which aimed at assessing the precision the clinical personnel could expect from a single StO_2 measurement of the BabyLux device. Even if considering this simpler protocol and analysis, our results improved the variability of StO_2 compared to the commercial cerebral oximeters. However, technological progress should still be focused on improving this result, in order to set a reliable threshold for normal values of StO_2 and act when different values are measured.

The reproducibility of BFI measurement over probe replacement (22%) is not easily comparable with other technologies as temporal resolution varies greatly, from seconds with optical methods to minutes with PET, due to differences in protocol for data acquisition and processing. In any case, test re-test variability with other modalities is not considerably lower than what we reported for DCS. Specifically, it was estimated to be from 8% to 27% with Xenon clearance method [80], while it is around 17% if NIRS technnology with injected tracer is used. It is reported to be lower with PET in adults (12%) [86], but in our piglets measurement it was actually 20% (chapter 6). In adults, variability over measurement is lower with ASL-MRI (5%) [86], but in infants it is expected to be higher with the same technology [220].

7.5 Conclusions

The BabyLux device could be translated in the clinics for small clinical studies and gave successful results. It could be employed to measure cerebral oxygenation after birth, in the complicated environment of the delivery room and with the necessity of starting rapidly the measurement to catch the rise in oxygenation. It proved its feasibility to be used in this protocol, without losing more measurement than the commercial and simpler pulse oximetry. The rise in tissue oxygenation was as expected and we added measurement on cerebral blood flow and metabolism. The decrease in CBF was not in contrast with previous findings, while the decrease in metabolism was not expected but could not be compared with any other measurement. Reproducibility over probe replacement of StO_2 was better than with commercial oximeter, while for BFI was comparable with other technologies which, however, do not measure perfusion continuously with such a temporal sampling.

Part III

Hybridization of a commercial DCS device and a prototype of a TRS device

Chapter 8

The integration of the two devices and test in laboratory settings

The third part of this thesis is focused on the development of an integrated diffuse optical device using a commercial DCS device and a prototype for a TRS device and on its application in a neuroscience study.

As a DCS device, the HemoFloMo (HemoPhotonics S.L, Spain) was available in our laboratory, while a prototype for a TRS device (TRS-20 by Hamamatsu Photonics K.K., Japan) was loaned to our group by Hamamatsu Photonics K.K., Japan. The prototype was modified into TRS-20I by the manufacturer for the purpose of the integration with the DCS. In this chapter the two devices are described, as well as the communication protocol between the two and the development of the integration. Results of laboratory tests are also presented.

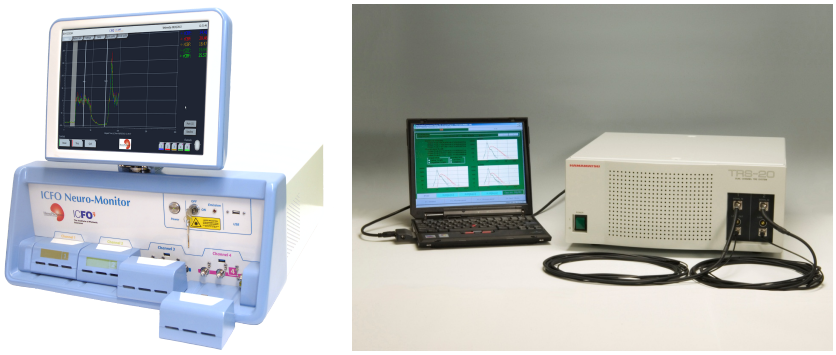

(a) (b))

Figure 8.1: Picture of HemoFloMo (HemoPhotonics S.L., Spain) (a) and TRS-20 (Hamamatsu Photonics K.K., Japan (b).

8.1 HemoFloMo

HemoFloMo (figure 8.1(a)) is a commercial DCS device developed and commercialized by HemoPhotonics S.L., Spain. It uses a CW long coherence length laser at 785 nm. Its light can be switched by an optical fiber switch within four source channels and an OFF position. In addition it has eight parallel detector channels. The user can select the configuration of the probe used and one or more detector channels can be associated to any of the source channels. There are no fibers included with the device, custom fibers from the user must be used. The device has four input and four output electrical channels, already integrated in the device. One of the output channels is dedicated to the marker signal, therefore each time a mark is selected in the device a signal is sent out from this channel. The others can be used by the user with a certain freedom, programming the measurement routine of the device.

8.2 TRS-20I

TRS-20 (figure 8.1(b)) is a prototype of a commercial TRS device by Hamamatsu Photonics K.K., Japan, based on the TRS-10 system that has been previously described [167].

It works with three laser sources at 760 nm, 800 nm and 830 nm. The repetition rate of the lasers is 5 MHz and the IRF has a width of about 300 ps. It has two source-detector channels. The system includes two complete sets of fibers for the two channels, either normal straight fibers or prism fibers. The latter allow for the fiber cable to run perpendicular to the direction of light injection and are particularly useful for measuring on the fore-head. Cases for IRF measurement are provided for both the fiber types

Signal	**Direction**	**Details**
Marker	IN	it marks an event in TRS-20I recording
Trigger	IN	it triggers TRS-20I measurement
Auto-Zero	IN	it defines the end of the baseline period
SW1	OUT	it switches the state of fiber switch 1
SW2	OUT	it switches the state of fiber switch 2
Done	OUT	voltage pulse after TRS-20I acquisition
Enable	OUT	high when TRS-20I is in acquisition mode
Busy	OUT	high when TRS-20I is acquiring data

Table 8.1: Input/Output channel for TRS-20I. Direction refers to whether each signal is an input or output channel and a short description for each signal is reported. Only the black font channels have been used in the integration protocol.

The TRS-20 has been modified to allow for communication with another device, I will refer to this modified device as TRS-20I. First of all, optical fiber switches with one input and two output positions (FSM 1x2, piezosystem jena, Germany) have been added. In this way the light could be deviated from the source and sent to an OFF position. In addition an external digital input

output board has been added. This is consist of a NI Compact- DAQ 4-slot USB Chassis (NI cDAQ-9174, National Instruments) and a two 4-Channel, LVTTL Digital Input/Output Module (NI 9402, National Instruments). Table 8.1 reports the input and output channels configured in the input/output board. Only the channels reported in black font have been used in the final integration protocol.

For completeness, I must conclude the section highlighting that TRS-20 has not been introduced to the market, but Hamamatsu Photonics K.K. has commercialized another TRS device called tNIRS-1 [69]. The pulse width of the source (1.5 ns) in this system is significantly larger than what is usually used in TRS devices (few hundreds of ps). Nonetheless, results for optical properties are comparable to what is measured by TRS-20 in phantoms and precision of the instrument is better than the CW-NIRS device commercialized by the same company (NIRO-200NX) [69].

8.3 Integration

In figure 8.2 a picture of the hybrid device composed by HemoFloMo and TRS-20I is shown. The integration was designed with HemoFloMo as the master. As explained above, HemoFloMo gives the freedom to the user to select a routine of events, which defines the behavior of input and output channels with respect to the DCS curve acquisition. When the start command is given, the routine will be executed and then iterated until the system is stopped. For the purpose of the communication with TRS-20I, the sequence of events in the DCS functioning has been set as:

- **DCSscan** (DCS acquisition)
- **TriggerON** (to set trigger output level to high)
- **wait100ms** (to define the length of the trigger signal for TRS)

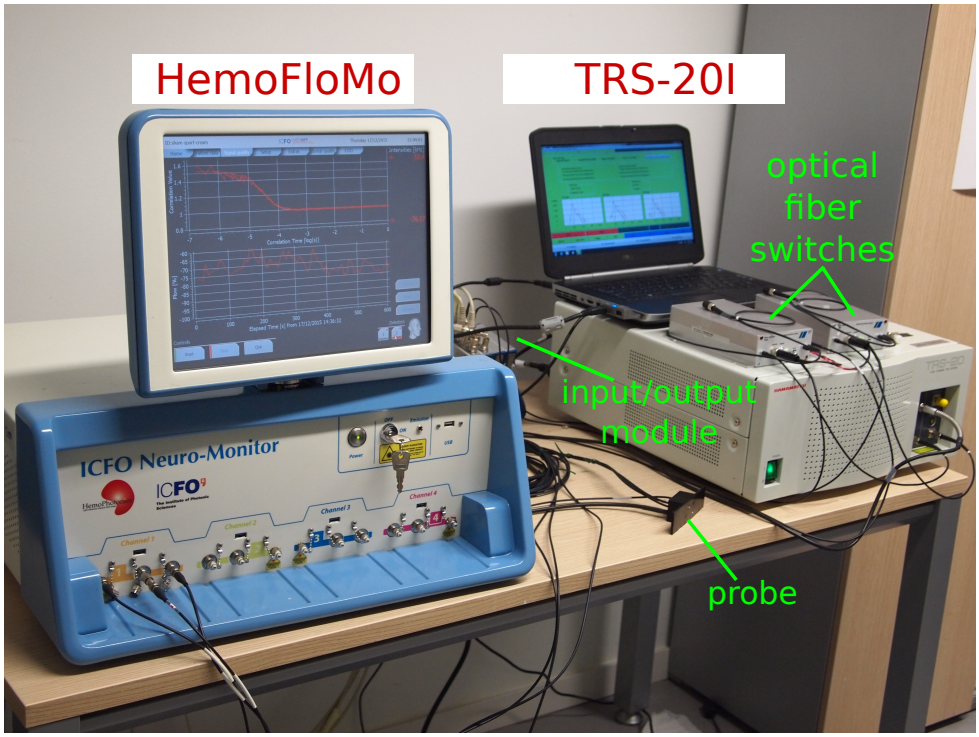

Figure 8.2: The hybrid device formed by TRS-20I and HemoFloMo is shown. Optical fiber switches and input/output module added to TRS-20 for the purpose of the integration are highlighted. The probe that encases fibers for both devices is also shown.

- **TriggerOff** (to set trigger output level to low)
- **waitTrigger** (to wait for a trigger input, "Done" signal of TRS-20I, before the next step)

Figure 8.3 reports a schematic view of the communication protocol between the two devices. First device to be started is the TRS-20I, the "Enable" signal is raised to high level and the device is waiting for a trigger to start the acquisition. Once HemoFloMo is also started, the procedure explained above

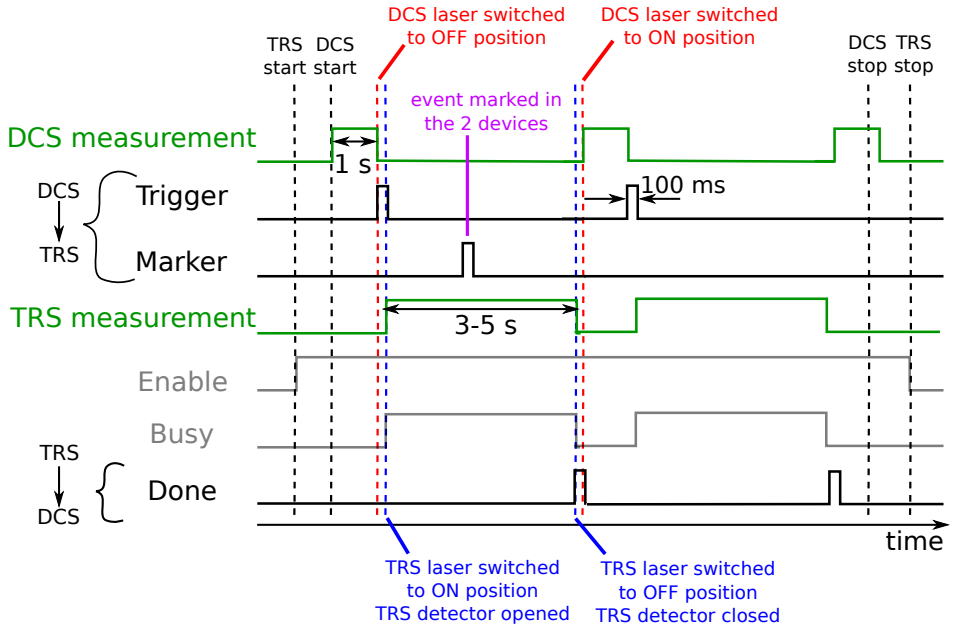

Figure 8.3: Communication protocol between HemoFloMo and TRS-20I. DCS acquisition is triggered by the signal "Done" from the TRS, while TRS acquisition by the signal "Trigger" from DCS. In each of the two devices, once a measurement is acquired, the light is switched from the ON position, corresponding to the probe, to an OFF, unused, position.

in the routine is followed. Therefore, a DCS acquisition is completed and, afterwards, a trigger pulse is sent to TRS-20I, through the channel "Trigger", and the HemoFloMo is in a waiting state until the next trigger. TRS-20I acquires one measurement and sends a trigger to HemoFloMo through the signal "Done". In order to avoid the two devices mutually disturbing the measurement, after each acquisition the optical fiber switches in the two devices turn the light from the probe into an OFF position. In addition, TRS-20I closes a shutter in front of its detectors after each measurement and opens them before each acquisition. This is because the high power HemoFloMo laser light would

cause saturation of TRS-20I detectors. On contrary, TRS-20I light is weak enough to not cause any damage to HemoFloMo detectors.

The acquisition time for the two devices can be set by the users, typical time sampling is reported in figure 8.3. DCS measurements can be usually acquired with 1 s of averaging time with HemoFloMo. On the other hand, longer integration time is needed for TRS-20I. According to the device manual, a ratio of at least three decades is suggested between noise level and the peak of the DTOF. This is usually achieved with 3-5 s of integration time.

When an event is marked in the HemoFloMo, a signal "Marker" is sent to TRS-20I and the mark registered in its own acquisition. This property is used for the synchronization of the two device acquisition.

8.3.1 Probes

Custom probes have been designed in order to host fibers of both devices. The source detector positions of the two devices must preferably lie in a cross configuration, in order to probe the same area with the two techniques. In figure 8.4 example of two probes designed in compliance with this condition is shown. In those examples two detector positions are foreseen for DCS. The cross configuration is valid for the long DCS source detector separation. The probe displayed on the left side of figure 8.4 is designed for TRS-20I prism fibers and for DCS bent fibers, therefore it would have fibers running parallel to the probe surface. While the one showed on the right side is used for straight fiber. The choice between the two probes depends on the application, the former is useful for measuring on the fore-head, while the latter one is preferable for phantom measurements or big muscles, e.g. the thigh.

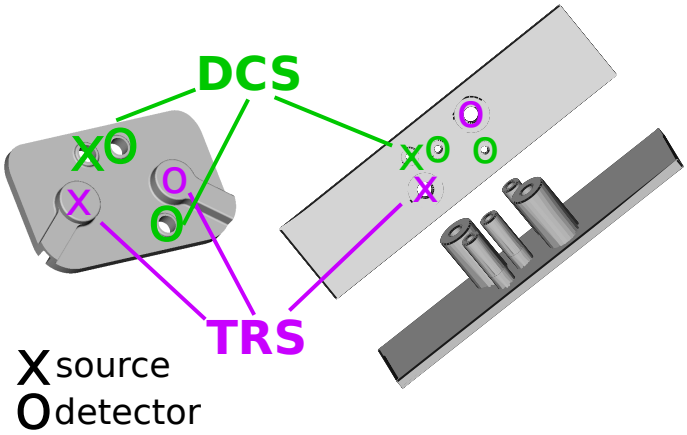

Figure 8.4: Examples of probes that can encase both HemoFloMo and TRS-20I fibers. The probe on the left side is designed for TRS-20I prism fibers and for DCS bent fibers, while the one on the right side (bottom and side view) can be used with TRS-20I and DCS straight fibers. Two detectors are used for DCS in these probes, one located at 25 mm from the source and the other one at 10 mm. Source-detector distance for TRS is 25 mm.

8.4 Tests in laboratory settings

8.4.1 Methods

Accuracy of optical property estimation by TRS-20I was tested by measuring six different solid phantoms (INO, Canada). The phantom manufacturer provides results of their optical property estimation by its own TRS system, claiming an accuracy of 20%. The solid phantoms were not measured at exactly the same wavelength by the manufacturer. Optical properties were specified by INO at 785 nm and 830 nm for all the phantoms, therefore the former was compared to the TRS-20I measurements at 760 nm, being the closest, and the latter one matches the corresponding TRS-20I measurements. Ten measurement were acquired for each phantom with an integration time of 5 s. Results

obtained from the ten acquisitions were averaged.

In order to test whether the communication between the two devices was working smoothly, an over-night measurement on a liquid phantom made with synthetic scatterers diluted in water and provided by HemoPhotonics S.L, Spain [169] was performed. Nominal optical properties were 0.1 cm^{-1} for μ_a(785 nm) and 10 cm^{-1} for μ'_s(785 nm), while nominal BFI amounts to 10^{-8} cm^2/s. Integration time was set to 5 s for TRS, while averaging time to 2 s for DCS. 5000 measurements were acquired representing the maximum number to be stored on TRS-20I. This measurement allowed to investigate:

- the communication signals between the two devices with an oscilloscope.
- the β parameter of DCS curve and the background counts measured by TRS. These quantities allowed to check whether light levels of the two devices mutually interfere in their measurements.
- the stability of optical and dynamic property estimation along several hours of measurement.

8.4.2 Results

Figure 8.5 reports the solid phantom optical properties measured by TRS-20I and compares them to what has been measured by the manufacturer, considering an accuracy of ±20%. All points measured by TRS-20I lie inside the accuracy ranges, it can be observed an over-estimation of the μ'_s, especially for lower μ'_s values.

The two signals "Trigger" and "Done" were monitored by an oscilloscope with the settings used for the over-night measurement on a liquid phantom. The monitored signals are reported in figure 8.6. The time between receiving the start trigger and sending the trigger after the measurement is larger than the sampling time chosen for the two devices. The difference is due to the actions performed by each device to prepare and to close the measurement

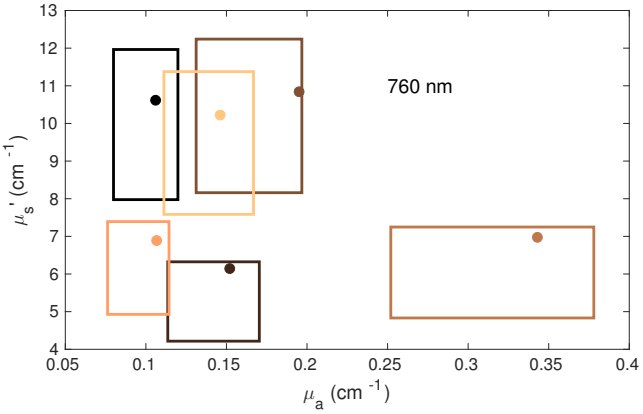

(a)

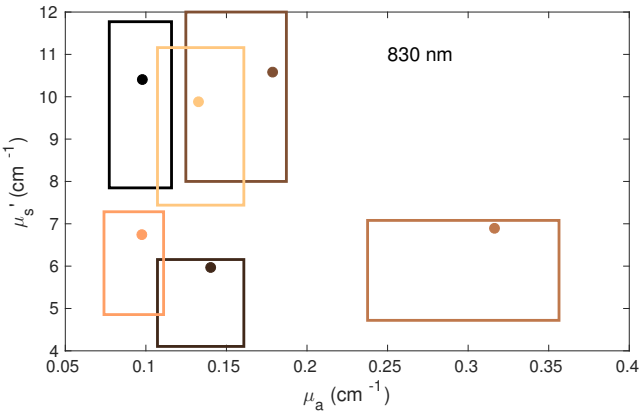

(b)

Figure 8.5: Optical properties of the six solid phantom (INO, Canada) measured by TRS-20I. Absorption coefficients are reported on the x-axis, while the scattering coefficients are indicated on the y-axis. The rectangles report the characterization performed by the manufacturer: the center is the value measured and the border the 20% accuracy.

before sending the trigger to the other (change of optical switches state and shutting of the detector for TRS). Over the 5000 measurements the average

time difference between two consecutive measurements is 9.1 s as registered by both devices, in accordance to what can be seen in figure 8.6.

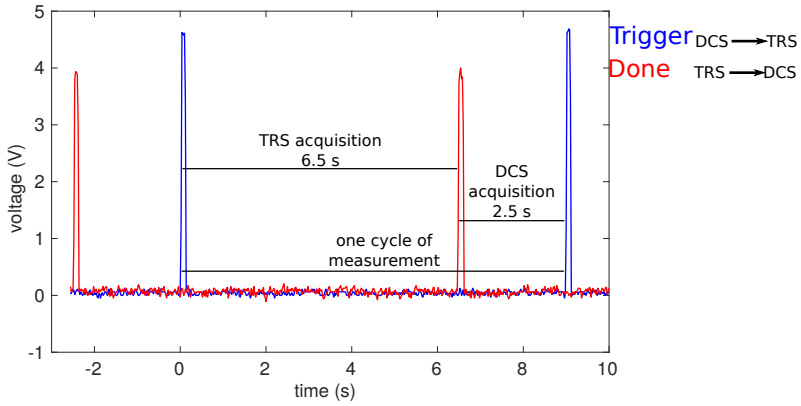

Figure 8.6: The two signals "Trigger" and "Done" measured by an oscilloscope, when TRS integration time is set to 5 s and DCS averaging time to 2 s. "Trigger" triggers the TRS-20I measurement while "Done" triggers the HemoFloMo measurement.

From the over-night measurement, β parameter of DCS curve and the background counts measured by TRS are the first parameters to be checked to assess the robustness of the integration. Spurious incoherent light would indeed lower the β parameter, while DCS light shining from the probe during TRS measurement would most probably saturate the TRS detector or at least increase the background noise. Figure 8.7 reports stability of these parameters over several hours of measurement therefore it assures stability of communication between the two. Optical and dynamic properties estimated by the hybrid TRS-20I and HemoFloMo are reported in figure 8.8. They appear stable over the 12 hours of measurement.

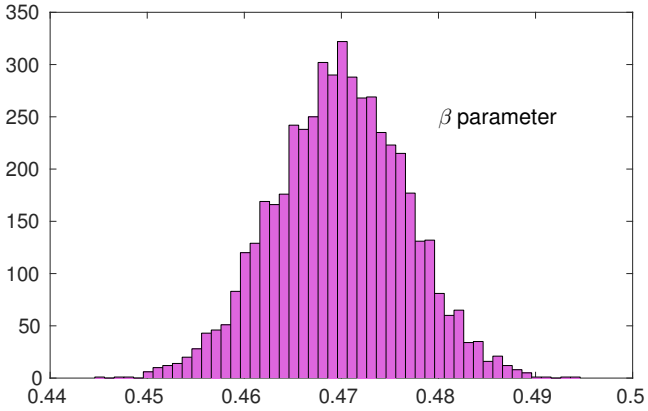

(a) β parameter, HemoFloMo

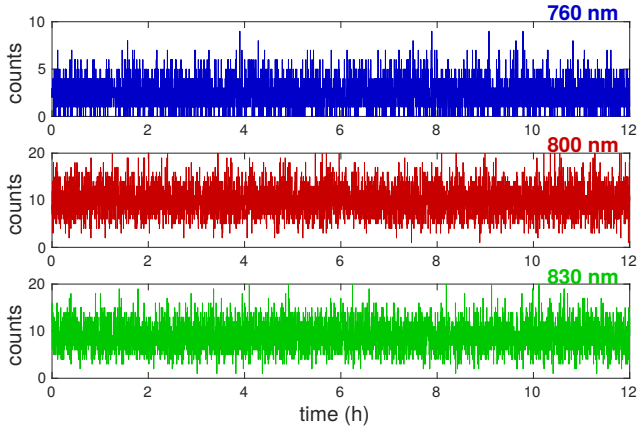

(b) Background counts, TRS-20I

Figure 8.7: Results from an over-night measurement on a liquid phantom. (a) histogram of β parameter measured from DCS curves acquired by HemoFloMo. Absence of low values assure that TRS light was not interfering with DCS measurement. (b) Background counts in TRS spectrum. The stability prove that DCS light did not interfere with TRS measurement and the communication between the two was stable over-night.

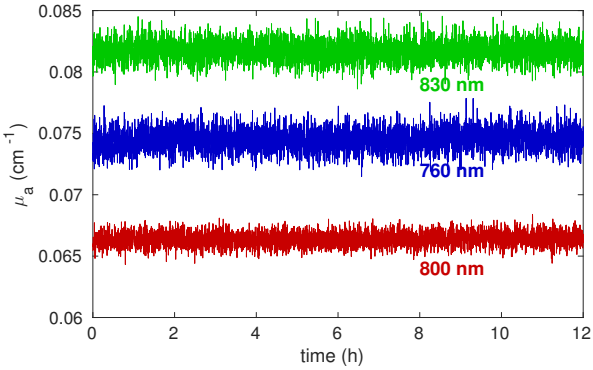

(a) Absorption coefficient

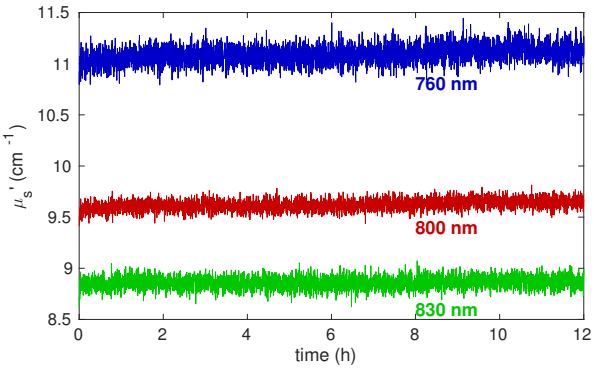

(b) Reduced scattering coefficient

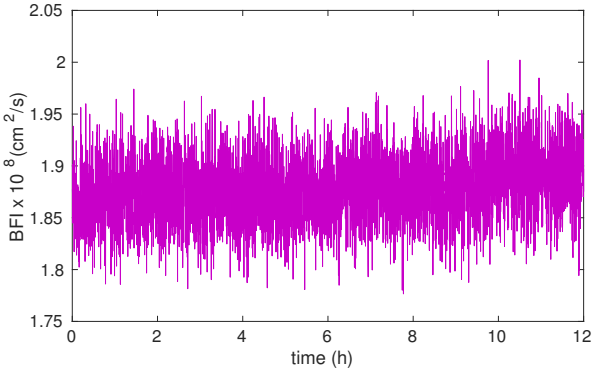

(c) Dynamic properties

Figure 8.8: (a) Absorption, (b) reduced scattering coefficients (at three wavelengths) and (c) BFI of a liquid phantom by the hybrid TRS-20I and HemoFloMo.

Chapter 9

Cerebral haemodynamics and electroencephalography measurements during transcranial direct current stimulation

In this chapter I present a study performed with the hybrid TRS-20I and HemoFloMo device, described in the previous one. The device was used to monitor cerebral haemodynamics during transcranial direct current stimulation and, concurrently, electroencephalography was also measured. The aim is to explore the possibility to use diffuse optical cerebral haemodynamic monitors to gain online feedback of the stimulation, in order to improve and optimize protocols of intervention. EEG is the technology commonly used for monitoring the effect of the stimulation and the study purposes included demonstration that we could concurrently monitor the two aspects of the cerebral response to

the stimulation, the neuronal and haemodynamic activity. This study has been published in the paper: Martina Giovannella, David Ibañez, Clara Gregori-Pla, Michal Kacprzak, Guillem Mitjà, Giulio Ruffini, Turgut Durduran, *"Concurrent measurement of cerebral haemodynamics and electroencephalography during transcranial direct current stimulation"*, Neurophoton. 5(1) 015001 (25 January 2018)

9.1 Background

In the introductory chapter of this thesis (chapter 1) I highlighted that diffuse optical neuro-monitors can be used to investigate the cerebral response to a stimulation thanks to the principle of neurovascular coupling. Specifically, we have here investigated the cerebral haemodynamics during and after transcranial direct current stimulation.

Transcranial current stimulation (tCS) is a non-invasive form of brain stimulation that applies weak direct electrical currents to the brain through electrodes placed on the scalp. Different types of stimulation are available based on how the current delivered to the brain is modulated [191]. The most common approach is to hold the current constant during the stimulation period, this is known as transcranial direct current stimulation. This method is commonly referred to as tDCS, but in order to avoid confusion with the optical method, we here use DC-tCS. DC-tCS induces bidirectional, polarity dependent, changes in cerebral excitability of humans [160, 179] and has been shown to modulate cognition in both healthy subjects (improvement of cognitive function) and in patients (reversing the effects of cognitive deficits after a stroke) [31, 32]. Positive effects have also been shown in treatment of depression, chronic and acute pain, Parkinson's disease, focal epilepsy and for improving recovery after stroke [27, 68, 71, 131]. A therapeutic application of this technique is appealing due to its relative low cost, to its demonstrated safety [8] and as a substitute for pharmacotherapy, especially for patients with poor drug tolerability [27]. In

order to define protocols of application and to optimize the individual dosage of stimulation, the effects of the stimulation on the cerebral activity must be monitored in real time [17, 197]. Availability of a concurrent read-out of the stimulation effects could improve its effectiveness and, ultimately, a personalized stimulation driven by the neuromonitor feedback can be imagined [117]. For this purpose, due to the complex nature of cerebral activity, multimodal monitoring is preferable [94, 189], such that different monitors integrated in a single set-up can allow to record the effects at different levels, from neuronal activity, to haemodynamics to systemic [92]. The neuronal activity is evaluated by electroencephalography (EEG) which measures the synchronous activation of a large population of pyramidal neurons oriented perpendicularly to the scalp. On the other hand, cerebral haemodynamics can be used as a surrogate measure of the cerebral activation assuming that cerebral blood flow (CBF) increases in a region of the brain where neurons and synapses are activated in order to meet the demand for more energy and that the amount of local increase of blood flow and the changes in oxygen saturation are related to the cellular energy consumption [185]. Even if different options are available as neuro-monitors of haemodynamics, functional near infrared spectroscopy (fNIRS) appears to be the best suited for this application [150]. fNIRS refers to the usage of NIRS technologies to investigate cerebral response to an evoked or spontaneous brain activation. It allows for continuous non-invasive measurements, does not require the immobility of the subject and it is not necessary to change the environment preferable for the stimulation to integrate fNIRS in the protocol [150]. These advantages are fundamental for this kind of application. CW-NIRS has indeed already been used as a monitor during DC-tCS, both in animals [82] and on humans at rest [118, 151, 154] and during tasks [101, 111, 118]. It has also been used together with EEG to monitor DC-tCS [109] and a device integrating the two monitors have been developed and characterized [129, 192]. Despite of the successes of these studies, it must be reminded that CW-NIRS does not allow a quantification of absolute value

of HbO_2 and HHb concentration, lacks precision and accuracy [93] and does not give a direct measure of CBF, the primary marker of the neurovascular coupling.

In this work, we propose to use time resolved NIRS (TRS) and diffuse correlation spectroscopy (DCS), together with EEG, as neuro-monitors of the brain stimulation. The hybridization of a commercial DCS device, HemoFloMo, and a prototype of a TRS device, TRS-20, presented in the previous chapter has been used for this purpose. Here HemoFloMo and TRS-20I are used together with EEG to monitor cerebral activity before, during and after ten minutes of DC-tCS over the frontal cortex. This area is the most convenient choice for the diffuse optical monitors because of the lack of hair. Since its stimulation has been proven effective for the improvement of various cognitive functions [47, 56, 65, 66, 107, 121, 155, 223], for example working memory enhancement [7, 67, 168, 227], and for treatment of depression [24, 131, 159], it is also a relevant area to stimulate and study.

9.2 Methods

9.2.1 Transcranial direct current stimulation and EEG device

DC-tCS was delivered using Neuroelectrics Starstim® (Neuroelectrics, Barcelona, Spain) which is a research-class eight channel transcranial current stimulator that is also capable of measuring EEG. 12 mm diameter silver chloride electrodes (Ag/AgCl) with conductive saline gel were used both for EEG recording and for stimulation. Eight electrode (AF7, AF8, FT7, FT8, TP7, TP8, PO7 and PO8) locations were chosen as depicted in figure 9.1(a) according to the 10-10 EEG system [112]. In particular, the active electrodes during stimulation were AF7 (left frontal lobe) and PO8 (right parieto-occipital lobe). From now on, we will refer to the former (AF7) as the stimulation electrode while to the latter (PO8) as the return electrode. All the eight electrodes functioned as EEG recording electrodes for protocol periods that did not involve stimulation.

EEG spectrum was sampled at 500 Hz.

9.2.2 Hybrid TRS-20I and HemoFloMo

Cerebral haemodynamics was monitored in this study using the device described in details in chapter 8. It is a hybridization of a commercial DCS device, HemoFloMo (HemoPhotonics S.L., Spain), and of a prototype of a TRS device, TRS-20 (Hamamatsu Photonics K.K., Japan). Therefore it can measure concurrently the cerebral blood flow in the microvasculature of the tissue and the blood oxygenation in the microvasculature of the tissue. In this measurement, the HemoFloMo averaging time was set to 1.5 s, while the TRS20I integration time was adjusted between 3-4 s depending on the counts collected in each subject. As explained, the sampling time was the sum of the two device acquisition times, with some delay due to the details of the hybridization, resulting in a sampling time of 6-8 s.

The probe 3D-printed in flexible material and used for this protocol is shown in figure 9.1(b). It can accommodate not only the fibers for DCS (source-detector separation 2.5 cm) and for TRS (source-detector separation 3.7 cm), but also an electrode. Two of these probes were placed on the forehead of the subject, one on the left hemisphere in correspondence with AF7, carrying the stimulation electrode, while the other on the right hemisphere in AF8 position with a purely EEG recording electrode. Two of the four sources available for HemoFloMo were used, one for the left and one for the right hemisphere. For each hemisphere, only one detection position was implemented using a bundle of four single-mode fibers probing the same area, *i.e.* all the eight detector channels were used. The correlation curves collected by four fibers in the same area were averaged in order to improve the signal-to-noise ratio. On the other hand, the two independent source-detector channels of the TRS device (TRS-20I) were used for the two hemispheres.

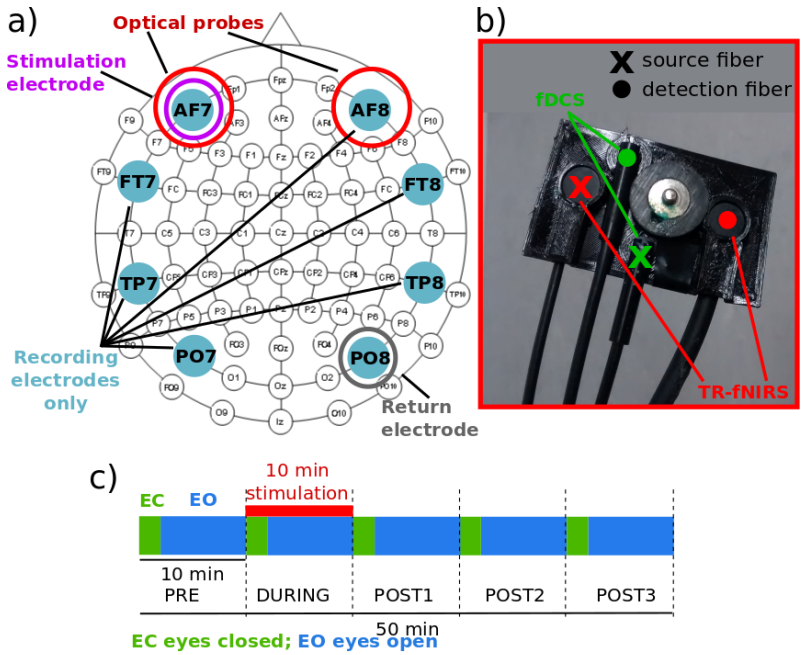

Figure 9.1: (a) A schematic of the optical probes, stimulating and return electrodes and EEG recording electrodes superimposed on a standard 10-10 EEG system. (b) Image of the integrated probe that could accommodate optical fibers (both for DCS and TRS) and an electrode. (c) Schematic of the protocol that lasted a total of fifty minutes divided in five ten minute periods. Stimulation was delivered during the second period.

9.2.3 Protocol

Healthy, right-handed adult subjects were recruited for three sessions of combined stimulation and measurement: anodal (i.e anode in AF7 (stimulation electrode) cathode in PO8 (return electrode)), cathodal (*i.e.* cathode in AF7, anode in PO8) stimulation sessions and a sham session. Such a montage creates an electric field that crosses the brain as confirmed by simulation of the electric field distribution in the brain (data not shown). For half of the subjects, the

anodal was the first session, while for the other half cathodal was. Sham stimulation was always given during the third session. All sessions were separated by a wash-out period of at least one week. The studies were approved by the ethical committee of Hospital Clinic in Barcelona. Each subject signed an informed consent and the study was conducted according to the principles of the Declaration of Helsinki. Exclusion criteria included the history of neurological and psychiatric conditions and the current use of psychoactive medications.

A schematic of the protocol is presented in figure 9.1(c). The protocol consisted of fifty minute measurement sessions divided in five periods. After ten minutes of baseline (PRE period), ten minutes of stimulation was given (DURING period), then thirty more minutes were recorded (POST1, POST2 and POST3 periods). During the stimulation, a current of 1 mA (resulting in a current density of 0.88 mA/cm^2) was delivered to the brain with a ramp up of 30 s at the beginning and a ramp down of 30 s at the end of the stimulation period. Such a duration for ramp up and down was chosen considering that a shorter one could cause a itching and disturbing sensation for the subject. In the sham session, the current was ramped up to 1 mA in 30 s and then brought back to zero in 30 s. After eight minutes, it was again ramped up and down to simulate the real stimulation sessions. This design gave the subjects the same feeling as a real stimulation because the ramp up and down periods are usually the most noticeable moments. However, the stimulation was too short to have significant, durable effect on the brain activity.

For each ten minute period, the subject was asked to close the eyes for the first two minutes (from 0 to 2, from 10 to 12, 20 to 22, 30 to 32 and 40 to 42 minutes). During the eyes-open condition, subjects were requested to stare at a screen where a cross was shown to change colour or to rotate at random time (but between every 20 or 30 s) and to press a key when the cross configuration changed to maintain the subject gaze and attention to a fixed point.

9.2.4 Data analysis

Optical data

TRS measurement acquired by TRS-20I were analyzed using all the three methods described in section 3.1.3: the DPF and variance analysis, for which the first ten minutes of the protocol were used as baseline, and the fitting analysis. For this, only μ_a was used as a fitting parameter, while μ_s' was fixed at baseline values. This helps improving the stability of the derived absorption coefficient, used to retrain HbO_2 and HHb concentration absolute values. This approximation assumes the metabolic changes to only affect the blood oxygenation but not the tissue scattering properties, considering the fact that red blood cells are only a small factor of the total scatterers.

DCS measurements were analysed using the solution for the diffusion equation of the electric field autocorrelation function for the semi-infinite medium to derive the blood flow index (BFI) as explained in section 3.2.3. Optical properties derived from TRS were used in the analysis. Once derived, the BFI, a measure of CBF, was normalized to the baseline (first ten minutes of acquisition) to obtain a measure of relative CBF (rCBF).

EEG

Changes in the EEG patterns induced by the brain stimulation were independently analysed for eyes open and closed conditions. Pre- and post-stimulation EEG recordings were filtered using a finite impulse response filter of 500 coefficients with cut-off frequencies set to 1 Hz and 20 Hz. Filtered recordings were split into 60 second blocks in which power at delta (2-4 Hz), theta (4-8 Hz), alpha (8-13 Hz) and beta (12-18Hz) bands were calculated. Each 60 second block was further split into two second windows with a 50% overlap. After individual epoch de-trending, those epochs containing samples larger than 75 μV, considered high amplitude artifacts, were rejected. Relative power at the previously defined frequency bands was calculated via trapezoidal power spectral density

(PSD) integration and were normalized with respect to the full band power (2-18 Hz). Power at 60 second blocks was calculated as the average power of artefact-free two second epochs.

Statistical data analysis

Outlier detection was implemented by analysing the functional depth [9, 63], *i.e.* the centrality of a given curve within a group of trajectories, with each curve representing the response of cerebral haemodynamics or EEG power. The R package [209] *fda.usc* [64] and the R function *Outliergram* [9] were used as tools for this purpose. The outlier detection was run in the two hemispheres independently for the cerebral haemodynamics and for each electrode and band for the EEG response. A subject was defined as an outlier if it was detected by both methods simultaneously and was, thus, removed from the statistical analysis. If a subject was defined an outlier for HbO_2 concentration, it was removed also for HHb concentration, and vice versa.

A linear mixed effects (LME) analysis was performed to test the effect of the stimulation session and time on the cerebral haemodynamics and EEG response using the R package *lme4* [15]. For cerebral haemodynamics, we treated the two hemispheres independently building an LME model for each of them. To include time, we selected periods of 4 minutes during which we averaged the response: minute 14 to 19 as DURING DC-tCS period, minute 24 to 29, 34 to 39, 44 to 49 as POST1, POST2 and POST3 DC-tCS periods respectively. Response was normalized to the last 4 minutes of the PRE-period, therefore this period was not introduced in the analysis. EEG power change with respect to initial baseline, each band and electrode was evaluated separately, as well as eyes opened and eyes closed periods. POST periods were introduced in the LME by averaging the response in each of them. In all the models, the period and the stimulation type (and their interaction) entered as fixed effects. As random effects, the intercepts for subject and the random slope for period on a subject basis were considered. For EEG only a random

intercept was used since the model would not converge if the random slope had also been added. Residuals plots were tested for the inspection of deviations from homoscedasticity or normality. Models were built with forward steps following likelihood ratio tests of the model with the effect in question against the model without the effect in question. The bayesian information criterion (BIC) parameter was considered to assess whether the effect was improving the model. Stimulation type was the first to be tested. If found significant, the period was added and a new model was tested. If this step was also successful, the interaction between the two was also tested.

Post-hoc analysis was performed with R package *lsmeans* [133] to quantify changes in haemodynamics parameters and in EEG power for each stimulation session and period. To this end, least-square means of the linear model were calculated and the different sessions were compared using the Tukey correction for multiple comparisons. For data visualization, a bootstrap sample was calculated for the time series of cerebral haemodynamics parameter. The bootstrap method is based on consecutive and random re-sampling of the sample distribution [36] and was implemented in the R package *fda.usc* [64].

9.3 Results

A total of twenty healthy subjects (nine female) participated in anodal and cathodal stimulation sessions. Twelve of them came back for a sham session. Technical problems resulted in one subject for TRS measurement being discarded for the cathodal session leaving nineteen subjects for HbO_2 and HHb concentration measurements. In addition, one DCS measurement was discarded during the sham session leaving eleven subjects for flow measurement during sham stimulation. Technical exclusion criteria for EEG, explained in the data analysis section, resulted in twenty subjects for anodal, sixteen for cathodal and nine for the sham session. As explained above, outliers were detected and excluded from the statistical analysis. Number of subjects surviving

the outlier detection for EEG and haemodynamics parameters are presented in table 9.1 and table 9.2 respectively.

	Sham				Anodal				Cathodal			
	α	β	δ	θ	α	β	δ	θ	α	β	δ	θ
AF7	9	8	9	8	20	20	19	19	15	15	16	15
AF8	9	9	9	8	20	19	19	19	15	15	16	15
FT7	9	9	9	9	19	19	18	19	16	15	16	14
FT8	9	9	9	8	20	17	19	20	16	15	14	15
PO7	9	9	9	8	19	19	19	19	16	15	16	15
PO8	8	9	9	7	20	19	18	19	15	15	16	15
TP7	9	9	9	8	19	19	19	19	15	14	16	15
TP8	9	9	9	7	18	19	19	18	15	15	16	15

Table 9.1: Number of subjects for EEG that were used for the statistical analysis for each electrode and for each band(alpha (α), beta (β), delta (δ) and theta (θ)), after the technical exclusion criteria and outlier detection.

	Sham		Anodal		Cathodal	
	Left	Right	Left	Right	Left	Right
CBF	11	11	18	18	20	18
HbO_2 and HHb	12	12	18	19	17	17

Table 9.2: Number of subjects for haemodynamics parameters that were used for the statistical analysis after the technical exclusion criteria and outlier detection.

In figure 9.2, the time series of rCBF change, averaged over subjects, is shown together with the bootstrap sample. Only results from the left hemisphere (ipsilateral side, under the stimulation electrode) are shown from the three different stimulation sessions.

When building the LME model from the null one, the stimulation type is found to improve it for blood flow in the left hemisphere, but not in the

right one. Therefore, blood flow response depends on the stimulation in the ipsilateral hemisphere, but not in the contralateral one. Period is not an effect that improves the model for neither of the hemispheres. Accordingly, we can conclude that blood flow stays constant at the end of the stimulation period (DURING) and in the POST periods. Post-hoc analysis results are summarized in figure 9.6. Blood flow increases significantly from the baseline by 10% (C.I. 7%-14%) for anodal ($p < 0.001$) and 11% (C.I. 7%-15%) for cathodal ($p < 0.001$) stimulation while no increase is seen in the sham session ($p = 0.07$). A comparison between the different sessions revealed a detectable difference between anodal and sham ($p = 0.008$) and cathodal and sham ($p = 0.003$) sessions while no difference is seen between anodal and cathodal sessions.

In figure 9.3, the results for the time evolution of HbO_2 concentration from TRS measurements using the three different analysis methods are shown for anodal and sham stimulations for the left (ipsilateral) hemisphere. DPF analysis gives an increase of HbO_2 concentration starting during the stimulation and persisting after it. Notably, this change is seen both in the anodal and sham sessions. The results obtained with the analysis of variance and by fitting are comparable and show smaller changes than the DPF analysis both in anodal ($p < 0.001$) and sham ($p < 0.001$) sessions. For this reason, the fit analysis results are used for building the LME model for the changes in HbO_2 and HHb concentrations. Furthermore, this is what is most commonly used for TRS analysis [211]. Figure 9.4 and figure 9.5 show the average time evolution and the bootstrap sample from all the subjects for HbO_2 and HHb concentrations respectively in the left hemisphere during the three stimulation sessions. As for the blood flow, among the effects considered in the LME model and listed in the Methods, only the stimulation improves the model. For both variables, the changes depend on the stimulation session but a recovery is not seen in the 30 minutes of POST periods, because the period is not a significant effect for the model.

As summarized in figure 9.6, HbO_2 concentration increased by $0.5\mu M$ (C.I.

$0.1\mu M$-$0.8\mu M$) during anodal session ($p = 0.002$) and by $0.5\mu M$ (C.I. $0.2\mu M$-$0.8\mu M$) during cathodal ($p = 0.001$). As expected, the changes in HHb concentration were opposite to HbO_2 concentration. HHb concentration decreased by $-0.3\mu M$ (C.I. $-0.5\mu M$-$-0.1\mu M$) during anodal session ($p < 0.001$) and by $-0.3\mu M$ (C.I. $-0.5\mu M$-$-0.2\mu M$) ($p < 0.001$) during cathodal session. No change was seen in the sham session ($p = 0.1$ for HbO_2 and $p = 0.07$ for HHb concentration). A difference was detected by our model for HbO_2 concentration between anodal and sham ($p = 0.004$) sessions, as well as between cathodal and sham ($p = 0.003$) sessions. On the other hand, a pair comparison for HHb concentration gave a significant difference only between cathodal and sham sessions ($p = 0.03$).

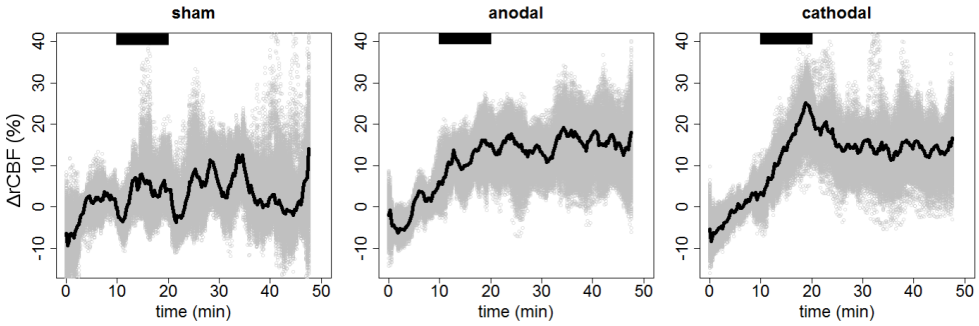

Figure 9.2: rCBF change during the three types of stimulation sessions on the left hemisphere. The thick black line is the average, the grey area represents the bootstrap sample over all the subjects. The black horizontal bar highlights the stimulation period.

A frequency range from 1 to 20 Hz was considered for the EEG analysis. The lower limit was chosen because artifacts derived from movement and subsequent changes in the skin-electrode impedance affect mostly the low EEG frequencies. Furthermore, a time-frequency analysis of each recording was performed in order to study the signal quality of the data set. In many recordings,

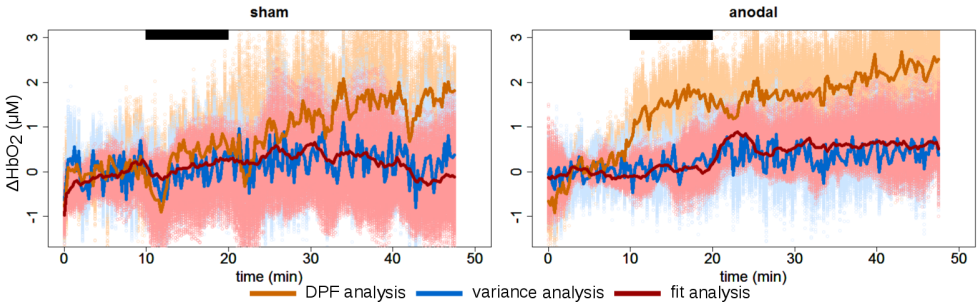

Figure 9.3: Changes in oxy-haemoglobin (HbO_2) concentration during sham and anodal stimulation, in the left hemisphere, according to the three types of analysis considered for TRS: orange for DPF analysis, blue for the variance and red for the fitting analysis. Continuous line is the average of all the subjects, the lighter coloured region represents the bootstrap sample with the same colour code. The black horizontal bar highlights the stimulation period.

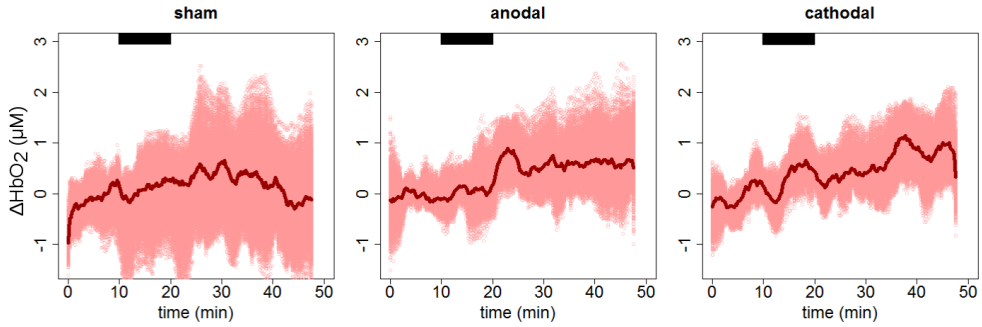

Figure 9.4: Oxy-haemoglobin (HbO_2) concentration during the three types of stimulation sessions on the left hemisphere from the fit analysis. The thick line is the average, the lighter coloured region represents the bootstrap sample over all the subjects. The black horizontal bar highlights the stimulation period.

the EEG spectrum was affected by external interferences in frequencies above 22 Hz. It was then decided to choose an upper cut-off frequency of 20 Hz to

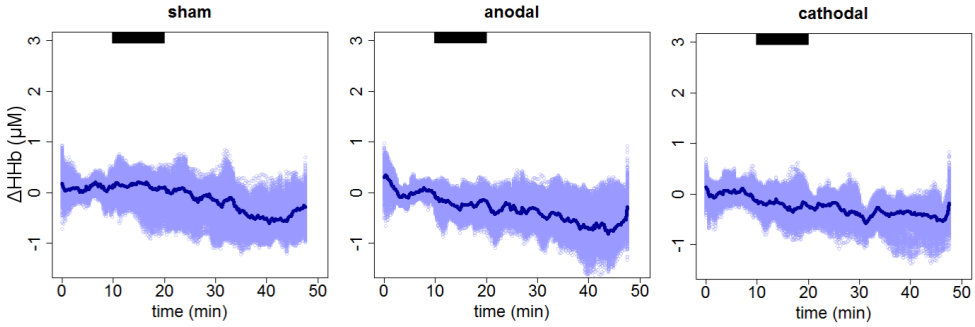

Figure 9.5: Deoxy-haemoglobin (HHb) concentration during the three types of stimulation sessions on the left hemisphere from the fit analysis. The thick line is the average, the lighter coloured region represents the bootstrap sample over all the subjects. The black horizontal bar highlights the stimulation period.

avoid this noise. As a result, the beta band covers 13 Hz to 20 Hz. In addition, after the temporal and spectral inspection of the EEG spectrum that was acquired during the stimulation, we have concluded that the quality was not sufficient to perform a reliable EEG analysis. Therefore, only recordings before and after the stimulation were used. Going through results obtained in EEG power, the changes in resting-state across stimulation modalities were observed only in the eyes-open condition. Figure 9.7 shows barplots for bands and electrodes where response was affected by the stimulation session according to LME model. Post-hoc analysis resulted in a statistically significant power decrease in delta band in TP8 after every stimulation type. Statistically significant differences between anodal and cathodal sessions ($p < 0.001$) and anodal and sham sessions ($p = 0.02$) were observed. A statistically significant power decrease in the theta band after cathodal stimulation in fronto-right region (AF8, FT8) was observed. Statistically significant differences between cathodal and sham sessions ($p = 0.002$ in both electrodes) and cathodal and anodal sessions ($p = 0.002$ in both electrodes) were also observed. A more widespread

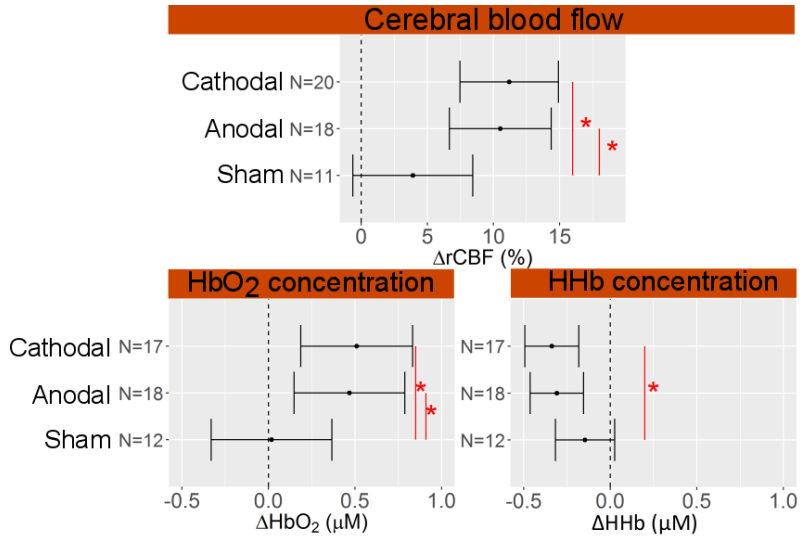

Figure 9.6: Changes of cerebral haemodynamics parameters during and after the stimulation sessions, as obtained by the LME model with the 95 % confidence interval as the errorbars. N refers to the number of subjects used for the statistical analysis. Red * highlights statistically significant difference between stimulation sessions. Dashed vertical line represents the zero level.

effect in the beta band was observed. All electrodes in the tempo-parietal (TP7 and TP8) and parieto-occipital (PO7 and PO8) lobes experienced a statistical significant increase after sham, but, not after any active stimulation. In all these electrodes, the difference between anodal and sham sessions ($p = 0.004$ for TP7,$p = 0.01$ for TP8, $p < 0.001$ for PO7, $p = 0.002$ for PO8) and cathodal and sham session were significant ($p < 0.001$ for all electrodes).

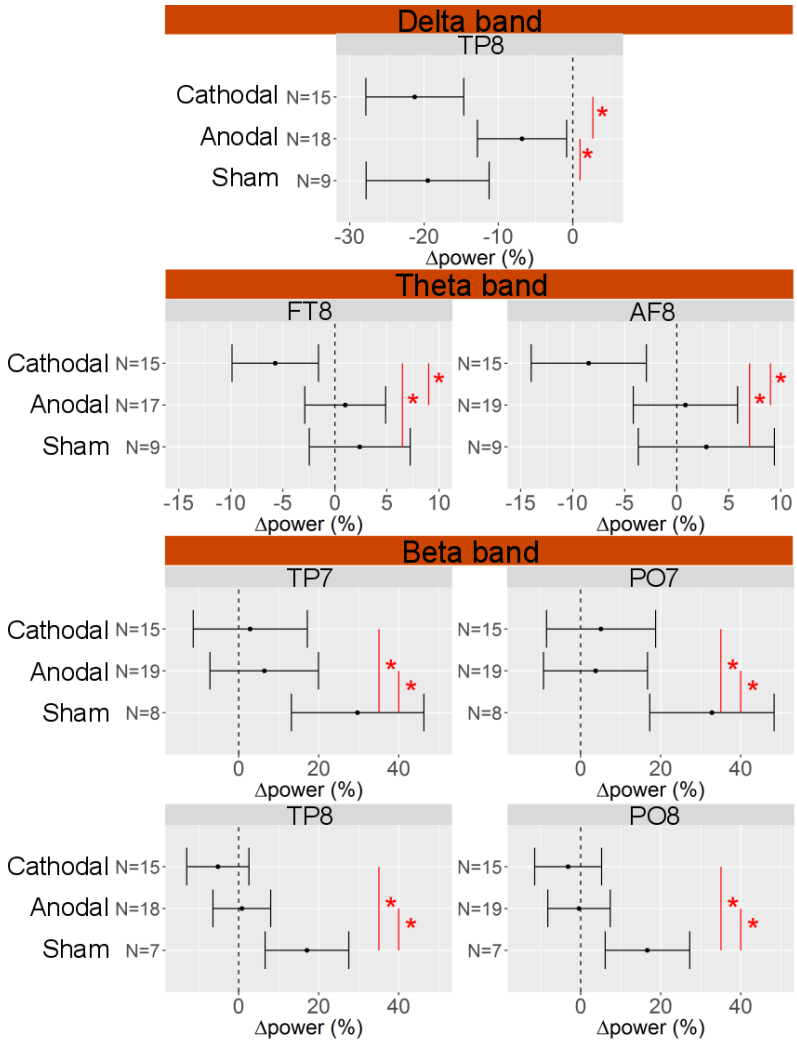

Figure 9.7: Change of electroencephalography (EEG) power in electrode TP8 in the delta band, electrodes AF8 and FT8 in the theta band and electrodes TP7, PO7, TP8, PO8 in the beta band caused by the three types of stimulation, as obtained by the LME model, with 95 % confidence interval as the errorbars. N refers to the number of subjects used for the statistical analysis. Red * highlights the statistical significant difference between stimulation sessions. Dashed vertical line represents the zero level. Only bands and electrodes with statistical significant changes are shown.

9.4 Discussion

In this work we have introduced the use of functional diffuse correlation spectroscopy (DCS), together with time resolved functional near infrared spectroscopy (TRS), as neuro-monitors of cerebral haemodynamics during and after transcranial direct current stimulation (DC-tCS). The former has allowed the direct measurement of cerebral blood flow (CBF) primary biomarker of the neurovascular coupling. The measurement of cerebral haemodynamics was concurrent to electroencephalography (EEG) which measures electrical activity. Therefore, information on both haemodynamics and neuronal activity from the same run of the protocol were available.

I discuss results of linear mixed effect (LME) models for haemodynamics and EEG. LME models take into account variability within subjects and are dependent on the numbers of degrees of freedom. The methods section explains how the LMEs were built and the results section explains in detail the resulting models and the significant effects on EEG and haemodynamics found through those models. It must be highlighted that these results valuably describe the group response to the stimulation, while they do not give information on the response of each subject. This would be useful if the haemodynamics data must be used for tailoring the stimulation on each specific subject. This is however a preliminary work that aims at assessing the feasibility of optical and EEG recording and the description of the "average" response to the stimulation.

9.4.1 Cerebral haemodynamics

Statistical analysis confirms that CBF increases in the left ipsilateral hemisphere (in the region under the stimulation electrode) during anodal and cathodal sessions but not during the sham session. CBF does not recover during the 30 minutes following the stimulation. This is consistent with the fact that if the stimulation is applied for a period longer than 9 minutes, the effect of the stimulation persists long after the stimulation ends [127]. Specifically, our statistical

model results in a 10% increase during anodal session and 11% during cathodal and gives no difference between the two stimulation conditions. This amount for CBF change is similar to what was assessed with arterial spin labelling MRI (ASL-MRI), a magnetic resonance imaging (MRI) technique, [229] but, is much larger than what measured by positron emission tomography (PET) [128]. In reference [128], scans taken during the following hour after the stimulation were averaged, while we have measured only the following 30 minutes, which may account for some of the difference in our results. The optical probe placed in the right contralateral hemisphere did not detect any change in CBF in this region. The work done with PET [128] allowed for whole brain imaging and detected regional increases in different areas of the brain, even far away from the stimulation electrodes, after both anodal and cathodal sessions compared to sham. Although anodal stimulation proved to cause a more widespread increase of regional CBF than cathodal stimulation, the same effect was seen for both stimulation types in the region under the electrode, which is consistent with our results.

As far as TRS measurement are concerned, I will here discuss results of the fit analysis. In this protocol, HbO_2 concentration increases and HHb concentration decreases in the left hemisphere during both anodal and cathodal stimulations, but not during sham. The right frontal lobe (contralateral to the stimulation) does not present changes in the oxygenation as is also true for CBF. Even if changes retrieved were very small, less than $1\mu M$, HbO_2 and HHb concentrations can mark the status of the ongoing stimulation. As a matter of fact, the changes are statistically significant during both anodal and cathodal sessions but not during the sham session. HbO_2 concentration is a more robust marker, since response to anodal and to sham sessions are statistically significantly different, as well as the response to the cathodal and to sham sessions. On the other hand, for HHb concentration, the contrast-to-noise ratio is not enough to give a statistically significant difference between anodal and sham sessions, but a decrease is not seen in the sham session. The

directions of HHb and HbO_2 concentration changes are consistent with what is expected in case of a cerebral activation and what was previously found in the literature [118, 151]. Specifically, due to the neurovascular coupling, when a cerebral region is activated, CBF is recruited to meet the additional demand of oxygen and it increases [185]. Concurrent to this, an increase of HbO_2 concentration and a decrease of HHb concentration is usually detected [199]. This suggests that the brain is over supplied by oxygen by the increase of CBF compared to the oxygen consumption. The details of this process is, in fact, more complex [185]. The time series of the haemodynamics parameters in figure 9.2, 9.4 and 9.5 suggest a more steep increase of CBF than the HbO_2 and HHb concentrations. The above mentioned mechanism of neurovascular coupling can explain this [199]. Right after the stimulus, the supply of CBF does not overcome the need immediately. Only after this happens, a HbO_2 concentration increase and a HHb decrease is detected. This process was previously verified during *in vivo* protocols [188]. Nonetheless, to make quantitative inferences on the time lag, we should have had a better time resolution than what we have here.

Different source detector separation for TRS and DCS

Explaining DCS data analysis, it was highlighted that optical properties measured by TRS are used for DCS analysis. It must be noted that source detector separation for the two was different (2.5 cm for DCS and 3.7 cm for TRS). Since our analysis assumes that the underlying tissue is homogeneous, we can tolerate this difference. In addition our results are relatively insensitive to small inaccuracies of the bulk optical properties, since we focus on the measurement of relative CBF [53].

Possible influence on skin perfusion

It is known that diffuse optical techniques measure a mixture of extra- and intra-cerebral perfusion [13]. This could be a confounding factor since DC-tCS causes a "skin redness" (erythema), that may lead to changes in the skin perfusion of different amounts between active and sham stimulations [8]. However, the properties of photon diffusion into the tissue help us in explaining that response detected in this protocol is not mainly due to changes in skin perfusion due to the stimulation induced skin redness. The visitation probability of photons traveling into the tissue has a so-called "banana-shaped" pattern and touches the skin mainly in the region corresponding to the source and detector fibers [171]. In our case, the fibers are separated by a distance of 25 mm while the electrode, placed in the middle has a diameter of 12 mm. If we consider that various works [58, 212] have shown that the erythema is concentrated in the area under the electrode, our optical monitors are not particularly sensitive to this redness. Furthermore, a recent study [116] measured the temperature under the electrode during the stimulation, detecting a non-significant change after 10 minutes of stimulation (our total time of stimulation). Only after 20 minutes of application a significant increase of 1.36° was detected. However, we should account for the fact that this work used a larger electrode resulting in a lower current density than ours (0.06 mA/cm^2 versus 0.88 mA/cm^2). Interestingly, there is evidence suggesting that the current intensity and the electrode area are more important parameters leading to increased redness and discomfort due to the stimulation of more cutaneous receptors [212]. In the above mentioned reference [116], temperature was measured using a current intensity of 2 mA, larger that what was used in our experiment. Therefore, we expect a minimal, non-significant temperature increase in our case. Another indication that the observed, long-term changes are not purely due to skin redness is that it is known that erythema disappears within thirty minutes after the stimulation [81]. In our case, the stimulation response did not decrease after thirty minutes.

Results from different type of TRS analysis

Even if fit analysis is the most used methods for TRS curve analysis, I also explored other methods. DPF analysis was considered to understand which results would have been obtained using a typical one distance CW-NIRS setup. While the variance method was meant to compare the fit results with a method that has proven to be more sensitive to deeper layers. DPF analysis shows an increase of about 2 μM in HbO_2 concentration in the left hemisphere compatible with what was previously found in the literature [118,151]. This increase is seen in active and sham stimulations where the brain is not actually stimulated which questions its validity. Focusing on the results given by the analysis of variance, the second moment of the DTOF, we retrieve smaller changes both in anodal and sham session respect to DPF analysis. Notably, the variance of TRS curves is more sensitive to the deeper layers respect to the intensity, the parameter used in the DPF analysis [137]. This may suggest that results in DPF analysis are contaminated by superficial effects present both during anodal and sham stimulations. Moreover, these results are in accordance with a previous single subject experiment where TRS was used during anodal stimulation [154]. In this work TRS measurements were analyzed with a gated analysis [232]. This method exploits the depth information encoded in time in the broadened pulse collected after propagation into the tissue, and allows to decouple changes in the extra-cerebral and cerebral layers. Measurements performed on a single subject during anodal stimulation retrieved a larger HbO_2 concentration change in the superficial than in the deeper layer, which would be heavily reflected in the DPF analysis. We would like to point out that the time gating analysis of TRS was not implemented here because the lack of knowledge of the extra-cerebral layer thickness on an individual basis compromises the validity of this method [183].

Cerebral haemodynamics response not dependent on stimulation polarity

It is interesting to observe that both the anodal and cathodal stimulation sessions have created similar changes in the haemodynamics parameters. All the reviewed and cited published works [128, 229] that measure cerebral haemodynamics during DC-tCS show the same pattern for both cathodal and anodal stimulations in the region under the electrode. Our results confirm these findings. In addition, positron emission tomography (PET) studies concurrent to transcranial magnetic stimulation (TMS) also demonstrate an increase in CBF in the region under the stimulation for both excitatory and inhibitory protocols [190]. These results suggest that CBF is not a marker of the polarity of the stimulation, at least in the directly stimulated area, and that regardless of whether the stimulation results in an activation of inhibitory or excitatory synapses, it leads to an increase in blood flow. It has been highlighted that this behavior of CBF reflects the local levels of synaptic activity in intracortical neurons and inputs to those areas rather than the activity of output neurons which is opposite when the stimulation is excitatory or inhibitory [128, 143].

9.4.2 EEG

The stimulation protocol used in this study influenced EEG rhythmic activity at different bands and electrodes. Comparing the results from previously published studies about DC-tCS on the frontal cortex is not a trivial task since EEG response depends heavily on the electrode montage [2]. All of the previous studies used F3 as the stimulation electrode while the return electrode, here referring to the electrode not placed in the frontal cortex with opposite polarity, was placed either on the supra-orbital region or on extra-cerebral regions. In contrast, we have decided to use the AF7 electrode as stimulation electrode because the optical measurement series on the frontal brain region are more reliable due to the absence of hair. The return electrode was chosen

to be spatially and functionally distant from the stimulation electrode in order to minimize the interactions and to stimulate the frontal region unilaterally. Moreover, few studies measured the EEG spectrum at rest while most of them assessed the response to a task and how this can be influenced by the stimulation. It must be noted that a recent systematic review highlighted that results in the EEG spectrum of the same protocol were not consistent within different works [91]. They concluded that there is no evidence that EEG spectrum is affected by the stimulation. It may also be hypothesized that, since it is not trivial to maintain subjects in a well controlled condition, the variability of the effects is increased. We note that the protocol is fifty minutes long which may have led to a sense of drowsiness and/or fatigue in the subjects which could alter the cerebral electrophysiology and metabolism. The staring and attention tasks were implemented to minimize this effect. Furthermore, the transition from eyes open and closed and vice versa also helped with this issue. In spite of this, we cannot exclude that some of the subjects may have been affected and we do not have any control over this.

In order to define EEG spectrum results, effects in different frequency bands have been studied since different bands are traditionally related to different brain functions. It is however controversial whether the activity at a certain frequency band is related to a single brain function or that complex stimuli are reflected on a single oscillatory activity [14]. This may explain the multiplicity of bands affected by our protocol.
The protocol applied in this study influenced brain activity in the delta, theta and beta bands. No effect was detected in the alpha band which is consistent with previous works [91]. We will focus from now on on the bands where the stimulation has proven to be effective. The changes in the delta band were observed in the right tempo-parietal region after all stimulation sessions but were significantly smaller in the anodal session compared to the other two. On the other hand, changes in the theta band occurred in the right fronto-temporal area exclusively after cathodal stimulation. Interestingly, delta and

theta bands are associated to functions linked to the frontal cortex which was stimulated in our protocol. It is an indication of activity in cognitive and memory performances [124], attention [83] and working memory [194]. A response in these bands is consistent with previous work. Specifically, a lower power in delta and beta bands after the stimulation compared to sham has been previously observed [113, 223], where pre- and post-stimulation spectral power were not calculated but the comparison between stimulation sessions was done in absolute values. This effect has only been found in the frontal cortex, in contrast to our findings, but both stimulation and return electrodes were placed on the anterior part of the head, while we have an electric field crossing all the brain. A significant and selective decrease of the power of theta band in the right inferior frontal gyrus area has been reported after DC-tCS stimulation along with an improvement in behavioural inhibition [104].

Differences in EEG power across different stimulation sessions were also seen in the beta band. Power increased after sham session in temporal and parietal region, but not after active stimulation sessions. An unchanged or a decreased level of beta activity is usually observed in tasks where behaviour is driven by bottom-up signals, while enhancement occurs if the system has to actively maintain endogenous attention [57]. It may be hypothesized that the detected increase in beta activity is linked to a active effort to maintain the cognitive concentration state required for the sustained attentional task along the experimental protocol. This activity was present during sham but not during active stimulation sessions. Several references highlight an influence of DC-tCS when applied on the frontal cortex, on sustained attention [73]. In our protocols, same effects for anodal and cathodal session was found in the EEG beta band in the posterior part of the brain, without a differentiation due to the polarity. Intuitively this is not expected because opposite polarity stimulation should produce an opposite electric field in the brain, *i.e.* either excitatory or inhibitory. Nonetheless, it must be mentioned that the predominance of excitatory or inhibitory electric field in an area of the brain does not exclude that

some "pockets" of the opposite direction are present [126]. We can speculate that only excitatory areas influenced the power in the beta band in the posterior area of the brain in our protocol. Unfortunately, this is prohibitively hard to confirm since not only the electrode montage but also the concurrent tasks alter the response to a certain polarity of stimulation [201, 204], *i.e.* it would require a special protocol to address this. For our protocol, the attention task was not the primary goal.

9.4.3 Correlation between cerebral haemodynamics and neuronal activity

Lastly, it was verified whether the change in CBF in the left frontal cortex due to stimulation has any correlation with the power change respect to baseline in any of the EEG bands and electrodes. This was done even for the electrodes far away from the optical probes since the source of the EEG signal can lay far from the scalp point where it is registered and its exact location cannot be determined well due to the inverse problem [75]. The Pearson correlation coefficient was calculated and a correlation was defined significant if, by bootstrapping the sample (*i.e.* repeating the analysis removing one subject at time), the correlation stays significant. After this analysis, we have found a negative correlation in the delta band for electrode FT8 with a Pearson correlation coefficient of R=-0.6. This is consistent with a predicted and verified decrease in lower frequency band during activation [119, 144]. The study of the correlation between the haemodynamics and neuronal activity is a very appealing topic due to the important information on the neurovascular coupling it could provide. It is also a very complicated process since several factor can contribute to the failure of the correlation between EEG activity and haemodynamics [186]. A detailed characterization of this is beyond the scope of this work, which aimed at the introduction of hybrid diffuse optical devices for monitoring the response to the stimulation, and requires a dedicated protocol with more regions probed for haemodynamics.

9.5 Conclusion

We have shown that DCS and TRS are suitable tools to monitor cerebral haemodynamics during and after DC-tCS and they can be integrated with EEG which monitors the neuronal activity. We have found CBF to be a good indicator of the ongoing stimulation since it shows an increase during and after anodal and cathodal stimulation in the region under the stimulation electrode. Results obtained with TRS show small changes of HbO_2 and HHb concentrations but the effect of the stimulation was still detectable. By concurrent EEG recordings, we could follow the modulation of the underlying neural oscillations. DC-tCS over the frontal cortex induced statistically significant power changes across different stimulation sessions in delta, theta and beta EEG rhythms.

Part IV

Conclusions and references

Chapter 10

Conclusions

Two hybrid devices integrating time resolved near-infrared spectroscopy (TRS) and diffuse correlation spectroscopy (DCS) have been developed, tested and exploited for monitoring cerebral haemodynamics in both adult and infant populations. Such devices allow for the simultaneous and independent measurement of microvascular cerebral blood flow and of the blood oxygen content in the microvasculature of the tissue. They make possible to measure non-invasively and continuously cerebral haemodynamics and metabolism at the bed- or cot-side.

The core of this thesis is the work developed within the BabyLux project. Together with the consortium involved in the project, I have developed a hybrid DCS and TRS device that could be used as a neuro-monitor for the premature newborn infants. The device has been built targeting this population and it had to be robust, portable and user-friendly to be used by the clinical personnel in the neonatology units.

Apart from describing the device and the protocol applied to test it in laboratory settings, other important technological aspects have been described in this thesis, whose importance goes beyond the BabyLux device.

First of all, through realistic simulated data, I have described the lower

limits to be expected from such a device in terms of precision and accuracy. This was tailored to measurement of the neonatal head but it can be extended to other DCS and TRS devices and to other populations.

Furthermore, I have validated DCS-measured cerebral blood flow (CBF), the BFI, against the gold standard positron emission tomography on a piglet model. I have obtained a calibration formula to turn BFI in flow units which gave satisfactory results in piglets and infants.

Two equivalent BabyLux devices were built and successfully validated in clinical settings by the end-users, *i.e.* neonatologists. In particular, we have demonstrated that the BabyLux device could measure in a complicated environment such as the delivery room, following the transition after birth, not losing more data than the commercial pulse oximetry and providing results not in contrast with previous findings.

Clinical testing focused, in addition, on the reproducibility of the measurement over probe replacement. Performance for StO_2 were improved compared to the cerebral oximeters, while variability of BFI was comparable to other technologies, which, in any case, measure with different time and space resolution.

Therefore the BabyLux device improves the state of the art, *i.e.* commercial cerebral oximeters, because it adds information on blood flow and provides better precision in oxygen saturation estimation.

The feedback received and the experience gained during the clinical studies with the BabyLux device can help with the first upgrade of the device. Updates can be, for example, providing more power from the TRS lasers, to lower the test-re-test variability of oxygen saturation, or improving the software, to reach an even more user-friendly graphical user interface. Inter-subject variability of BFI is a further point to improve, for example by increasing the signal-to-noise-ratio of DCS. Adding more detectors, or improving the engineering of the probe, to be less sensitive to pressure, movement, head curvature, are some of the first actions to initiate. Furthermore, the upgrade should be focused on

the safety features in order to be able to start the process of CE approval for medical devices and to make it easier to start clinical research on a larger scale.

Meanwhile, more clinical studies are ongoing with the device and further are planned. New studies focus mainly on preterm infants, the target population which was not measured during this thesis' work. First results on preterm newborns confirm the usability of the device and its probe on smaller heads.

The importance of the BabyLux project results lays in contributing to bridge the gap between research and clinical market. Hybrid DCS and TRS devices had been previously used for small studies on term and preterm infants, however the BabyLux device is the first device specifically designed for this purpose. Its user-friendliness allowed the clinicians to acquire data with minimal technical support and no adverse effects have been registered during data acquisition, even in extreme conditions such as the delivery room. This work lays the ground for a new generation of neuro-monitors for the infants brain and paves the way of more extensive clinical studies, involving more clinical centers.

In the last part of this thesis I have presented the hybridization of a commercial DCS and a prototype for a TRS. A detailed explanation of the robust integration of the two devices is of interest to eventually reproduce it. Having such hybrid devices available in non-technical research groups could expand and push forward research on various applications.

In this thesis the integrated device has been employed to measure cerebral haemodynamics of healthy adult volunteers. Specifically I have monitored the local CBF before during and after transcranial direct current stimulation for the first time. Such a neuro-monitor can be used for basic research on the effect of the stimulation but also to ultimately tailor the protocol to the subject necessity. Next steps will require to investigate the cerebral haemodynamics in specific interventions, including tasks, and to correlate the haemodynamic response, during or after the stimulation, to patient or subject outcome.

Results discussed throughout the thesis are positive and appealing, however

it must be reminded that several challenges are still to be solved for ultimately pushing diffuse optics towards clinical application. Some of the limitations of these technologies require to push physics research instead of a purely engineering efforts. One example is the fact that BFI absolute measurement is still not reliable enough for clinical purpose. One weak point, leading to high BFI variability, is the inaccurate determination of reduced scattering coefficient μ_s'. To tackle this point, work must be done on the model used for analysis, since the diffusion approximation already theoretically estimates μ_s' with an error of about 10%. Model based on the radiation transport equation have been published over the years, but they are still too complex to be employed for *in-vivo* data. Another improvement could focus on narrowing the pulse width of the instrument response function to increase the sensitivity of TRS measurement to μ_s'. Work is being carried on mainly on the detector side, focusing for example on silicon photomultipliers, lowering the noise and improving the timing resolution of this electronics.

A further unresolved problem regards the physical origin of the quantity measured by DCS. Specifically, BFI is surely proportional to blood flow but it depends on a variety of other parameters, the haematocrit and the vessel diameter and dimension in the probed tissue, among others. The fact that we do not have control of all the sources of the signal increases the variability of the measurement. A deeper insight on the origin of the BFI value would be useful for fundamentally understanding its relationship with the tissue blood flow and to make the BFI absolute value a measure of absolute blood flow useful and reliable for clinical application. Currently, DCS community is focused on theoretical and numerical studies, that will have to ultimately be translated in experimental measurement.

A common problem for all diffuse optical technologies used as brain monitors is the extra-cerebral contribution to the signal detected. This is not a major issue for the infant application, due to the thin skull and scalp of the newborns and infants, but it is for adult brain monitoring, as discussed in Part

3 of this thesis. To this purpose, research has been focused on theoretically studying the depth sensitivity and selectivity of diffuse optical technologies. Interestingly, previous studies have shown a larger sensitivity to the brain for both DCS and TRS compared to CW-NIRS. On the other side, data analysis and experimental protocols have been developed in order to improve the sensitivity to the brain haemodynamics. These new methods have not been fully introduced in *in-vivo* measurements yet. First of all because they usually require an accurate knowledge of the superficial layer thickness on an individual basis to actually improve the results and this is not an information easily obtained. In addition, some of them require multi-distance measurements, increasing the complexity of the instruments and probes.

The list of issues provided above has been keeping (and will keep) the diffuse optical community busy enough to improve precision and accuracy of brain haemodynamics measured by diffuse optics to reach the degree of reliability needed for clinical application. However we must remind that the small and medium sized clinical studies running all over the world employing the cutting-edge diffuse optical neuro-monitor are providing positive and valuable results. These technologies are (currently) the only and best option to provide continuous and non-invasive monitoring of the brain supply and consumption of oxygen at the cot- or bed-side. For this reason, clinical research should run in parallel with technological progress, with the design of more clinical studies in more clinical centers. These should have the objectives to, first, define reference clinical values and, hence, guidelines for maintaining those in each patient. This is specifically true for application in neonatal intensive care. Once more information on each preterm or critically-ill infant brain is given by shedding light on the head of each of them, a new path for clinical intervention can be laid. We could therefore discover whether clinical care guided by near-infrared photons traveling in neonatal brain could significantly improve the outcome of infants born preterm or critically-ill.

Bibliography

[1] Aanerud, J., Borghammer, P., Mallar Chakravarty, M., Vang, K., Rodell, A. B., Jónsdottir, K. Y., Møller, A., Ashkanian, M., Vafaee, M. S., Iversen, P., Johannsen, P., and Gjedde, A. Brain energy metabolism and blood flow differences in healthy aging. *J. Cereb. Blood Flow Metab. 32*, 7 (2012), 1177–1187.

[2] Accornero, N., Capozza, M., Pieroni, L., Pro, S., Davi, L., and Mecarelli, O. EEG mean frequency changes in healthy subjects during prefrontal transcranial direct current stimulation. *J. Neurophysiol. 112*, 6 (2014), 1367–1375.

[3] Almaazmi, M., Schmid, M. B., Havers, S., Reister, F., Lindner, W., Mayer, B., Hummler, H. D., and Fuchs, H. Cerebral near-infrared spectroscopy during transition of healthy term newborns. *Neonatology 103*, 4 (2013), 246–251.

[4] Andersen, J. B. *Neonatal Imaging of Cerebral Blood Flow with Positron Emission Tomography and Arterial Spin Labeling Magnetic Resonance.* PhD thesis, University of Copenhagen, 2015.

[5] Andersen, J. B., Henning, W. S., Lindberg, U., Ladefoged, C. N., Højgaard, L., Greisen, G., and Law, I. Positron emission tomography/magnetic resonance hybrid scanner imaging of cerebral

blood flow using 15O-water positron emission tomography and arterial spin labeling magnetic resonance imaging in newborn piglets. *J. Cereb. Blood Flow Metab. 35*, 11 (2015), 1703–1710.

[6] Andersen, J. B., Lindberg, U., Olesen, O. V., Benoit, D., Ladefoged, C. N., Larsson, H. B., Højgaard, L., Greisen, G., and Law, I. Hybrid PET/MRI imaging in healthy unsedated newborn infants with quantitative rCBF measurements using 15O-water PET. *J. Cereb. Blood Flow Metab.* (2018), 271678X17751835.

[7] Andrews, S. C., Hoy, K. E., Enticott, P. G., Daskalakis, Z. J., and Fitzgerald, P. B. Improving working memory: The effect of combining cognitive activity and anodal transcranial direct current stimulation to the left dorsolateral prefrontal cortex. *Brain Stimul. 4*, 2 (2011), 84–89.

[8] Antal, A., Alekseichuk, I., Bikson, M., Brockmöller, J., Brunoni, A. R., Chen, R., Cohen, L. G., Dowthwaite, G., Ellrich, J., Flöel, A., Fregni, F., George, M. S., Hamilton, R., Haueisen, J., Herrmann, C. S., Hummel, F. C., Lefaucheur, J. P., Liebetanz, D., Loo, C. K., McCaig, C. D., Miniussi, C., Miranda, P. C., Moliadze, V., Nitsche, M. A., Nowak, R., Padberg, F., Pascual-Leone, A., Poppendieck, W., Priori, A., Rossi, S., Rossini, P. M., Rothwell, J., Rueger, M. A., Ruffini, G., Schellhorn, K., Siebner, H. R., Ugawa, Y., Wexler, A., Ziemann, U., Hallett, M., and Paulus, W. Low intensity transcranial electric stimulation: Safety, ethical, legal regulatory and application guidelines. *Clin. Neurophysiol. 128*, 9 (2017), 1774–1809.

[9] Arribas-Gil, A., and Romo, J. Shape outlier detection and visualization for functional data: the outliergram. *Biostatistics 15*, 4 (2014), 603–619.

[10] Baenziger, O., Jaggi, J. L., Mueller, A. C., Morales, C. G., Lipp, A. E., Duc, G., and Bucher, H. U. Regional differences of cerebral blood flow in the preterm infant. *Eur. J. Pediatr. 154* (1995), 919–924.

[11] Baik, N., Urlesberger, B., Schwaberger, B., Schmölzer, G. M., Mileder, L., Avian, A., and Pichler, G. Reference Ranges for Cerebral Tissue Oxygen Saturation Index in Term Neonates during Immediate Neonatal Transition after Birth. *Neonatology 108*, 4 (2015), 283–286.

[12] Bailey, S. M., Hendricks-Munoz, K. D., and Mally, P. Cerebral, renal, and splanchnic tissue oxygen saturation values in healthy term newborns. *Am. J. Perinatol. 31*, 4 (2014), 339–344.

[13] Baker, W. B., Parthasarathy, A. B., Ko, T. S., Busch, D. R., Abramson, K., Tzeng, S.-y., Mesquita, R. C., Durduran, T., Greenberg, J. H., Kung, D. K., and Yodh, A. G. Pressure modulation algorithm to separate cerebral hemodynamic signals from extracerebral artifacts. *Neurophotonics 2*, 3 (2015), 035004.

[14] Basar, E., Basar-Eroglu, C., Karakas, S., and Schuermann, M. Are cognitive processes manifested in event-related gamma, alpha, theta and delta oscillations in the EEG? *Neurosci. Lett. 259*, 3 (1999), 165–168.

[15] Bates, D., Mächler, M., Bolker, B., and Walker, S. Fitting Linear Mixed-Effects Models Using lme4. *J. Stat. Softw. 67*, 1 (2015), 1–48.

[16] Becker, W. *Advanced Time-Correlated Single Photon Counting Techniques*, vol. 81 of *Springer Series in Chemical Physics*. Springer Berlin Heidelberg, Berlin, Heidelberg, 2005.

[17] Bergmann, T. O., Karabanov, A., Hartwigsen, G., Thielscher, A., and Siebner, H. R. Combining non-invasive transcranial brain stimulation with neuroimaging and electrophysiology: Current approaches and future perspectives. *Neuroimage 140* (2016), 4–19.

[18] Bernal, N. P., Hoffman, G. M., Ghanayem, N. S., and Arca, M. J. Cerebral and somatic near-infrared spectroscopy in normal newborns. *J. Pediatr. Surg. 45*, 6 (2010), 1306–1310.

[19] Boas, D. A. *Diffuse photon probes of structural and dynamical properties of turbid media: theory and biomedical applications.* PhD thesis, University of Pennsylvania, 1996.

[20] Boas, D. A., Campbell, L. E., and Yodh, A. G. Scattering and imaging with diffuse temporal field correlation. *Phys. Rev. Lett. 75*, 9 (1995), 1855–1858.

[21] Boas, D. a., and Franceschini, M. a. Haemoglobin oxygen saturation as a biomarker: the problem and a solution. *Philos. Trans. R. Soc. A Math. Phys. Eng. Sci. 369*, 1955 (2011), 4407–4424.

[22] Boas, D. A., Sakadžic, S., Selb, J., Farzam, P., Franceschini, M. A., and Carp, S. A. Establishing the diffuse correlation spectroscopy signal relationship with blood flow. *Neurophotonics 3*, 3 (jun 2016), 031412.

[23] Boas, D. A., and Yodh, A. G. Spatially varying dynamical properties of turbid media probed with diffusing temporal light correlation. *J. Opt. Soc. Am. A 14*, 1 (jan 1997), 192.

[24] Boggio, P. S., Bermpohl, F., Vergara, A. O., Muniz, A. L. C. R., Nahas, F. H., Leme, P. B., Rigonatti, S. P., and Fregni, F. Go-no-go task performance improvement after anodal transcranial DC

stimulation of the left dorsolateral prefrontal cortex in major depression. *J. Affect. Disord. 101*, 1-3 (2007), 91–98.

[25] Brew, N., Walker, D., and Wong, F. Y. Cerebral vascular regulation and brain injury in preterm infants. *Am. J. Physiol. Regul. Integr. Comp. Physiol. 306*, 11 (jun 2014), R773–86.

[26] Brigadoi, S., and Cooper, R. J. How short is short? Optimum sourcedetector distance for short-separation channels in functional near-infrared spectroscopy. *Neurophotonics 2*, 2 (2015), 025005.

[27] Brunoni, A. R., Nitsche, M. a., Bolognini, N., Bikson, M., Wagner, T., Merabet, L., Edwards, D. J., Valero-Cabre, A., Rotenberg, A., Pascual-Leone, A., Ferrucci, R., Priori, A., Boggio, P. S., and Fregni, F. Clinical research with transcranial direct current stimulation (tDCS): challenges and future directions. *Brain Stimul. 5*, 3 (2012), 175–95.

[28] Calamante, F., Thomas, D. L., Pell, G. S., Wiersma, J., and Turner, R. Measuring Cerebral Blood Flow Using Magnetic Resonance Imaging Techniques. *J. Cereb. Blood Flow Metab. 19*, 7 (1999), 701–735.

[29] Carp, S. A., Farzam, P., Redes, N., Hueber, D. M., and Franceschini, M. A. Combined multi-distance frequency domain and diffuse correlation spectroscopy system with simultaneous data acquisition and real-time analysis. *Biomed. Opt. Express 8*, 9 (2017), 3993.

[30] Carstensen, B. Replicate measurements. In *Comp. Clin. Meas. Methods*. John Wiley & Sons, Ltd, Chichester, UK, aug 2010, ch. 5.

[31] Clark, V. P., and Parasuraman, R. Neuroenhancement: Enhancing brain and mind in health and in disease. *Neuroimage 85* (2014), 889–894.

[32] Coffman, B. A., Clark, V. P., and Parasuraman, R. Battery powered thought: Enhancement of attention, learning, and memory in healthy adults using transcranial direct current stimulation. *Neuroimage 85* (2014), 895–908.

[33] Contini, D., Martelli, F., and Zaccanti, G. Photon migration through a turbid slab described by a model based on diffusion approximation. I. Theory. *Appl. Opt. 36*, 19 (1997), 4587–4599.

[34] Cortese, L., Presti, G. L., Pagliazzi, M., Contini, D., Mora, A. D., Pifferi, A., Sekar, S. K. V., Spinelli, L., Taroni, P., Zanoletti, M., Weigel, U. M., de Fraguier, S., Nguyen-Dihn, A., Rosinski, B., and Durduran, T. Liquid phantoms for near-infrared and diffuse correlation spectroscopies with tunable optical and dynamic properties. *Biomed. Opt. Express 9*, 5 (may 2018), 2068.

[35] Cubeddu, R., Pifferi, A., Taroni, P., Torricelli, A., and Valentini, G. Experimental test of theoretical models for time-resolved reflectance. *Med. Phys. 23*, 9 (sep 1996), 1625–1633.

[36] Cuevas, A., Febrero, M., and Fraiman, R. On the use of the bootstrap for estimating functions with functional data. *Comput. Stat. Data Anal. 51*, 2 (2006), 1063–1074.

[37] Culver, J. P., Durduran, T., Furuya, D., Cheung, C., Greenberg, J. H., and Yodh, A. G. Diffuse optical tomography of cerebral blood flow, oxygenation, and metabolism in rat during focal ischemia. *J Cereb Blood Flow Metab 23*, 8 (2003), 911–924.

[38] Dawson, J. A., Kamlin, C. O. F., Vento, M., Wong, C., Cole, T. J., Donath, S. M., Davis, P. G., and Morley, C. J. Defining the Reference Range for Oxygen Saturation for Infants After Birth. *Pediatrics 125*, 6 (2010), e1340–e1347.

[39] De Carli, A., Andresen, B., Giovannella, M., Durduran, T., Contini, D., Spinelli, L., Weigel, U. M., Passera, S., Pesenti, N., Mosca, F., Torricelli, A., Fumagalli, M., and Greisen, G. Cerebral oxygenation and blood flow in term infants during postnatal transition: the BabyLux project. *ADC Fetal Neonatal Ed. accepted* (2019).

[40] Dehaes, M., Cheng, H. H., Buckley, E. M., Lin, P.-Y., Ferradal, S., Williams, K., Vyas, R., Hagan, K., Wigmore, D., McDavitt, E., Soul, J. S., Franceschini, M. A., Newburger, J. W., and Ellen Grant, P. Perioperative cerebral hemodynamics and oxygen metabolism in neonates with single-ventricle physiology. *Biomed. Opt. Express 6*, 12 (2015), 4749.

[41] Delpy, D. T., and Cope, M. Quantification in tissue near-infrared spectroscopy. *Philos. Trans. R. Soc. London. Ser. B Biol. Sci. 352*, 1354 (jun 1997), 649–659.

[42] Demel, A., Feilke, K., Schöning, M., Wolf, M., Poets, C. F., and Franz, A. R. Healthy term and moderately preterm infants have similar cerebral oxygen saturation and cerebral blood flow volumes during early post-natal transition. *Acta Paediatr. Int. J. Paediatr. 104*, 8 (2015), e330–e336.

[43] Demel, A., Feilke, K., Wolf, M., Poets, C. F., and Franz, A. R. Correlation between skin, bone, and cerebrospinal fluid layer thickness and optical coefficients measured by multidistance frequency-domain near-infrared spectroscopy in term and preterm infants. *J. Biomed. Opt. 19*, 1 (2014), 017004.

[44] Dempsey, L. A., Persad, M., Powell, S., Chitnis, D., and Hebden, J. C. Geometrically complex 3D-printed phantoms for diffuse optical imaging. *Biomed. Opt. Express 8*, 3 (mar 2017), 1754.

[45] Diop, M., Verdecchia, K., Lee, T.-Y., and St Lawrence, K. Calibration of diffuse correlation spectroscopy with a time-resolved near-infrared technique to yield absolute cerebral blood flow measurements. *Biomed. Opt. Express 3*, 6 (2012), 1476.

[46] Dobbing, J., and Sands, J. Quantitative growth and development of human brain. *Arch. Dis. Child. 48*, 10 (1973), 757–767.

[47] Dockery, C. A., Hueckel-Weng, R., Birbaumer, N., and Plewnia, C. Enhancement of Planning Ability by Transcranial Direct Current Stimulation. *J. Neurosci. 29*, 22 (2009), 7271–7277.

[48] Dong, L., He, L., Lin, Y., Shang, Y., and Yu, G. Simultaneously extracting multiple parameters via fitting one single autocorrelation function curve in diffuse correlation spectroscopy. *IEEE Trans. Biomed. Eng. 60*, 2 (2013), 361–368.

[49] Drayton, M., and Skidmore, R. Doppler ultrasound in the neonate. *Ultrasound Med. Biol. 12*, 10 (oct 1986), 761–772.

[50] Dullenkopf, A., Frey, B., Baenziger, O., Gerber, A., and Weiss, M. Measurement of cerebral oxygenation state in anaesthetized children using the INVOS 5100 cerebral oximeter. *Paediatr. Anaesth. 13*, 5 (2003), 384–391.

[51] Duncan, A., Meek, J. H., Clemence, M., Elwell, C. E., Tyszczuk, L., Cope, M., and Delpy, D. T. Optical pathlength measurements on adult head, calf and forearm and the head of the newborn infant using phase resolved optical spectroscopy. Tech. Rep. 2, 1995.

[52] Durduran, T., Choe, R., Baker, W. B., and Yodh, a. G. Diffuse optics for tissue monitoring and tomography. *Reports Prog. Phys. 73*, 7 (2010), 076701.

[53] Durduran, T., and Yodh, A. G. Diffuse correlation spectroscopy for non-invasive, micro-vascular cerebral blood flow measurement. *Neuroimage 85* (2014), 51–63.

[54] Durduran, T., Yodh, A. G., Chance, B., and Boas, D. A. Does the photon-diffusion coefficient depend on absorption? *J. Opt. Soc. Am. A 14*, 12 (1997), 3358.

[55] Einstein, A. *Investigations on the Theory of the Brownian Movement.* Dover Publications, 1956.

[56] Elmer, S., Burkard, M., Renz, B., Meyer, M., and Jancke, L. Direct current induced short-term modulation of the left dorsolateral prefrontal cortex while learning auditory presented nouns. *Behav. Brain Funct. 5*, 1 (2009), 29.

[57] Engel, A. K., and Fries, P. Beta-band oscillations-signalling the status quo? *Curr. Opin. Neurobiol. 20*, 2 (2010), 156–165.

[58] Ezquerro, F., Moffa, A. H., Bikson, M., Khadka, N., Aparicio, L. V., de Sampaio-Junior, B., Fregni, F., Bensenor, I. M., Lotufo, P. A., Pereira, A. C., and Brunoni, A. R. The Influence of Skin Redness on Blinding in Transcranial Direct Current Stimulation Studies: A Crossover Trial. *Neuromodulation 20*, 3 (2017), 248–255.

[59] Farrell, T. J., Patterson, M. S., and Wilson, B. A diffusion theory model of spatially resolved, steady-state diffuse reflectance for the noninvasive determination of tissue optical properties in vivo. *Med. Phys. 19*, 4 (jul 1992), 879–888.

[60] Farzam, P., Buckley, E., Lin, P., Grant, E., Inder, T., Carp, S., and Franceschini, M. Shedding light on the neonatal brain: probing cerebral hemodynamics by diffuse optical spectroscopic methods. *Sci. Rep.*, November (2017), 1–10.

[61] Farzam, P., and Durduran, T. Multidistance diffuse correlation spectroscopy for simultaneous estimation of absolute scattering and absorption coefficient and the blood flow index. *J. Biomed. Opt. 20*, 5 (2015), 55001.

[62] Fauchère, J. C., Schulz, G., Haensse, D., Keller, E., Ersch, J., Bucher, H. U., and Wolf, M. Near-Infrared Spectroscopy Measurements of Cerebral Oxygenation in Newborns during Immediate Postnatal Adaptation. *J. Pediatr. 156*, 3 (2010), 372–376.

[63] Febrero, M., Galeano, P., and González-Manteiga, W. Outlier detection in functional data by depth measures, with application to identify abnormal NOx levels. *Environmetrics 19*, 4 (2008), 331–345.

[64] Febrero-Bande, M., and Oviedo de la Fuente, M. Statistical computing in functional data analysis: the R package fda. usc. *J. Stat. Softw. 51*, 4 (2012), 1–28.

[65] Ferrucci, R., Mameli, F., and Guidi, I. Transcranial direct current stimulation improves recognition memory in Alzheimer disease. *Neurology 71* (2008), 493–498.

[66] Fiori, V., Coccia, M., Marinelli, C. V., Vecchi, V., Bonifazi, S., Ceravolo, M. G., Provinciali, L., Tomaiuolo, F., and Marangolo, P. Transcranial Direct Current Stimulation Improves Word Retrieval in Healthy and Nonfluent Aphasic Subjects. *J. Cogn. Neurosci. 23*, 9 (2011), 2309–2323.

[67] Fregni, F., Boggio, P. S., Nitsche, M., Bermpohl, F., Antal, A., Feredoes, E., Marcolin, M. A., Rigonatti, S. P., Silva, M. T. A., Paulus, W., and Pascual-Leone, A. Anodal transcranial direct current stimulation of prefrontal cortex enhances working memory. *Exp. Brain Res. 166*, 1 (2005), 23–30.

[68] Fregni, F., and Pascual-Leone, A. Technology Insight: noninvasive brain stimulation in neurology perspectives on the therapeutic potential of rTMS and tDCS. *Nat. Clin. Pract. Neurol. 3*, 7 (2007), 383–393.

[69] Fujisaka, S.-i., Ozaki, T., Suzuki, T., Kamada, T., Kitazawa, K., Nishizawa, M., Takahashi, A., and Suzuki, S. A Clinical Tissue Oximeter Using NIR Time-Resolved Spectroscopy. 2016, pp. 427–433.

[70] Gagnon, L., Desjardins, M., Jehanne-Lacasse, J., Bherer, L., and Lesage, F. Investigation of diffuse correlation spectroscopy in multi-layered media including the human head. *Opt. Express 16*, 20 (2008), 15514–15530.

[71] George, M. S., and Aston-Jones, G. Noninvasive techniques for probing neurocircuitry and treating illness: vagus nerve stimulation (VNS), transcranial magnetic stimulation (TMS) and transcranial direct current stimulation (tDCS). *Neuropsychopharmacology 35*, 1 (2010), 301–316.

[72] Giusto, A., D'andrea, C., Spinelli, L., Contini, D., Torricelli, A., Martelli, F., Zaccanti, G., and Cubeddu, R. Monitoring absorption changes in a layered diffusive medium by white-light time-resolved reflectance spectroscopy. *IEEE Trans. Instrum. Meas. 59*, 7 (2010), 1925–1932.

[73] Gladwin, T. E., den Uyl, T. E., Fregni, F. F., and Wiers, R. W. Enhancement of selective attention by tDCS: Interaction with interference in a Sternberg task. *Neurosci. Lett. 512*, 1 (2012), 33–37.

[74] Goodman, J. W. Some fundamental properties of speckle*. *J. Opt. Soc. Am. 66*, 11 (nov 1976), 1145.

[75] Grech, R., Cassar, T., Muscat, J., Camilleri, K. P., Fabri, S. G., Zervakis, M., Xanthopoulos, P., Sakkalis, V., and Van-

RUMSTE, B. Review on solving the inverse problem in EEG source analysis. *J. Neuroeng. Rehabil. 5*, 1 (2008), 25.

[76] GREISEN, G. Autoregulation of cerebral blood flow in newborn babies. *Early Hum. Dev. 81*, 5 (may 2005), 423–8.

[77] GREISEN, G. Methods to Assess Systemic and Organ Blood Flow in the Neonate. In *Hemodynamics Cardiol. Neonatol. Quest. Controv.*, C. S. Kleinman and I. Seri, Eds., second ed. Elsevier, 2012, ch. 4, pp. 81–94.

[78] GREISEN, G., ANDRESEN, B., PLOMGAARD, A. M., AND HYTTEL-SØRENSEN, S. Cerebral oximetry in preterm infants: an agenda for research with a clear clinical goal. *Neurophotonics 3*, 3 (2016), 031407.

[79] GREISEN, G., LEUNG, T., AND WOLF, M. Has the time come to use near-infrared spectroscopy as a routine clinical tool in preterm infants undergoing intensive care? *Philos. Trans. A. Math. Phys. Eng. Sci. 369*, 1955 (nov 2011), 4440–51.

[80] GREISEN, G., AND TROJABORG, W. Cerebral blood flow, PaCO2 changes, and visual evoked potentials in mechanically ventilated, preterm infants. *Acta Paediatr. Scand. 76*, 3 (1987), 394–400.

[81] GUARIENTI, F., CAUMO, W., SHIOZAWA, P., CORDEIRO, Q., BOGGIO, P. S., BENSEÑOR, I. M., LOTUFO, P. A., BIKSON, M., AND BRUNONI, A. R. Reducing Transcranial Direct Current Stimulation-Induced Erythema With Skin Pretreatment: Considerations for Sham-Controlled Clinical Trials. *Neuromodulation 18*, 4 (2015), 261–265.

[82] HAN, C.-H., SONG, H., KANG, Y.-G., KIM, B.-M., AND IM, C.-H. Hemodynamic responses in rat brain during transcranial direct current stimulation: a functional near-infrared spectroscopy study. *Biomed. Opt. Express 5*, 6 (2014), 1812.

[83] Harmony, T., Fernández, T., Silva, J., Bernal, J., Díaz-Comas, L., Reyes, A., Marosi, E., Rodríguez, M., and Rodríguez, M. EEG delta activity: An indicator of attention to internal processing during performance of mental tasks. *Int. J. Psychophysiol. 24*, 1-2 (1996), 161–171.

[84] Haskell, R. C., Svaasand, L. O., Tsay, T.-T., Feng, T.-C., Tromberg, B. J., and McAdams, M. S. Boundary conditions for the diffusion equation in radiative transfer. *J. Opt. Soc. Am. A 11*, 10 (oct 1994), 2727.

[85] He, L., Baker, W., Milej, D., Kavuri, V., Busch, D., Diop, M., Lawrence, K., Balu, R., Andrew Kofke, W., and Yodh, A. Noninvasive continuous optical monitoring of absolute cerebral blood flow in critically ill adults. *Neurophotonics 5*, 04 (nov 2018), 1.

[86] Henriksen, O. M., Larsson, H. B. W., Hansen, A. E., Grüner, J. M., Law, I., and Rostrup, E. Estimation of intersubject variability of cerebral blood flow measurements using MRI and positron emission tomography. *J. Magn. Reson. Imaging 35*, 6 (2012), 1290–1299.

[87] Herscovitch, P., Markham, J., and Raichle, M. E. Brain blood flow measured with intravenous H2(15)O. I. Theory and error analysis. *J. Nucl. Med. 24*, 9 (sep 1983), 782–9.

[88] Hessel, T. W., Hyttel-Sorensen, S., and Greisen, G. Cerebral oxygenation after birth - a comparison of INVOS(®) and FORE-SIGHT near-infrared spectroscopy oximeters. *Acta Paediatr. 103*, 5 (2014), 488–493.

[89] Holland, B. a., Haas, D. K., Norman, D., Brant-Zawadzki, M., and Newton, T. H. MRI of normal brain maturation. *AJNR. Am. J. Neuroradiol. 7*, 2 (1986), 201–208.

[90] Hong, I. K., Chung, S. T., Kim, H. K., Kim, Y. B., Son, Y. D., and Cho, Z. H. Ultra fast symmetry and SIMD-based projection-backprojection (SSP) algorithm for 3-D PET image reconstruction. *IEEE Trans. Med. Imaging 26*, 6 (2007), 789–803.

[91] Horvath, J. C., Forte, J. D., and Carter, O. Evidence that transcranial direct current stimulation (tDCS) generates little-to-no reliable neurophysiologic effect beyond MEP amplitude modulation in healthy human subjects: A systematic review. *Neuropsychologia 66* (2015), 213–236.

[92] Horwitz, B., and Poeppel, D. How can EEG/MEG and fMRI/PET data be combined? *Hum. Brain Mapp. 17*, 1 (2002), 1–3.

[93] Hoshi, Y. Functional near-infrared optical imaging: Utility and limitations in human brain mapping. *Psychophysiology 40*, 4 (2003), 511–520.

[94] Hunter, M. A., Coffman, B. A., Trumbo, M. C., and Clark, V. P. Tracking the neuroplastic changes associated with transcranial direct current stimulation: a push for multimodal imaging. *Front. Hum. Neurosci. 7*, August (2013), 495.

[95] Hyttel-Sorensen, S., Hessel, T. W., la Cour, A., and Greisen, G. A comparison between two NIRS oximeters (INVOS, OxyPrem) using measurement on the arm of adults and head of infants after caesarean section. *Biomed. Opt. Express 5*, 10 (2014), 3671.

[96] Hyttel-Sorensen, S., Pellicer, A., Alderliesten, T., Austin, T., van Bel, F., Benders, M., Claris, O., Dempsey, E., Franz, A. R., Fumagalli, M., Gluud, C., Grevstad, B., Hagmann, C., Lemmers, P., van Oeveren, W., Pichler, G., Plomgaard, A. M., Riera, J., Sanchez, L., Winkel, P., Wolf, M., and Greisen, G. Cerebral near infrared spectroscopy oximetry in extremely preterm

infants: phase II randomised clinical trial. *BMJ 350*, jan05 2 (2015), g7635–g7635.

[97] Hyttel-Sorensen, S., Sorensen, L. C., Riera, J., and Greisen, G. Tissue oximetry : a comparison of mean values of regional tissue saturation , reproducibility and dynamic range of four NIRS-instruments on the human forearm. 1743–1753.

[98] Ijichi, S., Kusaka, T., Isobe, K., Okubo, K., Kawada, K., Namba, M., Okada, H., Nishida, T., Imai, T., and Itoh, S. Developmental changes of optical properties in neonates determined by near-infrared time-resolved spectroscopy. *Pediatr. Res. 58*, 3 (sep 2005), 568–73.

[99] Irestedt, L., Lagercrantz, H., Hjemdahl, P., Hagnevik, K., and Belfrage, P. Fetal and maternal plasma catecholamine levels at elective cesarean section under general or epidural anesthesia versus vaginal delivery. *Am. J. Obstet. Gynecol. 142*, 8 (1982), 1004–1010.

[100] Irwin, D., Dong, L., Shang, Y., Cheng, R., Kudrimoti, M., Stevens, S. D., and Yu, G. Influences of tissue absorption and scattering on diffuse correlation spectroscopy blood flow measurements. *Biomed. Opt. Express 2*, 7 (2011), 1969–1985.

[101] Ishikuro, K., Urakawa, S., Takamoto, K., Ishikawa, A., Ono, T., and Nishijo, H. Cerebral functional imaging using near-infrared spectroscopy during repeated performances of motor rehabilitation tasks tested on healthy subjects. *Front Hum Neurosci 8*, May (2014), 292.

[102] Isobe, K., Kusaka, T., Fujikawa, Y., Okubo, K., Nagano, K., Yasuda, S., Kondo, M., Itoh, S., Hirao, K., and Onishi, S. Measurement of cerebral oxygenation in neonates after vaginal delivery and

cesarean section using full-spectrum near infrared spectroscopy. *Comp. Biochem. Physiol. - A Mol. Integr. Physiol. 132*, 1 (2002), 133–138.

[103] Iwamoto, H. S., Teitel, D., and Rudolph, A. M. Effects of birth-related events on blood flow distribution. *Pediatr. Res. 22*, 6 (1987), 634–640.

[104] Jacobson, L., Ezra, A., Berger, U., and Lavidor, M. Modulating oscillatory brain activity correlates of behavioral inhibition using transcranial direct current stimulation. *Clin. Neurophysiol. 123*, 5 (2012), 979–984.

[105] Jacques, S. L., and Pogue, B. W. Tutorial on diffuse light transport. *J. Biomed. Opt. 13*, 4 (2008), 041302.

[106] Jain, V., Buckley, E. M., Licht, D. J., Lynch, J. M., Schwab, P. J., Naim, M. Y., Lavin, N. a., Nicolson, S. C., Montenegro, L. M., Yodh, A. G., and Wehrli, F. W. Cerebral oxygen metabolism in neonates with congenital heart disease quantified by MRI and optics. *J. Cereb. Blood Flow Metab. 34*, 3 (2014), 380–388.

[107] Javadi, A. H., and Walsh, V. Transcranial direct current stimulation (tDCS) of the left dorsolateral prefrontal cortex modulates declarative memory. *Brain Stimul. 5*, 3 (2012), 231–241.

[108] Jelzow, A., Wabnitz, H., Tachtsidis, I., Kirilina, E., Brühl, R., and Macdonald, R. Separation of superficial and cerebral hemodynamics using a single distance time-domain NIRS measurement. *Biomed. Opt. Express 5*, 5 (2014), 1465–82.

[109] Jindal, U., Sood, M., Dutta, A., and Chowdhury, S. R. Development of Point of Care Testing Device for Neurovascular Coupling From Simultaneous Recording of EEG and NIRS During Anodal Transcranial

Direct Current Stimulation. *IEEE J. Transl. Eng. Heal. Med. 3* (2015), 1–12.

[110] Jobsis, F. Noninvasive, infrared monitoring of cerebral and myocardial oxygen sufficiency and circulatory parameters. *Science (80-.). 198*, 4323 (dec 1977), 1264–1267.

[111] Jones, K. T., Gözenman, F., and Berryhill, M. E. The strategy and motivational influences on the beneficial effect of neurostimulation: A tDCS and fNIRS study. *Neuroimage 105* (2015), 238–247.

[112] Jurcak, V., Tsuzuki, D., and Dan, I. 10/20, 10/10, and 10/5 systems revisited: Their validity as relative head-surface-based positioning systems. *Neuroimage 34*, 4 (2007), 1600–1611.

[113] Keeser, D., Padberg, F., Reisinger, E., Pogarell, O., Kirsch, V., Palm, U., Karch, S., Möller, H. J., Nitsche, M. A., and Mulert, C. Prefrontal direct current stimulation modulates resting EEG and event-related potentials in healthy subjects: A standardized low resolution tomography (sLORETA) study. *Neuroimage 55*, 2 (2011), 644–657.

[114] Keller, S. H., Svarer, C., and Sibomana, M. Attenuation correction for the HRRT PET-scanner using transmission scatter correction and total variation regularization. *IEEE Trans. Med. Imaging 32*, 9 (2013), 1611–1621.

[115] Kety, S. S., and Schmidt, C. F. The effects of altered arterial tensions of carbon dioxide and oxygen on cerebral blood flow and oxygen consumption of normal young men. *J. Clin. Invest. 27*, 4 (1948), 484–492.

[116] Khadka, N., Zannou, A. L., Zunara, F., Truong, D. Q., Dmochowski, J., and Bikson, M. Minimal Heating at the Skin Surface

During Transcranial Direct Current Stimulation. *Neuromodulation Technol. Neural Interface* (jan 2017).

[117] Khan, B., Hodics, T., Hervey, N., Kondraske, G., Stowe, A., and Alexandrakis, G. Enhancing motor performance improvement by personalizing non-invasive cortical stimulation with concurrent functional near-infrared spectroscopy and multi-modal motor measurements. In *Opt. Tech. Neurosurgery, Neurophotonics, Optogenetics II* (2015), H. Hirschberg, S. J. Madsen, E. D. Jansen, Q. Luo, S. K. Mohanty, and N. V. Thakor, Eds., vol. 9305, p. 93051A.

[118] Khan, B., Hodics, T., Hervey, N., Kondraske, G., Stowe, A. M., and Alexandrakis, G. Functional near-infrared spectroscopy maps cortical plasticity underlying altered motor performance induced by transcranial direct current stimulation. *J. Biomed. Opt. 18*, 11 (2013), 116003.

[119] Kilner, J. M., Mattout, J., Henson, R., and Friston, K. J. Hemodynamic correlates of EEG: A heuristic. *Neuroimage 28*, 1 (2005), 280–286.

[120] Kim, J. G., and Liu, H. Investigation of biphasic tumor oxygen dynamics induced by hyperoxic gas intervention: the dynamic phantom approach. *Appl. Opt. 47*, 2 (2008), 242–52.

[121] Kincses, T. Z., Antal, A., Nitsche, M. A., Bártfai, O., and Paulus, W. Facilitation of probabilistic classification learning by transcranial direct current stimulation of the prefrontal cortex in the human. *Neuropsychologia 42*, 1 (2004), 113–117.

[122] Kleiser, S., Ostojic, D., Andresen, B., Nasseri, N., Isler, H., Scholkmann, F., Karen, T., Greisen, G., and Wolf, M. Com-

parison of tissue oximeters on a liquid phantom with adjustable optical properties: an extension. *Biomed. Opt. Express 9*, 1 (2018), 86.

[123] Kleiser, S., Ostojic, D., and Nasseri, N. In vivo precision assessment of a near-infrared spectroscopy-based tissue oximeter (OxyPrem v1.3) in neonates considering systemic hemodynamic fluctuations. *J. Biomed. Opt. 23*, 06 (jun 2018), 1.

[124] Klimesch, W. EEG alpha and theta oscillations reflect cognitive and memory performance: A review and analysis. *Brain Res. Rev. 29*, 2-3 (1999), 169–195.

[125] Kretschmann, H. J., Kammradt, G., Krauthausen, I., Sauer, B., and Wingert, F. *Brain growth in man.* No. 28. 1986.

[126] Laakso, I., Tanaka, S., Mikkonen, M., Koyama, S., Sadato, N., and Hirata, A. Electric fields of motor and frontal tDCS in a standard brain space: A computer simulation study. *Neuroimage 137* (2016), 140–151.

[127] Lang, N., Nitsche, M. a., Paulus, W., Rothwell, J. C., and Lemon, R. N. Effects of transcranial direct current stimulation over the human motor cortex on corticospinal and transcallosal excitability. *Exp. Brain Res. 156*, 4 (2004), 439–443.

[128] Lang, N., Siebner, H. R., Ward, N. S., Lee, L., Nitsche, M. a., Paulus, W., Rothwell, J. C., Lemon, R. N., and Frackowiak, R. S. How does transcranial DC stimulation of the primary motor cortex alter regional neuronal activity in the human brain? *Eur. J. Neurosci. 22*, 2 (2005), 495–504.

[129] Lareau, E., Lesage, F., Pouliot, P., Nguyen, D., Le Lan, J., and Sawan, M. Multichannel wearable system dedicated for simulta-

neous electroencephalography near-infrared spectroscopy real-time data acquisitions. *J. Biomed. Opt. 16*, 9 (2011), 096014.

[130] Lassen, N. A., Friberg, L., Kastrup, J., Rizzi, D., and Jensen, J. J. Effects of acetazolamide on cerebral blood flow and brain tissue oxygenation. *Postgr. Med J 63*, 737 (1987), 185–187.

[131] Lefaucheur, J.-p., Antal, A., Ayache, S. S., Benninger, D. H., Brunelin, J., Cogiamanian, F., Cotelli, M., De Ridder, D., Ferrucci, R., Langguth, B., Marangolo, P., Mylius, V., Nitsche, M. A., Padberg, F., Palm, U., Poulet, E., Priori, A., Rossi, S., Schecklmann, M., Vanneste, S., Ziemann, U., Garcia-Larrea, L., and Paulus, W. Evidence-based guidelines on the therapeutic use of transcranial direct current stimulation (tDCS). *Clin. Neurophysiol. 128*, 1 (2017), 56–92.

[132] Lemieux, P. A., and Durian, D. J. Investigating non-Gaussian scattering processes by using nth-order intensity correlation functions. *J. Opt. Soc. Am. A 16*, 7 (1999), 1651–1664.

[133] Lenth, R. V. Least-Squares Means: The R Package lsmeans. *J. Stat. Softw. 69*, 1 (2016).

[134] Li, W., Weiyuan, Z., and Yanhui, Z. The study of maternal and fetal plasma catecholamines levels during pregnancy and delivery. *J. Perinat. Med. 27*, 3 (1999), 195–198.

[135] Liebert, A., Wabnitz, H., and Elster, C. Determination of absorption changes from moments of distributions of times of flight of photons: optimization of measurement conditions for a two-layered tissue model. *J. Biomed. Opt. 17*, 5 (may 2012), 57005.

[136] Liebert, A., Wabnitz, H., Grosenick, D., Möller, M., Macdonald, R., and Rinneberg, H. Evaluation of optical properties of

highly scattering media by moments of distributions of times of flight of photons. *Appl. Opt. 42*, 28 (2003), 5785–5792.

[137] Liebert, A., Wabnitz, H., Steinbrink, J., Obrig, H., Moeller, M., Macdonald, R., Villringer, A., and Rinneberg, H. Time-Resolved Multidistance Near-Infrared Spectroscopy of the Adult Head: Intracerebral and Extracerebral Absorption Changes from Moments of Distribution of Times of Flight of Photons. *Appl. Opt. 43*, 15 (2004), 3037.

[138] Liem, K. D., and Greisen, G. Monitoring of cerebral haemodynamics in newborn infants. *Early Hum. Dev. 86*, 3 (2010), 155–158.

[139] Lin, P.-Y., Roche-Labarbe, N., Dehaes, M., Fenoglio, A., Grant, P. E., and Franceschini, M. A. Regional and hemispheric asymmetries of cerebral hemodynamic and oxygen metabolism in newborns. *Cereb. Cortex 23*, 2 (feb 2013), 339–48.

[140] Lin, Y., He, L., Shang, Y., and Yu, G. Noncontact diffuse correlation spectroscopy for noninvasive deep tissue blood flow measurement. *J. Biomed. Opt. 17*, 1 (jan 2012), 010502.

[141] Linnet, K. Estimation of the linear relationship between the measurements of two methods with proportional errors. *Stat. Med. 9*, 12 (dec 1990), 1463–1473.

[142] Liu, L., Johnson, H. L., Cousens, S., Perin, J., Scott, S., Lawn, J. E., Rudan, I., Campbell, H., Cibulskis, R., Li, M., Mathers, C., and Black, R. E. Global, regional, and national causes of child mortality: An updated systematic analysis for 2010 with time trends since 2000. *Lancet 379*, 9832 (2012), 2151–2161.

[143] Logothetis, N. K. The neural basis of the blood-oxygen-level-dependent functional magnetic resonance imaging signal. *Philos. Trans. R. Soc. B Biol. Sci. 357*, 1424 (2002), 1003–1037.

[144] Magri, C., Schridde, U., Murayama, Y., Panzeri, S., and Logothetis, N. K. The Amplitude and Timing of the BOLD Signal Reflects the Relationship between Local Field Potential Power at Different Frequencies. *J. Neurosci. 32*, 4 (2012), 1395–1407.

[145] Manuilova, E., Schuetzenmeister, A., and Model, F. mcr package, 2015.

[146] March of Dimes, PMNCH, Save the Children, and WHO. *Born Too Soon - The Global Action Report on PretermBirth.* World Health Organization, Geneva, 2012.

[147] Martelli, F., Binzoni, T., Pifferi, A., Spinelli, L., Farina, A., and Torricelli, A. There's plenty of light at the bottom: statistics of photon penetration depth in random media. *Sci. Rep. 6*, 1 (jul 2016), 27057.

[148] Martelli, F., Del Bianco, S., Ismaelli, A., and Zaccanti, G. *Light Propagation through Biological Tissue.* SPIE, 2010.

[149] Matcher, S. J., Cope, M., and Delpy, D. T. Use of the water absorption spectrum to quantify tissue chromophore concentration changes in near infrared spectroscopy. *Phys. Med. Biol. 39* (1994), 177–196.

[150] McKendrick, R., Parasuraman, R., and Ayaz, H. Wearable functional near infrared spectroscopy (fNIRS) and transcranial direct current stimulation (tDCS): expanding vistas for neurocognitive augmentation. *Front. Syst. Neurosci. 9*, March (2015), 1–14.

[151] Merzagora, A. C., Foffani, G., Panyavin, I., Mordillo-Mateos, L., Aguilar, J., Onaral, B., and Oliviero, A. Prefrontal hemodynamic changes produced by anodal direct current stimulation. *Neuroimage 49*, 3 (2010), 2304–10.

[152] Meyer, E. Simultaneous correction for tracer arrival delay and dispersion in CBF measurements by the H215O autoradiographic method and dynamic PET. *J. Nucl. Med. 30*, 6 (1989), 1069–1078.

[153] Mourant, J. R., Fuselier, T., Boyer, J., Johnson, T. M., and Bigio, I. J. Predictions and measurements of scattering and absorption over broad wavelength ranges in tissue phantoms. *Appl. Opt. 36*, 4 (1997), 949–957.

[154] Muthalib, M., Re, R., Besson, P., Perrey, S., Rothwell, J., Contini, D., Spinelli, L., and Torricelli, a. Transcranial direct current stimulation induced modulation of cortical haemodynamics: A comparison between time-domain and continuous-wave functional near-infrared spectroscopy. *Brain Stimul. 8*, 2 (2015), 392–393.

[155] Nelson, J. T., McKinley, R. A., Golob, E. J., Warm, J. S., and Parasuraman, R. Enhancing vigilance in operators with prefrontal cortex transcranial direct current stimulation (tDCS). *Neuroimage 85* (2014), 909–917.

[156] Niemz, M. H. *Laser-Tissue Interactions*. Springer Berlin Heidelberg, Berlin, Heidelberg, 2002.

[157] Nilsson, A. M., Sturesson, C., Liu, D. L., and Andersson-Engels, S. Changes in spectral shape of tissue optical properties in conjunction with laser-induced thermotherapy. *Appl. Opt. 37*, 7 (1998), 1256–1267.

[158] Ninck, M., Untenberger, M., and Gisler, T. Diffusing-wave spectroscopy with dynamic contrast variation: disentangling the effects of blood flow and extravascular tissue shearing on signals from deep tissue. *Biomed. Opt. Express 1*, 5 (dec 2010), 1502.

[159] Nitsche, M. A., Boggio, P. S., Fregni, F., and Pascual-Leone, A. Treatment of depression with transcranial direct current stimulation (tDCS): A Review. *Exp. Neurol. 219*, 1 (2009), 14–19.

[160] Nitsche, M. A., and Paulus, W. Excitability changes induced in the human motor cortex by weak transcranial direct current stimulation. *J. Physiol. 527*, 3 (2000), 633–639.

[161] Noori, S., Stavroudis, T. A., and Seri, I. Systemic and Cerebral Hemodynamics During the Transitional Period After Premature Birth. *Clin. Perinatol. 36*, 4 (2009), 723–736.

[162] Noori, S., Stavroudis, T. A., and Seri, I. *Principles of developmental cardiovascular physiology and pathophysiology*, second edi ed. Elsevier Inc., 2012.

[163] Noori, S., Wlodaver, A., Gottipati, V., McCoy, M., Schultz, D., and Escobedo, M. Transitional changes in cardiac and cerebral hemodynamics in term neonates at birth. *J. Pediatr. 160*, 6 (2012), 943–948.

[164] Ntziachristos, V. Going deeper than microscopy: the optical imaging frontier in biology. *Nat. Methods 7*, 8 (aug 2010), 603–14.

[165] Ntziachristos, V., and Chance, B. Accuracy limits in the determination of absolute optical properties using time-resolved NIR spectroscopy. *Med. Phys. 28*, 6 (2001), 1115–1124.

[166] Obrist, W. D., Thompson, H. K., King, C. H., and Wang, H. S. Determination of regional cerebral blood flow by inhalation of 133-Xenon. *Circ. Res. 20*, 1 (1967), 124–135.

[167] Oda, M., Yamashita, Y., Nakano, T., Suzuki, A., Shimizu, K., Hirano, I., Shimomura, F., Ohmae, E., Suzuki, T., and Tsuchiya, Y. Near-infrared time-resolved spectroscopy system for tissue oxygenation monitor. *SPIE Conf. Opt. Tomogr. Spectrosc. Tissue III 3597*, January (2000), 204–210.

[168] Ohn, S. H., Park, C.-I., Yoo, W.-K., Ko, M.-H., Choi, K. P., Kim, G.-M., Lee, Y. T., and Kim, Y.-H. Time-dependent effect of transcranial direct current stimulation on the enhancement of working memory. *Neuroreport 19*, 1 (2008), 43–47.

[169] Pagliazzi, M., Giovannella, M., Weigel, U. M., Pifferi, A., Torricelli, A., and Durduran, T. Long-lasting, liquid phantom for diffuse optical and correlation spectroscopies. In *Biomed. Opt. 2016* (Washington, D.C., 2016), OSA, p. JTu3A.25.

[170] Patterson, M., Chance, B., and Wilson, B. Time resolved reflectance and transmittance for the non-invasive measurement of tissue optical properties. *Appl. Opt. 28*, 12 (1989), 2331–2336.

[171] Patterson, M. S., Andersson-Engels, S., Wilson, B. C., and Osei, E. K. Absorption spectroscopy in tissue-simulating materials: a theoretical and experimental study of photon paths. *Appl. Opt. 34*, 1 (1995), 22.

[172] Pichler, G., Binder, C., Avian, A., Beckenbach, E., Schmölzer, G. M., and Urlesberger, B. Reference ranges for regional cerebral tissue oxygen saturation and fractional oxygen extraction in neonates

during immediate transition after birth. *J. Pediatr. 163*, 6 (2013), 1558–1563.

[173] Pichler, G., Urlesberger, B., Baik, N., Schwaberger, B., Binder-Heschl, C., Avian, A., Pansy, J., Cheung, P. Y., and Schmölzer, G. M. Cerebral Oxygen Saturation to Guide Oxygen Delivery in Preterm Neonates for the Immediate Transition after Birth: A 2-Center Randomized Controlled Pilot Feasibility Trial. *J. Pediatr. 170* (2016), 73–78e4.

[174] Pifferi, A., Contini, D., Mora, A. D., Farina, A., Spinelli, L., and Torricelli, A. New frontiers in time-domain diffuse optics, a review. *J. Biomed. Opt. 21*, 9 (2016), 091310.

[175] Pifferi, A., Farina, A., Torricelli, A., Quarto, G., Cubeddu, R., and Taroni, P. Review: Time-domain broadband near infrared spectroscopy of the female breast: A focused review from basic principles to future perspectives. *J. Near Infrared Spectrosc. 20*, 1 (2012), 223–235.

[176] Pifferi, A., Torricelli, A., Bassi, A., Taroni, P., Cubeddu, R., Wabnitz, H., Grosenick, D., Möller, M., Macdonald, R., Swartling, J., Svensson, T., Andersson-Engels, S., van Veen, R. L. P., Sterenborg, H. J. C. M., Tualle, J.-M., Nghiem, H. L., Avrillier, S., Whelan, M., and Stamm, H. Performance assessment of photon migration instruments: the MEDPHOT protocol. *Appl. Opt. 44*, 11 (2005), 2104–2114.

[177] Pogue, B. W., and Patterson, M. S. Frequency-domain optical absorption spectroscopy of finite tissue volumes using diffusion theory. *Phys. Med. Biol. 39*, 7 (1994), 1157–1180.

[178] Prahl, S. Tabulated Molar Extinction Coefficient for Hemoglobin in Water. *https://omlc.org/spectra/hemoglobin/summary.html* (1998).

[179] Priori, A. Brain polarization in humans: a reappraisal of an old tool for prolonged non-invasive modulation of brain excitability. *Clin. Neurophysiol. 114*, 4 (2003), 589–595.

[180] Puig, O., Vestergaard, M. B., Lindberg, U., Hansen, A. E., Ulrich, A., Andersen, F. L., Johannesen, H. H., Rostrup, E., Law, I., Larsson, H. B., and Henriksen, O. M. Phase contrast mapping MRI measurements of global cerebral blood flow across different perfusion states - A direct comparison with 15O-H2O positron emission tomography using a hybrid PET/MR system. *J. Cereb. Blood Flow Metab.* (2018), 0271678X1879876.

[181] Raichle, M. E., Martin, W. R., Herscovitch, P., Mintun, M. A., and Markham, J. Brain blood flow measured with intravenous H2(15)O. II. Implementation and validation. *J. Nucl. Med. 24*, 9 (sep 1983), 790–8.

[182] Rath, G., Bithal, P., and Mahajan, C. Advances in neuromonitoring. *Anesth. Essays Res. 7*, 3 (2013), 312.

[183] Re, R., Contini, D., Zucchelli, L., Torricelli, A., and Spinelli, L. Effect of a thin superficial layer on the estimate of hemodynamic changes in a two-layer medium by time domain NIRS. *Biomed. Opt. Express 7*, 2 (2016), 264.

[184] Renna, M., Buttafava, M., Zappa, F., Tosi, A., Martinenghi, E., Zanoletti, M., Mora, A. D., Pifferi, A., Torricelli, A., and Contini, D. Compact dual-wavelength system for time-resolved diffuse optical spectroscopy. *PRIME 2017 - 13th Conf. PhD Res. Microelectron. Electron. Proc.* (2017), 293–296.

[185] Riera, J. J., and Sumiyoshi, A. Brain oscillations: ideal scenery to understand the neurovascular coupling. *Curr. Opin. Neurol. 23*, 4 (2010), 374–381.

[186] Ritter, P., and Villringer, A. Simultaneous EEG-fMRI. *Neurosci. Biobehav. Rev. 30*, 6 (2006), 823–838.

[187] Roche-Labarbe, N., Carp, S. a., Surova, A., Patel, M., Boas, D. a., Grant, P. E., and Franceschini, M. A. Noninvasive optical measures of CBV, StO(2), CBF index, and rCMRO(2) in human premature neonates' brains in the first six weeks of life. *Hum. Brain Mapp. 31*, 3 (2010), 341–52.

[188] Roche-Labarbe, N., Fenoglio, A., Radhakrishnan, H., Kocienski-Filip, M., Carp, S. a., Dubb, J., Boas, D. a., Grant, P. E., and Franceschini, M. A. Somatosensory evoked changes in cerebral oxygen consumption measured non-invasively in premature neonates. *Neuroimage 85* (2014), 279–86.

[189] Rosa, M. J., Daunizeau, J., and Friston, K. J. EEG-fMRI integration: a critical review of biophysical modeling and data analysis approaches. *J. Integr. Neurosci. 09*, 04 (2010), 453–476.

[190] Rounis, E., Lee, L., Siebner, H. R., Rowe, J. B., Friston, K. J., Rothwell, J. C., and Frackowiak, R. S. Frequency specific changes in regional cerebral blood flow and motor system connectivity following rTMS to the primary motor cortex. *Neuroimage 26*, 1 (2005), 164–176.

[191] Ruffini, G., Wendling, F., Merlet, I., Molaee-Ardekani, B., Mekonnen, A., Salvador, R., Soria-Frisch, A., Grau, C., Dunne, S., and Miranda, P. C. Transcranial current brain stimulation (tCS): models and technologies. *IEEE Trans. Neural Syst. Rehabil. Eng. 21*, 3 (2013), 333–45.

[192] Safaie, J., Grebe, R., Moghaddam, H. A., and Wallois, F. Toward a fully integrated wireless wearable EEG-NIRS bimodal acquisition system. *J. Neural Eng. 10*, 5 (2013), 056001.

[193] Saigal, S., and Doyle, L. W. An overview of mortality and sequelae of preterm birth from infancy to adulthood. *Lancet 371*, 9608 (jan 2008), 261–269.

[194] Sauseng, P., Griesmayr, B., Freunberger, R., and Klimesch, W. Control mechanisms in working memory: A possible function of EEG theta oscillations. *Neurosci. Biobehav. Rev. 34*, 7 (2010), 1015–1022.

[195] Scholkmann, F., Kleiser, S., Metz, A. J., Zimmermann, R., Mata Pavia, J., Wolf, U., and Wolf, M. A review on continuous wave functional near-infrared spectroscopy and imaging instrumentation and methodology. *Neuroimage 85* (2014), 6–27.

[196] Selb, J., Boas, D. a., Chan, S.-T., Evans, K. C., Buckley, E. M., and Carp, S. a. Sensitivity of near-infrared spectroscopy and diffuse correlation spectroscopy to brain hemodynamics: simulations and experimental findings during hypercapnia. *Neurophotonics 1*, 1 (2014), 015005.

[197] Siebner, H. R., Bergmann, T. O., Bestmann, S., Massimini, M., Johansen-Berg, H., Mochizuki, H., Bohning, D. E., Boorman, E. D., Groppa, S., Miniussi, C., Pascual-Leone, A., Huber, R., Taylor, P. C. J., Ilmoniemi, R. J., De Gennaro, L., Strafella, A. P., Kähkönen, S., Klöppel, S., Frisoni, G. B., George, M. S., Hallett, M., Brandt, S. A., Rushworth, M. F., Ziemann, U., Rothwell, J. C., Ward, N., Cohen, L. G., Baudewig, J., Paus, T., Ugawa, Y., and Rossini, P. M. Consensus paper: Combining transcranial stimulation with neuroimaging. *Brain Stimul. 2*, 2 (2009), 58–80.

[198] Siesjo, B. K. *Brain energy metabolism.* John Wiley & Sons, Ltd, New York, 1978.

[199] Sokoloff, L. The physiological and biochemical bases of functional brain imaging. *Cogn. Neurodyn. 2*, 1 (2008), 1–5.

[200] Sorensen, L. C., and Greisen, G. Precision of measurement of cerebral tissue oxygenation index using near-infrared spectroscopy in preterm neonates. *J. Biomed. Opt. 11*, 5 (2006), 054005.

[201] Sparing, R., Thimm, M., Hesse, M. D., Küst, J., Karbe, H., and Fink, G. R. Bidirectional alterations of interhemispheric parietal balance by non-invasive cortical stimulation. *Brain 132*, 11 (2009), 3011–3020.

[202] Spinelli, L., Martelli, F., Farina, A., Pifferi, A., Torricelli, A., Cubeddu, R., and Zaccanti, G. Accuracy of the nonlinear fitting procedure for time-resolved measurements on diffusive phantoms at NIR wavelengths. In *Proc. SPIE 7174, Opt. Tomogr. Spectrosc. Tissue VIII* (2009), vol. 7174, p. 717424.

[203] Spinelli, L., Zucchelli, L., Contini, D., Caffini, M., Mehler, J., Fló, A., Ferry, A. L., Filippin, L., Macagno, F., Cattarossi, L., and Torricelli, A. In vivo measure of neonate brain optical properties and hemodynamic parameters by time-domain near-infrared spectroscopy. *Neurophotonics 4*, 04 (2017), 1.

[204] Stone, D. B., and Tesche, C. D. Transcranial direct current stimulation modulates shifts in global/local attention. *Neuroreport 20* (2009), 1115–1119.

[205] Sureau, F. C., Reader, A. J., Comtat, C., Leroy, C., Ribeiro, M.-J., Buvat, I., and Trebossen, R. Impact of Image-Space Resolu-

tion Modeling for Studies with the High-Resolution Research Tomograph. *J. Nucl. Med. 49*, 6 (2008), 1000–1008.

[206] Sybulski, S., and Maughan, G. B. Cortisol levels in umbilical cord plasma in relation to labor and delivery. *Am. J. Obstet. Gynecol. 125*, 2 (1976), 236–238.

[207] Tamborini, D., Farzam, P., Zimmermann, B., Wu, K.-C., Boas, D. A., and Franceschini, M. A. Development and characterization of a multidistance and multiwavelength diffuse correlation spectroscopy system. *Neurophotonics 5*, 01 (2017), 1.

[208] Tasker, R. C., and Menon, D. K. Critical care and the brain. *JAMA - J. Am. Med. Assoc. 315*, 8 (2016), 749–750.

[209] Team R Core. R: A Language and Environment for Statistical Computing, 2016.

[210] Toronov, V., D'Amico, E., Hueber, D., Gratton, E., Barbieri, B., and Webb, A. Optimization of the signal-to-noise ratio of frequency-domain instrumentation for near-infrared spectro-imaging of the human brain. *Opt. Express 11*, 21 (oct 2003), 2717.

[211] Torricelli, A., Contini, D., Pifferi, A., Caffini, M., Re, R., Zucchelli, L., and Spinelli, L. Time domain functional NIRS imaging for human brain mapping. *Neuroimage 85* (2014), 28–50.

[212] Turi, Z., Ambrus, G. G., Ho, K. A., Sengupta, T., Paulus, W., and Antal, A. When size matters: Large electrodes induce greater stimulation-related cutaneous discomfort than smaller electrodes at equivalent current density. *Brain Stimul. 7*, 3 (2014), 460–467.

[213] Urlesberger, B., Grossauer, K., Pocivalnik, M., Avian, A., Müller, W., and Pichler, G. Regional oxygen saturation of the

brain and peripheral tissue during birth transition of term infants. *J. Pediatr. 157*, 5 (2010), 740–744.

[214] Urlesberger, B., Kratky, E., Rehak, T., Pocivalnik, M., Avian, A., Czihak, J., Müller, W., and Pichler, G. Regional oxygen saturation of the brain during birth transition of term infants: Comparison between elective cesarean and vaginal deliveries. *J. Pediatr. 159*, 3 (2011), 404–408.

[215] Verdecchia, K., Diop, M., Lee, T.-Y., and St Lawrence, K. Quantifying the cerebral metabolic rate of oxygen by combining diffuse correlation spectroscopy and time-resolved near-infrared spectroscopy. *J. Biomed. Opt. 18*, 2 (2013), 27007.

[216] Vestergaard, M. B., Lindberg, U., Aachmann-Andersen, N. J., Lisbjerg, K., Christensen, S. J., Law, I., Rasmussen, P., Olsen, N. V., and Larsson, H. B. Acute hypoxia increases the cerebral metabolic rate - a magnetic resonance imaging study. *J. Cereb. Blood Flow Metab. 36*, 6 (jun 2016), 1046–1058.

[217] Vestergaard, M. B., Lindberg, U., Aachmann-Andersen, N. J., Lisbjerg, K., Christensen, S. J., Rasmussen, P., Olsen, N. V., Law, I., Larsson, H. B. W., and Henriksen, O. M. Comparison of global cerebral blood flow measured by phase-contrast mapping MRI with 15O-H2O positron emission tomography. *J. Magn. Reson. Imaging 45*, 3 (2017), 692–699.

[218] Vogenberg, F. R., Isaacson Barash, C., and Pursel, M. Personalized medicine: part 1: evolution and development into theranostics. *P T 35*, 10 (2010), 560–576.

[219] Vorstrup, S., Henriksen, L., and Paulson, O. B. Effect of acetazolamide on cerebral blood flow and cerebral metabolic rate for oxygen. *J. Clin. Invest. 74*, 5 (1984), 1634–9.

[220] Wang, J., Licht, D. J., Jahng, G.-H., Liu, C.-S., Rubin, J. T., Haselgrove, J., Zimmerman, R. a., and Detre, J. a. Pediatric perfusion imaging using pulsed arterial spin labeling. *J. Magn. Reson. Imaging 18*, 4 (2003), 404–13.

[221] Wang, L. V., and Wu, H.-i. *Biomedical Optics: Principles and Imaging.* John Wiley & Sons, Ltd, 2012.

[222] Warwick, J. M. Imaging of brain function using SPECT. *Metab. Brain Dis. 19*, 1-2 (2004), 113–123.

[223] Wirth, M., Rahman, R. A., Kuenecke, J., Koenig, T., Horn, H., Sommer, W., and Dierks, T. Effects of transcranial direct current stimulation (tDCS) on behaviour and electrophysiology of language production. *Neuropsychologia 49*, 14 (2011), 3989–3998.

[224] Wolf, M., Ferrari, M., and Quaresima, V. Progress of near-infrared spectroscopy and topography for brain and muscle clinical applications. *J. Biomed. Opt. 12*, 6 (2007), 062104.

[225] Wong, F. Y., Alexiou, T., Samarasinghe, T., Brodecky, V., and Walker, A. M. Cerebral arterial and venous contributions to tissue oxygenation index measured using spatially resolved spectroscopy in newborn lambs. *Anesthesiology 113*, 6 (2010), 1385–1391.

[226] Yu, G., Durduran, T., Lech, G., Zhou, C., Chance, B., Mohler, E. R., and Yodh, A. G. Time-dependent blood flow and oxygenation in human skeletal muscles measured with noninvasive near-infrared diffuse optical spectroscopies. *J. Biomed. Opt. 10*, 2 (2005), 024027.

[227] Zaehle, T., Sandmann, P., Thorne, J. D., Jäncke, L., and Herrmann, C. S. Transcranial direct current stimulation of the prefrontal cortex modulates working memory performance: combined behavioural and electrophysiological evidence. *BMC Neurosci. 12*, 1 (2011), 2.

[228] Zhao, J., Ding, H. S., Hou, X. L., Zhou, C. L., and Chance, B. In vivo determination of the optical properties of infant brain using frequency-domain near-infrared spectroscopy. *J. Biomed. Opt. 10*, 2 (2005), 024028.

[229] Zheng, X., Alsop, D. C., and Schlaug, G. Effects of transcranial direct current stimulation (tDCS) on human regional cerebral blood flow. *Neuroimage 58*, 1 (2011), 26–33.

[230] Zhou, C. *In-vivo optical imaging and spectroscopy of cerebral Hemodynamics*. PhD thesis, University of Pennsylvania, 2007.

[231] Zhou, C., Yu, G., Furuya, D., Greenberg, J. H., Yodh, A. G., and Durduran, T. Diffuse optical correlation tomography of cerebral blood flow during cortical spreading depression in rat brain. *Opt. Express 14*, 3 (2006), 1125.

[232] Zucchelli, L., Contini, D., Re, R., Torricelli, A., and Spinelli, L. Method for the discrimination of superficial and deep absorption variations by time domain fNIRS. *Biomed. Opt. Express 4*, 12 (2013), 2893–910.